Palacký University Olomouc

Faculty of Science

Joint Laboratory of Optics

Generation of Non-Classical Light in Photonic Structures

by

Radek Machulka

for

Ph.D. Degree

in

Olomouc

Czech Republic

2015

Univerzita Palackého v Olomouci
Přírodovědecká fakulta
Společná laboratoř optiky

Generace neklasických stavů světla ve fotonických strukturách

Radek Machulka

Disertační práce

Školitel:
Doc. Mgr. Jan Soubusta, Ph.D.

Olomouc
2015

Bibliographic Details

Title	Generation of Non-Classical Light in Photonic Structures
Nadpis	Generace neklasických stavů světla ve fotonických strukturách
Type	Ph.D. Degree Thesis
Author	Radek Machulka
Supervisor	Doc. Mgr. Jan Soubusta, Ph.D.
University	Palacký University Olomouc
Study program	Physics
	Optics and Optoelectronics
Department	Joint Laboratory of Optics
Language	English
Year	2015
Pages	134

Statement of Originality

I hereby declare that this thesis is my own work and that, to the best of my knowledge and belief, it contains no material previously published or written by another person nor material which to a substantial extent has been accepted for the award of any other degree or diploma of the university or other institute of higher learning, except where due acknowledgement has been made in the text.

The author grants permission to Palacký University in Olomouc to store and display this thesis and its electronic version in the university library and on the official website.

In Olomouc	Radek Machulka

Acknowledgement

Here, I would like to acknowledge all my colleagues and friends, who have been supporting me during my studies. I have to express my deepest gratitude to my supervisor Jan Soubusta for his guidance since the very beginning of my scientific career. I would also like to expand my special thanks to Ondřej Haderka and Jan Peřina for their support and encouragement, and to the rest of our group, too, namely to Václav Michálek, Antonín Černoch, Karel Lemr, and Jiří Svozilík for their countless friendly advices over the years.

Abstract

The second-order nonlinear processes are nowadays relatively common type of interactions, not only in optical laboratories. For instance second-harmonic and sum- or difference-frequency generation are widely used wave mixing techniques, especially useful for producing laser beams at different frequencies. On the other hand, process of spontaneous parametric down-conversion has become fundamental tool in almost any quantum-optical experiment as a source of entangled photon pairs. In this thesis, photonic structures based mainly on waveguides will be presented as an alternative source of second-order nonlinear processes with respect to ordinary used bulk crystals.

First, periodically-poled KTP waveguide will be characterized in process of second-harmonic generation, where quasi-phase-matching is utilized. It will be shown experimentally, that this structure can support whole set of processes differing in spectral and spatial profiles as well as in polarizations of interacting fields. The influence of fabrication imperfections on generated fields will be here also considered.

Then, a sophisticated source of entangled photon pairs based on Kwiat's design will be used to generate full set of Bell's states as a set of maximally entangled two-photon states. These states will be subjected to complete quantum tomography and non-locality test in order to experimentally prove their quantum nature.

Next, so-called Bragg reflection waveguides will be presented as a promising source of entangled photon pairs especially suitable for monolithic integration into compact optical devices. Modal phase-matching technique will be demonstrated as a method to compensate for dispersion effects. Non-classicality of generated fields will be verified by violation of Bell's like inequalities. This experimental study will be performed at standard telecommunication wavelength 1550 nm to demonstrate practical potential of such devices.

Also standard bulk-oriented source of photon pairs will be investigated. Such sources are interesting due to their simplicity and they are therefore ideal for comparative studies. Here, a link between different intensity regimes will be demonstrated, which can be advantageous, for instance, for quantum communications through lossy channels.

Finally, the luminescence-induced noise of nonlinear BBO crystals will be characterized both in time and spectral domain. Based on these results, an optimal strategies for filtering the luminescence will be discussed. The influence of such noise on simple heralded single photon source will be quantified at the end.

Abstract in Czech

Nelineární jevy druhého řádu jsou dnes již relativně běžně užívané procesy nejen v optických laboratořích. Například generace druhé harmonické a generace součtové či rozdílové frekvence jsou široce používané techniky vlnového směšování vhodné pro generaci optických svazků na různých frekvencích. Naproti tomu proces parametrické fluorescence je základním stavebním kamenem většiny kvantově-optických experimentů jako zdroj entanglovaných fotonových párů. V této práci budou studovány fotonické struktury založené zejména na vlnovodech jako zdroje nelineárních jevů druhého řádu alternativní k tradičně používaným objemovým krystalům.

Periodicky pólovaný vlnovod bude charakterizován v procesu generace druhé harmonické frekvence, kde je využita tzv. náhradní podmínka fázového sladění. Bude experimentálně ukázáno, že tyto struktury mohou simultánně generovat celou řadu procesů lišícími se jak spektrálními a prostorovými vlastnostmi, tak i polarizacemi interagujících polí. Rovněž bude diskutován vliv nedokonalostí výrobního procesu na vlastnosti generovaných polí.

Dále bude prezentován Kwiatův zdroj kvantově korelovaných (entanglovaných) fotonových párů. Tento zdroj bude použit pro generaci polarizačních Bellových stavů, které jsou maximálně entanglované dvoufotonové stavy. Tyto stavy pak budou předmětem dalšího studia. Pomocí metody kvantové tomografie a zejména porušením Bellových nerovností bude experimentálně ověřeno, že se jedná skutečně o neklasické stavy světla.

Neklasická světelná pole budou rovněž generována pomocí tzv. Braggových vlnovodů, kde se využívá módového fázového sladění. Tyto struktury jsou výhodné zejména vzhledem k jejich potenciální možnosti integrace do složitějších optických obvodů. Tyto experimenty byly navíc provedeny na standardní telekomunikační vlnové délce 1550 nm, což dále dokazuje jejich praktický potenciál. Neklasičnost generovaných polí bude i zde experimentálně prokázána porušením Bellových nerovností.

Studium polí generovaných klasickými objemovými krystaly bude rovněž obsahem této práce. Díky jejich jednoduchosti jsou ideálními kandidáty pro srovnání. Zde bude sledována souvislost mezi různými intenzitními režimy generace sestupné parametrické konverze pomocí studia prostorových korelací generovaných polí. Tato znalost může být užitečná např. pro návrh kvantově-informačních protokolů pro komunikaci ztrátovými linkami.

Poslední kapitola bude věnována studiu neparametrických procesů, které představují šum doprovázející parametrické procesy generované v objemových BBO krystalech. U takto generovaných polí budou studovány spektrální a časové vlastnosti na jejichž základě bude navržena optimální strategie pro filtraci tohoto šumu. Na závěr bude kvantifikován vliv takového šumu na kvalitu jednofotonového zdroje.

Contents

Introduction

Nonlinear process of spontaneous parametric down-conversion is in optical domain the most common source of correlated photon pairs, as an indispensable ingredient in many quantum-optics based applications. Until recently, the most setups for this process were based almost exclusively on nonlinear bulk crystals pumped by intense laser beams.

In recent years, however, more sophisticated photonic devices have become widely used, especially for their higher conversion efficiencies and ability to modify properties of generated fields. These sources are usually based on waveguides, which in addition allow for their integration, and thus for construction of compact optical circuits.

In field of quantum optics, where non-classical properties of photon pairs are highly utilized, the most applications are based on single photon pairs. However, at single photon level optical states suffer from losses. Even though a long-distance communications with single photons have already been performed, the possibility to extend these experiments to mesoscopic regime, where the states are more robust against losses, is of a great importance.

The Goals of the Thesis

The main goal of this thesis is to study nonlinear photonic devices from the perspective of generation of non-classical states of light through the process of parametric down-conversion, also considering practical aspects. Periodically-poled waveguides as well as relatively new Bragg reflection waveguides are studied as a promising bright sources for integrated platforms. Possible limitations by imperfections of fabrication process are considered as well. More common bulk crystals are also used to generate more complex entangled states and fields, whose correlations properties are studied not only at single-photon level, but also in a mesoscopic domain.

Annotation

Chapter 1 contains basic theoretical introduction into nonlinear optics and photonic devices. This treatment is focused mainly on the second-order nonlinear processes, especially on second-harmonic generation and spontaneous parametric down-conversion. Special attention is given to the phase-matching as a fundamental criterion in experiments. Finally, generation in bulk crystals as well as in guided structures is considered.

Chapter 2 describes experimental characterization of periodically-poled KTP waveguide through the process of second-harmonic generation. The theory of second-harmonic gener-

ation is further developed in this chapter. Fabrication imperfections are also included into numerical model. The experimental results are compared to the theory in the second part of this chapter.

In chapter 3, the phenomenon of quantum entanglement is discussed. First, the theoretical description of this system is developed. Basic experimental tools for determination and characterization of non-classical quantum states are also presented. Next, a set of entangled states is generated experimentally using parametric down-conversion and their non-classicality is afterwords experimentally verified.

As it is shown in chapter 4, Bragg reflection based waveguide can be utilized instead of bulk crystals in order to generate entangled photon states. At the beginning, the modal structure of this waveguide is determined and the phase-matching strategy based on modal phase-matching is calculated. Finally, the entangled two-photon states are generated and their non-classicality is experimentally proven.

Chapter 5 shows another potential benefits of parametric down-conversion. It mainly focuses on spatial correlations in generated fields. It experimentally demonstrates the link between different intensity regimes, where the generation can be either spontaneous or stimulated.

The final chapter 6 demonstrates the influence of luminescence induced noise on sources based on parametric down-conversion. The luminescence is characterized in spectral and time domain. Based on these results, an optimal strategies for minimizing its influence are suggested. The influence of luminescence on heralded single-photon source is also quantitatively estimated.

Finally, this thesis is concluded in the very last chapter, where the most important results are summarized. This chapter also gives a brief outlook and potential extension of presented research.

The theses ends with list of author's publications and relevant references.

1 Nonlinear Optics

Nonlinear optics is a part of optics studying propagation of strong optical fields through a media in which they induce the nonlinear response. It is therefore typical to study the dependence of dielectric polarization **P** on the electric field **E**.

Although this phenomenon was known long before, the massive interest in nonlinear optics raised shortly after invention of laser by Maiman in 1960. The breakthrough in the field is usually considered to be the very first observation of second-harmonic generation in 1961 by Franken *at al.*. The main reason was the fact, that the nonlinear phenomenons require high optical intensities in order to be generated effectively. The nonlinearity is however not an attribute of the radiation itself, but of the medium the radiation is propagating through. The propagating optical field modifies the property of the medium, which can afterwards modify back the propagating field. Since the properties of dielectric medium, in which the optical field is propagating, is described with relation between vector of dielectric polarization **P** and the electric vector **E**, the nonlinear wave equation has to be derived first in order for any nonlinear interaction to be characterized.

1.1 Nonlinear Wave Equation

The nonlinear wave equation is an equation describing propagation of an optical field through nonlinear optical medium. Similarly as for the linear wave equation, the full set of Maxwell's

equations in differential form has to be used

$$\nabla \times \mathbf{E} + \frac{\partial \mathbf{B}}{\partial t} = 0, \tag{1.1a}$$

$$\nabla \times \mathbf{H} - \frac{\partial \mathbf{D}}{\partial t} = \mathbf{j}, \tag{1.1b}$$

$$\nabla \cdot \mathbf{D} = \rho, \tag{1.1c}$$

$$\nabla \cdot \mathbf{B} = 0. \tag{1.1d}$$

The names of the field vectors from these equations and their units are as follows

$$\begin{aligned}
[\mathbf{E}] &= \mathrm{V\,m^{-1}} && \ldots \text{ electric field,}\\
[\mathbf{H}] &= \mathrm{A\,m^{-1}} && \ldots \text{ magnetic intensity,}\\
[\mathbf{D}] &= \mathrm{C\,m^{-2}} && \ldots \text{ electric displacement,}\\
[\mathbf{B}] &= \mathrm{Wb\,m^{-2}} && \ldots \text{ magnetic induction,}\\
[\mathbf{j}] &= \mathrm{A\,m^{-2}} && \ldots \text{ electric current density,}\\
[\rho] &= \mathrm{C\,m^{-1}} && \ldots \text{ electric charge density.}
\end{aligned}$$

Maxwell's equations represent basic laws of electricity and magnetism and fully describe the propagation of electromagnetic field in any medium. The first equation (1.1a) represents Faraday's law of induction describing the creation of an induced electric field due to the time-varying magnetic flux. The second equation (1.1b) is generalized Ampere's law describing creation of an induced magnetic field due to the electric charge flow. The third equation (1.1c) represents Coulomb's law describing creation of electric field by the electric charge distribution. And finally, the fourth equation (1.1d) characterizes absence of magnetic charge, or better, magnetic monopole.

The quantities ρ and $\mathbf{j}$ in Maxwell's equations (1.1b) and (1.1c) are the source quantities, and can be therefore regarded as sources of electromagnetic fields. The Maxwell's equations will be here solved in regions far from the sources, where no free charges or free currents are present, and therefore

$$\rho = 0, \tag{1.2a}$$

$$\mathbf{j} = 0. \tag{1.2b}$$

Maxwell's equations as presented create set of coupled differential equations, which in order to be solved must be supplemented with so-called material relations, describing response of the material to the electromagnetic field. Since the optical frequencies are too fast to affect the magnetic properties, the matter is considered to be non-magnetic in optical part of the spectrum, and the material relations therefore gain following form

$$\mathbf{B} = \mu_0 \mathbf{H}, \tag{1.3a}$$

$$\mathbf{D} = \varepsilon_0 \mathbf{E} + \mathbf{P}, \tag{1.3b}$$

where ε_0 and μ_0 are the permittivity and permeability of the vacuum, respectively. Vector $\mathbf{P}$ ($[\mathbf{P}] = \mathrm{C/m^2}$) denotes already mentioned vector of dielectric polarization. Let it be

noted, that in order to found particular unique solution of Maxwell's equations, also the initial and boundary conditions have to be specified.

With such specified material relations, the nonlinear wave equation can be easily derived from specified Maxwell's equations (1.1a)–(1.1d). First, the curl operator is to be applied on the first Maxwell's equation (1.1a), while interchanging order of time and space derivations

$$\nabla \times \nabla \times \mathbf{E} + \frac{\partial}{\partial t}(\nabla \times \mathbf{B}) = 0. \tag{1.4}$$

Next, the right-hand term $\nabla \times \mathbf{B}$ is replaced using the second Maxwell's equation (1.1b), where material equation (1.3a) was used in order to substitute $\mathbf{H}$ for $\mathbf{B}$

$$\nabla \times \nabla \times \mathbf{E} + \mu_0 \frac{\partial^2 \mathbf{D}}{\partial t^2} = 0. \tag{1.5}$$

Finally, replacing electric displacement vector $\mathbf{D}$ from equation (1.3b) the nonlinear wave equation is obtained

$$\nabla \times \nabla \times \mathbf{E} + \varepsilon_0 \mu_0 \frac{\partial^2 \mathbf{E}}{\partial t^2} = -\mu_0 \frac{\partial^2 \mathbf{P}}{\partial t^2}. \tag{1.6}$$

It is also convenient to express vector of dielectric polarization $\mathbf{P}$ as a sum of its linear and nonlinear parts

$$\mathbf{P} = \mathbf{P}^{(1)} + \mathbf{P}^{(\mathrm{NL})}, \tag{1.7}$$

where

$$\mathbf{P}^{(1)} = \varepsilon_0 \chi^{(1)} \mathbf{E}. \tag{1.8}$$

Quantity $\chi^{(1)}$ denotes the linear susceptibility of the material, where index (1) represents linear dependence of dielectric polarization on electric field. Now, with the new form of vector of dielectric polarization $\mathbf{P}$ from equation (1.7) together with equation (1.8) the nonlinear wave equation (1.6) can be rewritten as follows

$$\nabla \times \nabla \times \mathbf{E} + \varepsilon_0 \mu_0 \left(1 + \chi^{(1)}\right) \frac{\partial^2 \mathbf{E}}{\partial t^2} = -\mu_0 \frac{\partial^2 \mathbf{P}^{(\mathrm{NL})}}{\partial t^2}. \tag{1.9}$$

Next, vector identity for double curl of electric field vector $\mathbf{E}$

$$\nabla \times \nabla \times \mathbf{E} = \nabla(\nabla \cdot \mathbf{E}) - \nabla^2 \mathbf{E}, \tag{1.10}$$

can be used in order to obtain even more typical form of wave equation. In the case of nonlinear media, the third Maxwell's equation (1.1c) does not guarantee vanishing of the first term on the right-hand side of this identity, because of the nonlinear term $\mathbf{P}^{(\mathrm{NL})}$ in equation (1.7). Despite to that, it can be shown[1], that for approximation of slowly varying amplitude, this term is negligible in comparison to other terms, and can be therefore suppressed. The wave equation thus gets the following form

$$\nabla^2 \mathbf{E} - \frac{n^2}{c^2} \frac{\partial^2 \mathbf{E}}{\partial t^2} = \mu_0 \frac{\partial^2 \mathbf{P}^{(\mathrm{NL})}}{\partial t^2}, \tag{1.11}$$

where two new parameters were introduced: $c = 1/\sqrt{\varepsilon_0 \mu_0}$ is speed of light in vacuum and $n = \sqrt{\varepsilon_r} = \sqrt{1 + \chi^{(1)}}$ is the refractive index of non-magnetic media. Using definition of Laplace operator $\Delta \mathbf{E} = \nabla^2 \mathbf{E} = (\nabla \cdot \nabla)\mathbf{E}$, expected final form of the nonlinear wave equation can be obtained

$$\Delta \mathbf{E} - \frac{n^2}{c^2} \frac{\partial^2 \mathbf{E}}{\partial t^2} = \frac{1}{\varepsilon_0 c^2} \frac{\partial^2 \mathbf{P}^{(\mathrm{NL})}}{\partial t^2}. \tag{1.12}$$

This equations contains only electric material constants, the magnetic ones are hidden only in the speed of light c.

1.2 Nonlinear Processes

The nonlinear wave equation (1.12) derived in previous section represents inhomogeneous differential equation, where the inhomogeneous term on the right-hand side acts as a source quantity. Physically, the time-varying vector of dielectric polarization $\mathbf{P}^{(\mathrm{NL})}$, induced by external optical field, acts as a source of new electromagnetic radiation even at different frequency then has the original field. This can be understood in such a way, that the second time derivative represents acceleration of dielectric polarization, which is in general density of dipole momentum, and represents therefore the charge displacement within the medium, which if accelerated generates the electromagnetic field.

Mathematically it is advantageous to solve wave equation (1.12) without right-hand side first. Afterwords, this solution is used for solving inhomogeneous equation by means of Green's function method. The physical meaning of these solutions are electromagnetic waves propagating with phase velocity $v = c/n$

$$\mathbf{E}(\mathbf{r}, t) = \mathcal{E} e^{i(\mathbf{k}\cdot\mathbf{r} - \omega t)} + c.c., \tag{1.13}$$

where $\mathcal{E}$ denotes its constant amplitude, $|\mathbf{k}| = (n\omega)/c$ its wavenumber and ω its angular frequency. Expression $c.c.$ stands for the complex conjugate part and will be suppressed unless specified otherwise.

As for the complete form of nonlinear wave equation with right-hand side (1.12), the solution is expected in the same form as the equation (1.13). The presence of the right-hand side, as will be shown later, will result in energy coupling between different frequencies called wave mixing. This consequence is of a grate importance. It means, that unlike in linear optics, where one of the most essential feature of electromagnetic radiation is, that it does not change its frequency as it is propagating through the matter, here the energy can be exchanged between different frequency modes through adequate nonlinear interaction.

In order to better identify individual nonlinear processes, the vector of nonlinear dielectric polarization $\mathbf{P}^{(\mathrm{NL})}$ from equation (1.7) can be expressed in infinite Taylor's series, so the overall response of the media on propagating optical field $\mathbf{P}(t) = \varepsilon_0 \chi \mathbf{E}(t)$ gets expanded in form of following power series

$$P_i(t) = \overbrace{\varepsilon_0 \chi^{(1)}_{ij} E_j(t)}^{\text{Linear}} + \overbrace{\underbrace{\varepsilon_0 \chi^{(2)}_{ijk} E_j(t) E_k(t)}_{2^{\text{nd}}\text{ order}} + \underbrace{\varepsilon_0 \chi^{(3)}_{ijkl} E_j(t) E_k(t) E_l(t)}_{3^{\text{th}}\text{ order}} + \cdots}^{\text{Nonlinear}}, \tag{1.14}$$

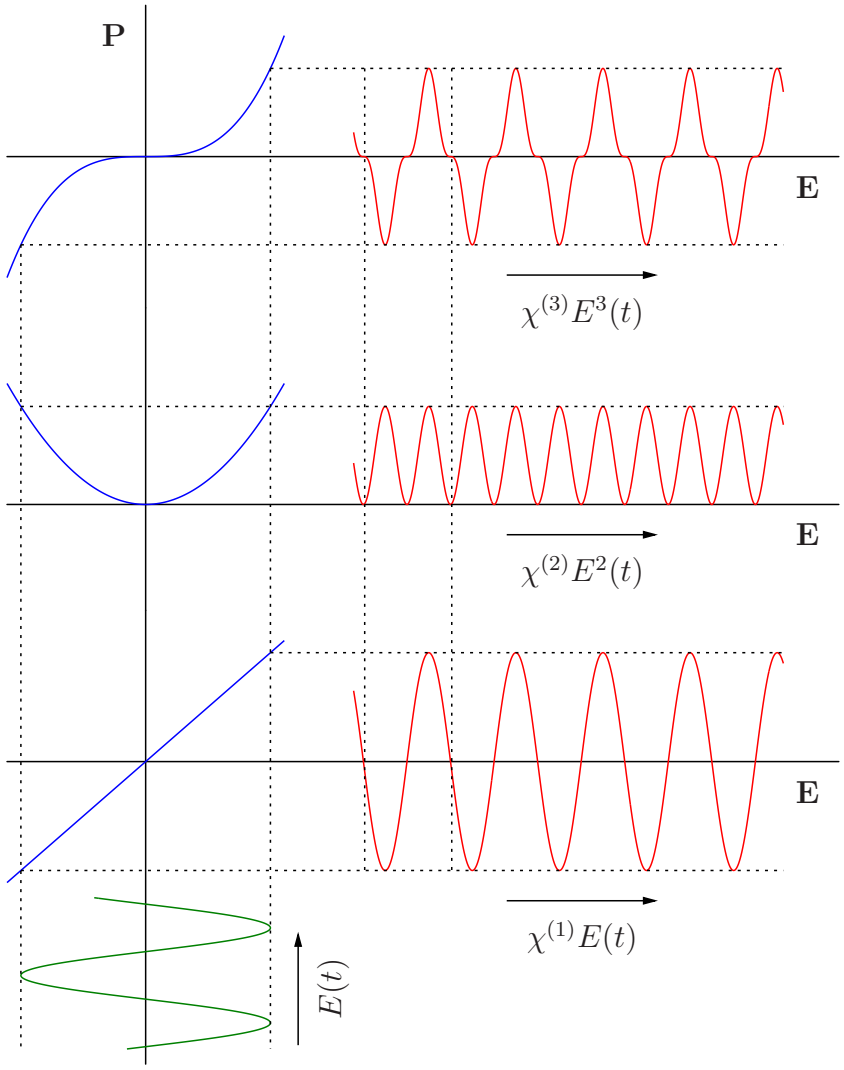

Figure 1.1: Schematic representation of material response characterized by the vector of dielectric polarization $\mathbf{P}(t)$ on incident optical field $\mathbf{E}(t)$ of sinusoidal running with angular frequency ω. Three different orders are illustrated separately: linear response $\chi^{(1)}E(t)$, nonlinear response of second-order $\chi^{(2)}E^2(t)$, and third-order nonlinear response $\chi^{(3)}E^3(t)$.

where Einstein's summation rule (summations over repeated indices) was used, and where quantity $\chi^{(i)}\big|_{i=2}^{\infty}$ denotes i-th order of nonlinear susceptibility tensor of $(i+1)$-th rank. Corresponding term $\mathbf{P}^{(i)} = \varepsilon_0\chi^{(i)} \cdot \mathbf{E}^i(t)\big|_{i=2}^{\infty}$ consequently represents i-th order nonlinear process. The graphical representation of nonlinear response of dielectric polarization vector $\mathbf{P}(t)$ on incident field $\mathbf{E}(t)$ as presented in equation (1.14) is for the first three orders depicted in the figure 1.1.

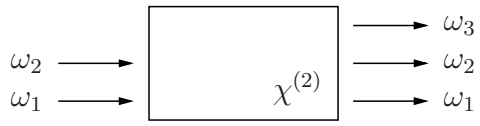

Figure 1.2: Schematic representation of second-order nonlinear process as a three-wave mixing. Fields ω_1 and ω_2 represents the input fields, while ω_3 represents field created via nonlinear interaction. The value of frequency of created field depends on particular type of interaction.

Based on properties of general Taylor series, even though the series from equation (1.14) does not necessary converge, the sequence $\left\{\chi^{(i)}\right\}_{i=1}^{\infty}$ is decreasing (i.e. $\chi^{(i)} < \chi^{(i+1)}$). As a consequence, nonlinear processes of i-th order are stronger (requires less pump powers in order to be observed) than processes of $(i+1)$-th order. It can be shown[2], that second-order nonlinear processes (characterized by nonlinear susceptibility $\chi^{(2)}$) will be comparable with the linear response (characterized by linear susceptibility $\chi^{(1)}$) if the external optical field E is of the order of an atomic field strength E_{at}. Based on this assumption, sizes of nonlinear susceptibility of any order can be estimated as $\chi^{(i)} \simeq \chi^{(1)}/E_{\text{at}}^{i-1}$, where $E_{\text{at}} \approx 10^{11}\,\text{Vm}^{-1}$. This gives a general idea, how much power is required for nonlinear effect to be observed. Another important property is, that i-th order nonlinear process utilized interaction of $i+1$ electromagnetic waves, so for instance nonlinear process of third-order leads to four-wave mixing (i.e. interaction of four in general different optical fields).

In order to identify practical consequences of different orders of nonlinear polarization, each of them should be investigated separately in order to keep the analysis simple. Here in this thesis however, only nonlinear processes of second-order will be discussed.

1.3 Second-Order Nonlinear Processes

In this section, the most elementary nonlinear effects, processes of second-order will be considered. The incident optical field $E(t)$ consists in this case of two different components with two generally different angular frequencies ω_1 and ω_2

$$E(t) = E_1 e^{-i\omega_1 t} + E_2 e^{-i\omega_2 t}, \tag{1.15}$$

as schematically depicted in the figure 1.2. Taking into account only second-order nonlinear interaction $P^{(2)}(t) = \varepsilon_0 \chi^{(2)} E^2(t)$, following expression for second-order nonlinear polarization is obtained

$$\begin{aligned} P^{(2)}(t) = {} & 2\varepsilon_0 \chi^{(2)} \left(E_1 E_1^* + E_2 E_2^*\right) + \\ & + \varepsilon_0 \chi^{(2)} \left(E_1^2 e^{-i2\omega_1 t} + E_2^2 e^{-i2\omega_2 t}\right) + \\ & + 2\varepsilon_0 \chi^{(2)} \left(E_1 E_2 e^{-i(\omega_1+\omega_2)t} + E_1 E_2^* e^{-i(\omega_1-\omega_2)t}\right). \end{aligned} \tag{1.16}$$

In this case the complex conjugate parts were also considered. In derived expression (1.16), following complex amplitudes can be identified

$$\begin{aligned}
P^{(2)}(0) &= 2\varepsilon_0\chi^{(2)}\left(|E_1|^2 + |E_2|^2\right) && \ldots \text{ optical rectification,}\\
P^{(2)}(2\omega_1) &= \varepsilon_0\chi^{(2)}E_1^2 && \ldots \text{ second-harmonic generation,}\\
P^{(2)}(2\omega_2) &= \varepsilon_0\chi^{(2)}E_2^2 && \ldots \text{ second-harmonic generation,}\\
P^{(2)}(\omega_1+\omega_2) &= 2\varepsilon_0\chi^{(2)}E_1E_2 && \ldots \text{ sum-frequency generation,}\\
P^{(2)}(\omega_1-\omega_2) &= 2\varepsilon_0\chi^{(2)}E_1E_2^* && \ldots \text{ difference-frequency generation.}
\end{aligned}$$

The reason to call the processes second-, sum-, or difference-frequency generation is obvious. The contribution, for instance, with complex amplitude $P^{(2)}(2\omega_1)$ will according to nonlinear wave equation (1.12) lead to generation of electromagnetic field with angular frequency $2\omega_1$, which is second-harmonic frequency to the fundamental frequency ω_1. On the other hand, component with corresponding complex amplitude $P^{(2)}(0)$ can not lead to any electromagnetic radiation, since its second time derivative will vanish. It can however lead to process called optical rectification, when electrostatic field is generated by the optical field. Third- and higher-orders of nonlinear interaction can be analysed in a similar way.

Before more detailed analysis will be continued, one more important matter has to be addressed first. All until now mentioned nonlinear processes are often called parametric. Parametric here means, that the medium does not contribute to the interaction directly, but acts only as a parameter. This means, that there is no energy transition between fields and a matter, because the atoms are not absorbing the fundamental radiation. The excitation can be expressed only using virtual levels with ultra-short lifetimes. The important consequence is, that electromagnetic energy in all interacting modes has to be conserved.

In order to describe second-order nonlinear processes in detail, the full vectorial approach has to be used. Second-order of nonlinear polarization from equation (1.14) can be in its full form expressed as follows

$$P_i^{(2)}(\omega_n+\omega_m) = \varepsilon_0\sum_{jk}\sum_{nm}\chi_{ijk}^{(2)}(\omega_n+\omega_m,\omega_n,\omega_m)E_j(\omega_n)E_k(\omega_m), \tag{1.17}$$

where indices ijk denote the space coordinates $\{x, y, z\}$ and indices nm represent two different input fields. As was already shown in equation (1.16), even while focusing only on limited class of second-order nonlinear processes, there are many representatives. Later in this chapter only two of them (second-harmonic generation and spontaneous parametric down-conversion) will be discussed in more details.

1.3.1 Conservation Laws

Nonlinear processes can be seen not only from the perspective of wave mixing, but also from the perspective of photon interaction. Sum-frequency generation, for instance, can be therefore understood as a process, where two photons with frequencies ω_1, ω_2 and wave vectors $\mathbf{k}_1$, $\mathbf{k}_2$, respectively are annihilated, while new photon with angular frequency ω_3

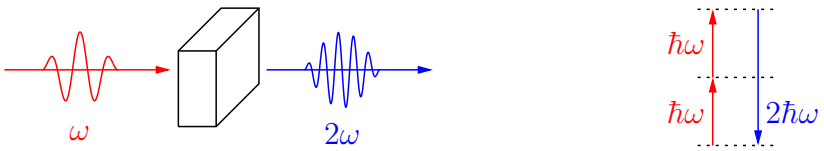

(a) (b)

Figure 1.3: Schematic representation of pulse pumped second-harmonic generation: (a) collinear geometry of the process, (b) virtual energy-level transition.

and wave vector $\mathbf{k}_3$ is created. For any interaction of this type, a fundamental conservation laws has to be fulfilled. In this case energy and momentum conservation laws take place

$$\hbar\omega_3 = \hbar\omega_1 + \hbar\omega_2, \tag{1.18a}$$
$$\hbar\mathbf{k}_3 = \hbar\mathbf{k}_1 + \hbar\mathbf{k}_2. \tag{1.18b}$$

Presented laws lead to already known frequency condition $\omega_3 = \omega_1 + \omega_2$, which determines frequency of produced field and a so-called phase-matching condition $\mathbf{k}_3 = \mathbf{k}_1 + \mathbf{k}_2$, which as will be shown later determines the efficiency of the process.

1.3.2 Second-Harmonic Generation

Nonlinear process of second-harmonic generation (SHG) is probably the most common nonlinear interaction. As a result of its simplicity from both theoretical and experimental point of view, together with its practical importance, it has been one of the most studied and used nonlinear optical phenomenon since the invention of laser. While it was for the first time observed by Franken *at al.* in 1961[3], it was also the first experimental demonstration of nonlinear interaction using laser source. In this experiment, ruby laser at wavelength of 694.3 nm was focused into a crystalline quartz plate, where radiation at twice the input frequency (347.2 nm) was observed using spectrometer. The conversion efficiency of the process was about 10^{-8}. Lately, the process of second-harmonic generation reached significant practical importance. Since it can be, under proper experimental condition, generated with efficiency close to one, it can be used as an efficient source of laser radiation at various different frequencies.

Process of second-harmonic generation is second-order, three-wave, nonlinear parametric process. It can be understood as a special case of sum-frequency generation, where the two input fields are identical. Usually, the term second-harmonic generation is used only for the geometry, where both incident pump fields are indistinguishable in its frequencies and wave vectors (i.e. collinear geometry). Graphical representation of such process is schematically depicted in the figure 1.3a.

For the case of second-harmonic generation, where $\omega_1 = \omega_2 = \omega$ and $\omega_3 = 2\omega$, equation (1.17) can be rewritten as

$$P_i(2\omega) = \varepsilon_0 \sum_{jk} \chi^{(2)}_{ijk}(2\omega, \omega, \omega) E_j(\omega) E_k(\omega), \tag{1.19}$$

which can be also represented in a matrix form as

$$\begin{pmatrix} P_1 \\ P_2 \\ P_3 \end{pmatrix} = 2\varepsilon_0 \begin{pmatrix} d_{11} & d_{12} & d_{13} & d_{14} & d_{15} & d_{16} \\ d_{21} & d_{22} & d_{23} & d_{24} & d_{25} & d_{26} \\ d_{31} & d_{32} & d_{33} & d_{34} & d_{35} & d_{36} \end{pmatrix} \cdot \begin{pmatrix} E_1^2 \\ E_2^2 \\ E_3^2 \\ 2E_2E_3 \\ 2E_1E_3 \\ 2E_1E_2 \end{pmatrix}. \tag{1.20}$$

Tensor d_{il} used in the previous equation was derived from tensor $\chi^{(2)}_{ijk}$ using intrinsic permutation symmetry $\chi^{(2)}_{ijk}(\omega_3, \omega_1, \omega_2) = \chi^{(2)}_{ikj}(\omega_3, \omega_2, \omega_1)$, which for second-harmonic generation, where $\omega_1 = \omega_2$, results in $\chi^{(2)}_{ijk} = \chi^{(2)}_{ikj}$. Tensor d_{il} can be therefore introduced using following multi-index notation

$$jk : \{11, 12, 13, 21, 22, 23, 31, 32, 33\} \rightarrow l : \{1, 6, 5, 6, 2, 4, 5, 4, 3\}.$$

Finally, the factor 2 in expression (1.20) is used as a historical convention.

In previous paragraph, the intrinsic permutation symmetry was used in order to simplify the expression. This symmetry simply means, that the order of interacting field in equation (1.19) does not matter, which is for second-harmonic generation fulfilled automatically, since both pumping fields are indistinguishable. There are however other symmetries, which can simplify the expression even further. The most critical one is the inversion symmetry. If matter possess inversion symmetry, second-order nonlinear susceptibility $\chi^{(2)}$ vanishes, and therefore no second-order nonlinear processes can be generated. The reason this conclusion is significant is, that relatively large numbers of crystals possess such a symmetry. One example can be a glass without any impurities, which as a common material for optical elements make them therefore robust against second-order nonlinear processes, which are in field of linear optics considered to be parasitic*.

In previous paragraph, the influence of inversion symmetry on second-order nonlinear susceptibility was demonstrated. However, large number of other crystal spatial symmetries can be utilized in order to simplify the form of nonlinear susceptibility tensor even more. As an example, structure of second-order nonlinear tensor for KTP ($KTiOPO_4$) crystal will be presented.

KTP crystals are one of commonly used nonlinear crystals, especially for frequency doubling of solid-state lasers such as Nd:YAG, or other neodymium-doped lasers. They form

*Although, third- and higher-orders nonlinear interactions can still occur, they requires much higher optical intensity for their generation.

an orthorhombic crystal structure resulting in mm2 symmetry class. Together with Kleinman symmetry for low-frequency limit of nonresonant media[4], second-order nonlinear tensor can be represented by matrix d_{il} as

$$d_{il} = \begin{pmatrix} 0 & 0 & 0 & 0 & d_{31} & 0 \\ 0 & 0 & 0 & d_{32} & 0 & 0 \\ d_{31} & d_{32} & d_{33} & 0 & 0 & 0 \end{pmatrix}, \tag{1.21}$$

which contains only three different nonzero elements, and which significantly limits the number of possible interactions (see section 2.3.2 on page 46).

Once the form of second-order nonlinear tensor has been derived, the solution of nonlinear wave equation in such lossless nonlinear medium can be found. Let the pump field E_p be assumed in the form of a monochromatic plane wave

$$E_p(z,t) = \mathcal{E}_p e^{i(k_p z - \omega t)}. \tag{1.22}$$

This relation defines electric field as a complex quantity. Measurable physical quantity can be obtained as the real part of this complex value. As was already discussed, such an incident field will generate oscillation of dielectric polarization P_s with doubled frequency due to second-order nonlinear interaction

$$P_s(z,t) = \mathcal{P}_s e^{-i2\omega t}. \tag{1.23}$$

According to equation (1.19), the amplitude $\mathcal{P}_s$ is

$$\mathcal{P}_s = 2\varepsilon_0 d_{\text{eff}} \left(\mathcal{E}_p e^{ik_p z}\right)^2 = 2\varepsilon_0 d_{\text{eff}} \mathcal{E}_p^2 e^{i2k_p z}. \tag{1.24}$$

This oscillating polarization will then lead to the generation of an electromagnetic radiation with doubled frequency. The quantity d_{eff} from equation (1.24) represents effective nonlinear susceptibility for one particular geometry as a corresponding matrix element from expression (1.20) as $d_{\text{eff}} = \mathbf{e}_s \cdot d_{ij} : \mathbf{e}_p \mathbf{e}_p$, where $\mathbf{e}_i$ is a unit vector in direction of polarization of wave i and symbol : denotes tensor shortening. The solution of linear wave equation for optical field generated in such a way will also lead to monochromatic plane wave

$$E_s(z,t) = \mathcal{E}_s e^{i(k_s z - 2\omega t)}. \tag{1.25}$$

It can be however predicted, that nonlinear source term on the right-hand side in equation (1.12) will cause the amplitude $\mathcal{E}_s$ to be spatially dependent as a slowly varying function of z. Substituting electric vector E_s and dielectric polarization P_s in the nonlinear wave equation (1.12) with the expressions from equations (1.25), (1.23), and (1.24), following equation describing spatial evolution of generated field is obtained

$$\frac{d^2\mathcal{E}_s}{dz^2} + i2k_s \frac{d\mathcal{E}_s}{dz} = \frac{-8\omega^2 d_{\text{eff}}}{c^2} \mathcal{E}_p^2 e^{-i(k_s - 2k_p)z}. \tag{1.26}$$

Using approximation of slowly varying amplitude

$$\left|\frac{d^2\mathcal{E}}{dz^2}\right| \ll \left|k\frac{d\mathcal{E}}{dz}\right|, \tag{1.27}$$

the second derivative of amplitude $\mathcal{E}_s$ can be neglected with respect to the first derivative and final form of differential equation for second-harmonic amplitude $\mathcal{E}_s$ can be obtained as

$$\frac{d\mathcal{E}_s}{dz} = \frac{i4\omega^2 d_{\text{eff}}}{k_s c^2}\mathcal{E}_p^2 e^{i\Delta k z}. \tag{1.28}$$

Quantity $\Delta k = 2k_p - k_s$ represents phase mismatch factor, which will play very important role as will be explained later. Equation (1.28) describes space evolution of second-harmonic amplitude leading to the energy transfer from the pump field. Also equation for the pump field amplitude $\mathcal{E}_p$ can be derived in the similar way

$$\frac{d\mathcal{E}_p}{dz} = \frac{i2\omega^2 d_{\text{eff}}}{k_p c^2}\mathcal{E}_s \mathcal{E}_p^* e^{-i\Delta k z}. \tag{1.29}$$

Non-Depleting Pump Approximation

In order to show a solution for derived equations (1.28) and (1.29), non-depleting pump approximation will be used. In this approximation the pump amplitude $\mathcal{E}_p$ is considered to be constant. This assumption holds for a low efficient energy transition from pump field into second-harmonic one. This approximation leads to $d_z\mathcal{E}_p = 0$ in equation (1.29), so only equation (1.28) is needed to be considered. To calculate the evolution of second-harmonic amplitude, the equation (1.28) has to be integrated over the crystal length L in the direction of propagation z

$$\begin{aligned}\mathcal{E}_s(L) &= \frac{i4\omega^2 d_{\text{eff}}\mathcal{E}_p^2}{k_s c^2}\int_0^L e^{i\Delta k z}dz \\ &= \frac{i4\omega^2 d_{\text{eff}}\mathcal{E}_p^2}{k_s c^2}\frac{e^{i\Delta k L}-1}{i\Delta k}.\end{aligned} \tag{1.30}$$

For practical use it is necessary to calculate intensity from the amplitude. Since for a linearly polarized monochromatic plane wave in non-magnetic media, the optical intensity is given as a time-averaged magnitude of Poynting vector

$$I = \langle S\rangle = 2cn\varepsilon_0|\mathcal{E}|^2, \tag{1.31}$$

the intensity of second-harmonic can be therefore expressed as

$$\begin{aligned}I_s &= \frac{32 n_s \varepsilon_0 \omega^4 d_{\text{eff}}^2 |\mathcal{E}_p|^4}{k_s^2 c^3}\left|\frac{e^{i\Delta k L}-1}{\Delta k}\right|^2 = \\ &= \frac{8 n_s \omega^4 d_{\text{eff}}^2 I_p^2 L^2}{n_p^2 k_s^2 c^5 \varepsilon_0}\,\text{sinc}^2\left(\frac{\Delta k L}{2}\right).\end{aligned} \tag{1.32}$$

The influence of the last term $\text{sinc}^2(\Delta k L/2)$ will be discussed in the next section. Now the case of perfect phase-matching, where $\Delta k = 0$, and the sinc function is therefore equals to one will be considered. It will be shown, that such a situation is possible and it corresponds

to the most efficient energy transition from the pump field into the second-harmonic one. The efficiency of second-harmonic generation η can be now calculated as a ratio between intensities of second-harmonic and fundamental fields

$$\eta = \frac{I_s}{I_p} = \frac{2\omega^5}{k^3 c^6 \varepsilon_0} d_{\text{eff}}^2 I_p L^2, \tag{1.33}$$

where relations $n_p = n_s = n$ and $k_s = 2k_p = 2k$ were used for perfect phase-matching.

As can be excepted, the efficiency of second-harmonic generation is directly proportional to the length of the crystal L, magnitude of the nonlinear coefficient d_{eff} and intensity of incident field I_p. As it will be shown later in this chapter, these dependencies together with influence of $\text{sinc}^2(\Delta kL/2)$ factor play a key role in considering optimal experimental conditions and geometry.

Pump Depletion

Previous analysis did not take into account the depletion of the pump field. Even though this approach is valid for low efficient processes, for those, whose conversion efficiency reaches unity is not, because it results in energy conservation law violation. To treat this case properly, both equations (1.28) with (1.29) has to be solved simultaneously. A perfect phase-matching will be considered again. It is also convenient to renormalize the complex amplitude $\mathcal{E}$ as follows

$$\mathcal{A}_i = \sqrt{\frac{2cn_i\varepsilon_0}{\hbar\omega_i}}\mathcal{E}_i, \tag{1.34}$$

since the squared amplitude $\mathcal{A}^2$ is then equal to photon flux density ϕ ($[\phi] = \text{photon}/(\text{sm}^2)$)

$$\phi_i = |\mathcal{A}_i|^2 = \frac{I_i}{\hbar\omega_i}. \tag{1.35}$$

Equations (1.28) and (1.29) can be thus rewritten as

$$\frac{d\mathcal{A}_p}{dz} = i2\kappa\mathcal{A}_s\mathcal{A}_p^*, \tag{1.36a}$$

$$\frac{d\mathcal{A}_s}{dz} = i\kappa\mathcal{A}_p^2, \tag{1.36b}$$

where

$$\kappa^2 = \frac{\hbar\omega^6 d_{\text{eff}}^2}{\varepsilon_0 k^3 c^6} \tag{1.37}$$

is so-called coupling parameter. Obtained equations (1.36a) and (1.36b) have to be solved with appropriate boundary conditions, which for second-harmonic generation of presented geometry are:

(i) no second-harmonic field at the input of the crystal

$$\mathcal{A}_s(0) = 0 \tag{1.38}$$

(ii) energy conservation during the interaction

$$|\mathcal{A}_p(z)|^2 + 2|\mathcal{A}_s(z)|^2 = |\mathcal{A}_p(0)|^2. \tag{1.39}$$

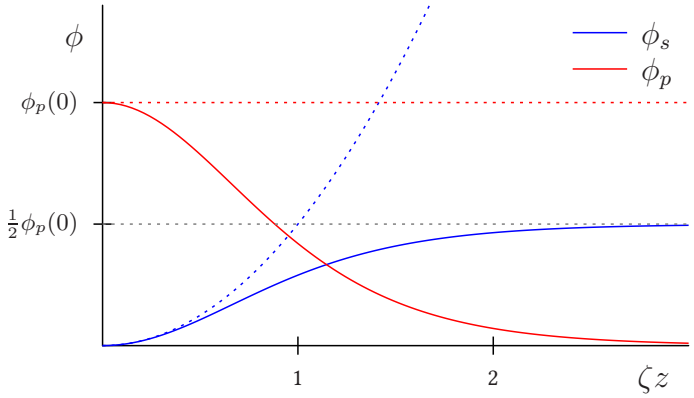

FIGURE 1.4: Spatial evolution of photon flux of both interacting fields in process of second-harmonic generation demonstrating photon number conservation $\phi_p(0) = \phi_p(z) + 2\phi_s(z)$. Dashed lines represent approximation of non-depleted pump.

Considering these two conditions, the solution can be found in the following form

$$\mathcal{A}_p(z) = \mathcal{A}_p(0)\text{sech}\left(\sqrt{2}\kappa\mathcal{A}_p(0)z\right), \tag{1.40a}$$

$$\mathcal{A}_s(z) = \frac{1}{\sqrt{2}}\mathcal{A}_p(0)\tanh\left(\sqrt{2}\kappa\mathcal{A}_p(0)z\right). \tag{1.40b}$$

Using equation (1.35), spatial variation of the photon flux density can be calculated as

$$\phi_p(z) = \phi_p(0)\text{sech}^2(\zeta z), \tag{1.41a}$$

$$\phi_s(z) = \frac{1}{2}\phi_p(0)\tanh^2(\zeta z), \tag{1.41b}$$

where $\zeta = \sqrt{2}\kappa\mathcal{A}_p(0)$. The efficiency of second-harmonic generation with depleted pump field can be then calculated from equation (1.41b) using expression (1.35) as a ratio between optical intensity of second-harmonic field at the output of the crystal and the pump field at the input as

$$\eta = \frac{I_s(L)}{I_p(0)} = \frac{\hbar\omega_s\phi_s(L)}{\hbar\omega_p\phi_p(0)} = \tanh^2(\zeta L). \tag{1.42}$$

As a consequence of these results, all the input pump photons can be converted into only half as many second-harmonic output photons as shown on plot in the figure 1.4, which is in agreement with energy conservation law. For high values of product ζL, the efficiency η approaches unity, where all pump power is transmitted into second-harmonic field. On the other hand, for low values of product ζL, the approximation $\tanh(x) \approx x$ can be used. In this approximation the expression (1.42) gets the form of (1.33), derived in the non-depleted pump power approximation.

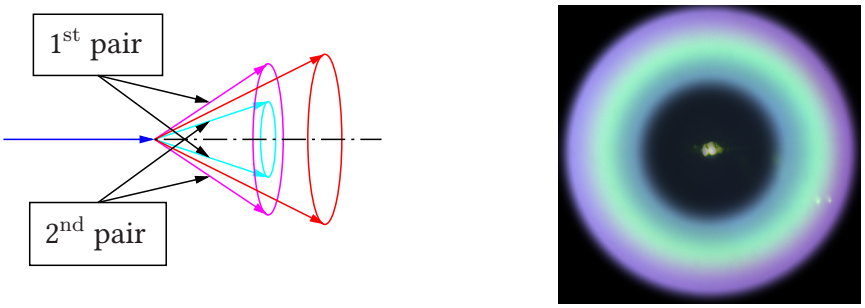

(a) (b)

Figure 1.5: (a) Schematic illustration of photon pairs creation in the process of spontaneous parametric down-conversion. (b) Image taken in real experiment with BBO nonlinear crystal pumped by fs OPA in UV region.

1.3.3 Spontaneous Parametric Down-Conversion

In previous section, process of second-harmonic generation was discussed. In this section, another second-order nonlinear effect, the process of spontaneous parametric down-conversion (SPDC) or shortly parametric fluorescence will be explored. This process was for the first time observed by Burnham *at al.* in ADP crystal using He-Cd laser at 325 nm in 1970[5].

Process of parametric down-conversion can be seen from two different perspectives. From the first perspective, it can be considered as time-reverse process to second-harmonic generation (or better to the sum-frequency generation). From the second perspective, it can be described as a special case of parametric amplification (or different-frequency generation) without the presence of a seeded field, where only vacuum fluctuations are amplified. Both these approaches are physically identical.

In contrast with the sum-frequency generation, where two photons from pump field are destroyed, while one photon with doubled frequency is created, here one photon is annihilated and one pair of two photons is created instead (see sketch in the figure 1.5a). For historical reasons, these photons are called *signal* and *idler*. Because the two photon comprising one pair originate from one pump photon, they are highly correlated both in space and time[*].

In the case of sum-frequency generation, both frequency ω and wave vector $\mathbf{k}$ are determined from frequencies and wave vectors of input fields, and where different combinations of these frequencies and wave vectors can create the same sum-frequency field. Here in the case of spontaneous parametric down-conversion however the same one pump field can create photon pairs with various frequencies and wave vectors. As a consequence, this process is highly broadband as illustrated in the figure 1.5b.

[*] In fact, these photons can be correlated in several other degrees of freedom as well.

Classical Description of Parametric Fluorescence

In order to describe this process theoretically, similar set of coupled differential equations has to be derived from wave equation (1.12) in the same manner as in the case of second-harmonic generation. Since the parametric fluorescence is spontaneous two-photon emission, the efficiency is relatively low. Pump field amplitude $\mathcal{E}_p$ can be therefore considered to be constant over the interaction*. In this case, following set of coupled equations for generated amplitudes $\mathcal{E}_s$ (signal) and $\mathcal{E}_i$ (idler) is obtained

$$\frac{d\mathcal{E}_s}{dz} = \frac{2i\omega_s^2 d_{\text{eff}}}{k_s c^2}\mathcal{E}_p\mathcal{E}_i^* e^{i\Delta kz}, \tag{1.43a}$$

$$\frac{d\mathcal{E}_i}{dz} = \frac{2i\omega_i^2 d_{\text{eff}}}{k_i c^2}\mathcal{E}_p\mathcal{E}_s^* e^{i\Delta kz}, \tag{1.43b}$$

where $\Delta k = k_p - k_s - k_i$. In order to solve this equations, a perfectly phase-matched interaction ($\Delta k = 0$) will be assumed. Since equations (1.43a) and (1.43b) are formally identical, also formally same solution is expected. The general solution can be found in the following form

$$\mathcal{E}_j(z) = \alpha \sinh(\kappa z) + \beta \cosh(\kappa z), \tag{1.44}$$

where

$$\kappa^2 = \frac{4\omega_s^2\omega_p^2}{k_s k_p c^4}|\mathcal{E}_p|^2 \tag{1.45}$$

is again coupling constant for parametric down-conversion and values of integration constants α and β depend on the appropriate boundary conditions, which for the case of spontaneous parametric down-conversion require no generated fields at the input of the crystal $\mathcal{E}_s(0) = \mathcal{E}_i(0) = 0$. The solutions can be therefore written as follows

$$\mathcal{E}_s(z) = \mathcal{E}_s(0)\cosh(\kappa z) - i\mathcal{E}_i^*(0)\sinh(\kappa z), \tag{1.46a}$$

$$\mathcal{E}_i(z) = \mathcal{E}_i(0)\cosh(\kappa z) - i\mathcal{E}_s^*(0)\sinh(\kappa z). \tag{1.46b}$$

This solution is valid for any parametric amplification process. For the first sight it may be surprising as a solution for parametric down-conversion, since with expected boundary conditions $\mathcal{E}_s(0) = \mathcal{E}_i(0) = 0$, no output field is generated. The reason for this is, that down-converted photons are created as amplification of vacuum fluctuations, which can not be explained using classical approach, and where quantum mechanical apparatus has to be involved.

Quantum Description of Parametric Fluorescence

Essentially, in order to derive quantum description of spontaneous parametric down-conversion, the classical pump, signal, and idler fields has to be substituted with operators. This substitution for the field envelopes can be formally expressed as $\mathcal{E}_j(z) \to \hat{a}_j(z)$, where $\hat{a}_j(z)$

*Here, only so-called low-gain regime is considered, however later also high-gain regime will be introduced, where the conversion efficiency is much higher, so the pump field is depleting and it thus can not be considered constant any more (see section 5.4.2 on page 89).

is annihilation operator and $j = s, i$. Annihilation and creation operators $\hat{a}_j^\dagger(z)$ of the field have to fulfil commutation relations

$$\left[\hat{a}_p(z), \hat{a}_q^\dagger(z)\right] = \delta_{pq}, \tag{1.47a}$$

$$\left[\hat{a}_p(z), \hat{a}_q(z)\right] = 0, \tag{1.47b}$$

where $\{p, q\} = \{s, i\}$. Using this notation, the photon flux density operator $\hat{I}(z)$ can be also derived as $\hat{I}_j(z) = \hat{a}_j^\dagger(z)\hat{a}_j(z)$, giving the mean numbers of photons per unit area.

It can be shown, that for three-wave mixing of type $\hbar\omega_p = \hbar\omega_s + \hbar\omega_i$, the time-independent interaction Hamiltonian has the following form

$$\hat{H} = \hbar\chi^{(2)}\left(\hat{p}^\dagger\hat{s}\hat{i} + \hat{p}\hat{s}^\dagger\hat{i}^\dagger\right), \tag{1.48}$$

where operators $\hat{p}, \hat{s}, \hat{i}$ and $\hat{p}^\dagger, \hat{s}^\dagger, \hat{i}^\dagger$ represent annihilation and creation operators for fundamental, signal, and idler fields, respectively. If pump field is assumed as a strong coherent state $E_p(t) = \mathcal{E}_p e^{-i\omega_p t}$, the interaction Hamiltonian (1.48) can be rewritten as

$$\hat{H} = \hbar\chi^{(2)}\left(E_p^*\hat{s}\hat{i} + E_p\hat{s}^\dagger\hat{i}^\dagger\right). \tag{1.49}$$

Time evolution of a signal field can be in Heisenberg picture represented via commutator as

$$\begin{aligned}\frac{d\hat{s}}{dt} &= -\frac{i}{\hbar}\left[\hat{s}, \hat{H}\right] \\ &= -i\chi^{(2)}\left[\hat{s}\left(E_P^*\hat{s}\hat{i} + E_p\hat{s}^\dagger\hat{i}^\dagger\right) - \left(E_P^*\hat{s}\hat{i} + E_p\hat{s}^\dagger\hat{i}^\dagger\right)\hat{s}\right] \\ &= -i\chi^{(2)}E_p\hat{i}^\dagger.\end{aligned} \tag{1.50}$$

The same expression can be derived in the same way also for the idler field

$$\frac{d\hat{i}}{dt} = -i\chi^{(2)}E_p\hat{s}^\dagger. \tag{1.51}$$

Since these equations are formally identical to these obtained with classical approach (see equations (1.43a) and (1.43b)), the solution can be written directly as

$$\hat{s}(t) = \hat{s}(0)\cosh(\chi^{(2)}E_p t) - i\hat{i}^\dagger(0)\sinh(\chi^{(2)}E_p t), \tag{1.52a}$$

$$\hat{i}(t) = \hat{i}(0)\cosh(\chi^{(2)}E_p t) - i\hat{s}^\dagger(0)\sinh(\chi^{(2)}E_p t). \tag{1.52b}$$

Although as can be seen this solution is formally identical to the one obtained using classical approach, the difference is hidden in the second term on the right-hand side. Even if the input fields are in vacuum states, signal and idler photons can be generated due to the presence of the creation operators. In other words, the classical approach requires for down-conversion existence of a seeding, however quantum mechanics shows, that spontaneous generation of photon pairs can be seeded only by the vacuum fluctuations.

Using this semiclassical approach, average photon numbers for the signal and idler fields can be calculated. From time dependent first order perturbation results

$$\langle n_s(t)\rangle = \langle n_s(0)\rangle\cosh^2\left(\frac{1}{2}G_0 t\right) + (1 + \langle n_i(0)\rangle)\sinh^2\left(\frac{1}{2}G_0 t\right), \tag{1.53a}$$

$$\langle n_i(t)\rangle = \langle n_i(0)\rangle\cosh^2\left(\frac{1}{2}G_0 t\right) + (1 + \langle n_s(0)\rangle)\sinh^2\left(\frac{1}{2}G_0 t\right), \tag{1.53b}$$

where

$$G_0 = 8\pi d_{\text{eff}} \sqrt{\frac{cI_p(0)}{2\varepsilon_0 n_p n_s^2 n_i^2 \lambda_s \lambda_i}} \frac{\sin\left(\frac{\Delta kL}{2}\right)}{\frac{\Delta kL}{2}} \tag{1.54}$$

it can be seen, how is the generation of signal and idler photons driven by the pump field through the nonlinear polarization even without presence of input fields. Using time to space transformation $t \rightarrow \sqrt{n_s n_i}(z/c)$, formula for spatial evolution of phase-matched, spontaneously generated down-converted fields can be obtained

$$\langle n_{s,i}(z) \rangle = \sinh^2(gz), \tag{1.55}$$

where the amplification factor g

$$g = 4\pi d_{\text{eff}} \sqrt{\frac{I_p(0)}{2\varepsilon_0 c n_p n_s n_i \lambda_s \lambda_i}} \tag{1.56}$$

is the so-called parametric gain.

1.4 Phase Matching

Until now only the case of perfectly phase-matched process, where Δk is equal to zero was discussed. Here the amplitude of generated field grows linearly during the propagation through the nonlinear medium* (see figure 1.4). This is a consequence of all atomic dipoles inside a nonlinear media oscillating with the same phase, so each component of second-harmonic field generated by individual dipoles in different parts of the nonlinear medium interfere constructively and as the result the energy transition from pump filed into second-harmonic field is the most efficient.

In this section, the influence of the phase mismatch factor $\Delta k \neq 0$ on the efficiency of nonlinear interactions, especially on second-harmonic generation will be discussed. As can be seen from equation (1.32), the intensity of second-harmonic generation I can be written as

$$I_s = I_s^{(\max)} \text{sinc}^2 \left(\frac{\Delta kL}{2} \right), \tag{1.57}$$

where $I_s^{(\max)}$ represents maximal intensity generated in the case of perfect phase-matching. Equation (1.57) is plotted in the figure 1.6, from where it is evident, that the phase-mismatch significantly reduces the efficiency of second-harmonic generation, or better the maximal length of nonlinear media. It can be also seen, that for given phase-mismatch Δk, the length of the crystal has to be reduced in order to maintain the same conversion efficiency. In other words, for longer crystal, the phase-matching condition is more strict. It is therefore convenient to define so-called coherence length $L_c = \pi/\Delta k$ as an interaction length, where the conversion efficiency is still high enough. On the contrary if the interaction length L is longer than the coherence length L_c, the generated field gets out of phase with the source polarization $\mathbf{P}^{(\text{NL})}$, and energy will therefore flow back into the pump field as illustrated in

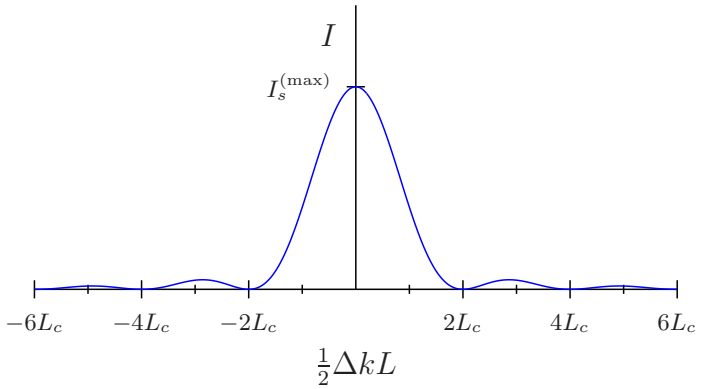

Figure 1.6: Dependence of conversion efficiency of second-harmonic generation with non-zero phase mismatch Δk on phase-mismatch factor $(1/2)\Delta kL$

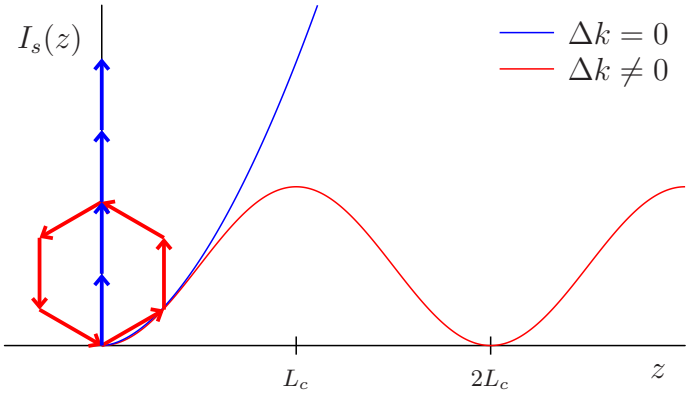

Figure 1.7: Evolution of second-harmonic intensity I_s for the case of perfect (blue line) and non-perfect (red line) phase-matching. It can be seen, that for the case of perfect phase-matching, the intensity grows monotonically (with square of distance), however for non-perfect phase-matching it oscillates periodically with period $2L_c$. The graph also contains a phasor representation of an interference of particular contributions from different positions along the crystal.

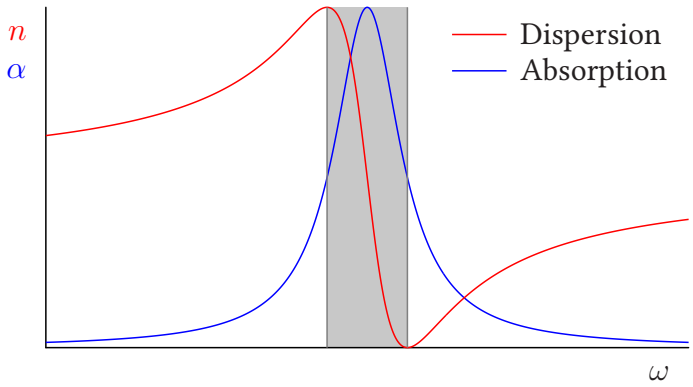

Figure 1.8: Frequency dependent coefficient of absorption α and index of refraction n. Gray-filled area represents spectral range of anomalous dispersion, which also corresponds to high absorption.

the figure 1.7. Coherence length L_c for process of second-harmonic generation can be also rewritten using formula $\Delta k = (2\pi/\lambda)(n_s - n_p)$, where λ is wavelength of fundamental field in the vacuum and n_p and n_s are refractive indices of fundamental and second-harmonic field, respectively. Using this formula, coherence length $L_c = \lambda/4(n_s - n_p)$ is clearly inversely proportional to material dispersion of nonlinear medium.

Since the factor sinc^2 from the equation (1.57) is a consequence of interference between waves generated in different parts of the nonlinear crystal, in order to achieve perfect phase-matching, fundamental wave (and therefore also nonlinear polarization $\mathbf{P}^{(\mathrm{NL})}$) has to propagate through the nonlinear media with the same phase shift as second-harmonic wave. Let it be shown, that for a collinear geometry of second-harmonic generation, the formula $\Delta k = k_p - 2k_s = 0$ results in following condition

$$\begin{aligned} k_p &= 2k_s \\ \frac{\omega_p n_p(\omega_p)}{c} &= 2\frac{\omega_s n_s(\omega_s)}{c}\bigg|_{\omega_p = 2\omega_s} \\ n_p(\omega_p) &= n_s(\omega_s). \end{aligned} \tag{1.58}$$

This condition requires the refractive indices for fundamental and second-harmonic fields to be identical. This condition however can not be fulfilled in standard material in the spectral region of normal dispersion, where the index of refraction n increases monotonically with angular frequency ω (see figure 1.8). The same analysis can be performed for all second-order nonlinear interactions, and although the final formulas will differ, the conclusion will be still the same.

There are however several approaches, that can be used in order to achieve perfect phase-matching. The fist one is to use material in region of anomalous dispersion, where condition (1.58) can be fulfilled (see figure 1.8). It is well known however, that region of anomalous

*Under the approximation of strong, non-depleted pump field.

dispersion coincides with the region of high absorption, and therefore most of the gained radiation would be lost due to the losses. Because of that (and the fact, that it would significantly restrict the interaction wavelengths) this technique is not practically used.

The second possibility is to utilized birefringence of anisotropic crystals. It can be shown, that birefringent materials can fulfil condition (1.58) for different combination of polarization of interacting fields. Even though this technique possess some disadvantages like a necessity to use anisotropic materials only and the fact, that the geometry of the experiment is restricted by the phase-matching condition, it is the most common approach in achieving perfectly phase-matched interactions.

The last approach presented here in this section is called quasi-phase-matching. As can be suspected, it is not as good as perfect-phase matching, however the monotonic growth of generated amplitude along the nonlinear crystal can be achieved. The main advantage of this approach is its versatility. Since the quasi-phase-matching device has to be designed individually in order to fit each particular interaction, almost any process can be quasi-phase-matched even using isotropic materials, or combination of identically polarized interacting fields.

1.4.1 Birefringence

In this paragraph, the phase-matching using birefringence in anisotropic media will be discussed.

In anisotropic medium, the refractive index (and therefore phase velocity) depends on polarization and direction of propagation. Although the polarization may change as the wave is propagating through the crystal, there exists, in general, two directions, where polarization remains unchanged. These directions are called optical axes. In anisotropic media, the Maxwell's equations are typically solved for propagation of monochromatic plane wave with angular frequency ω. As a result, the Fresnel's equation is obtained[6]

$$\frac{n_x^2 s_x^2}{n^2 - n_x^2} + \frac{n_y^2 s_y^2}{n^2 - n_y^2} + \frac{n_z^2 s_z^2}{n^2 - n_z^2} = 0, \tag{1.59}$$

where n is refractive index in direction of propagation given by unit vector $\mathbf{s} = \{s_x, s_y, s_z\}$ and n_x, n_y, n_z are the principal refractive indices. This equation represents three-dimensional surface consisting of two shells, which touch in four points (see the figure 1.9). Optical axes are then directions joining two of them and passing through the origin. In any random direction of propagation, two different refractive indices for two orthogonally polarized waves therefore exist as can be also seen from the figure 1.9. This represents a general case of so-called biaxial crystals with two different optical axes and with normal surface described with three principal refractive indices n_x, n_y, and n_z. Since the convention of labelling refractive indices of biaxial crystals is $n_x < n_y < n_z$, both optical axes lie in xz plane.

In many cases, two of the principal refractive indices are equal. The two principal indices are called *ordinary* (n_o) and *extraordinary* (n_e). In this case the crystal is called uniaxial, with

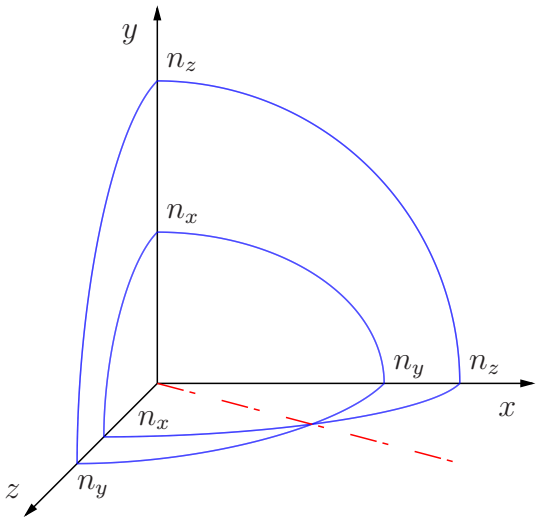

Figure 1.9: The normal surface of a biaxial crystal. The blue curves demonstrate the intersections of two shells with a coordinate planes. The red dash-doted line represents an optical axis.

the normal surface characterized by following formula

$$\frac{n_o^2(s_1^2+s_2^2)}{n^2-n_o^2}+\frac{n_e^2 s_3^2}{n^2-n_e^2}=0, \tag{1.60}$$

where $n_o^2 = \varepsilon_x/\varepsilon_0 = \varepsilon_y/\varepsilon_0$ and $n_e^2 = \varepsilon_z/\varepsilon_0$. The normal surface in this case consists of one sphere and one ellipsoid, which touch each other on z axis, which is therefore the only one optical axis. Uniaxial crystals are divided into two groups: (i) positive, where $n_e > n_o$ and (ii) negative, where $n_e < n_o$.

For the derivation of phase-matching condition a positive uniaxial crystals will be here considered. It can be shown[7], that value of refractive index of extraordinary wave propagating in any arbitrary direction given by angle θ, can be calculated using following formula

$$\frac{1}{n_e^2(\theta)}=\frac{\cos^2\theta}{n_o^2}+\frac{\sin^2\theta}{n_e^2}. \tag{1.61}$$

Since it is necessary to achieve different refractive indices for all interacting waves, it is clear, that also different directions of polarization will be involved. The table 1.1 summaries all possible combinations of direction of polarization for uniaxial crystal, and therefore types of interaction. Furthermore, also process of Type 0 can be defined as interaction of waves with the same polarization.

The basic idea for collinear geometry of second-harmonic generation is well depicted in the figure 1.10, which demonstrate the phase-matching in positive uniaxial crystal. For both fundamental and second-harmonic field the crystal possess two refractive indices $n_o^{(p)}$, $n_e^{(p)}$ and $n_o^{(s)}$, $n_e^{(s)}$, respectively. Since in positive crystal $n_o < n_e$, the pump wave will propagate

	Positive crystal			Negative crystal		
	Pump	Signal	Idler	Pump	Signal	Idler
Type I	o	e	e	e	o	o
Type II	o	o	e	e	e	o

Table 1.1: Table of interactions types based on directions of polarization of an interacting waves.

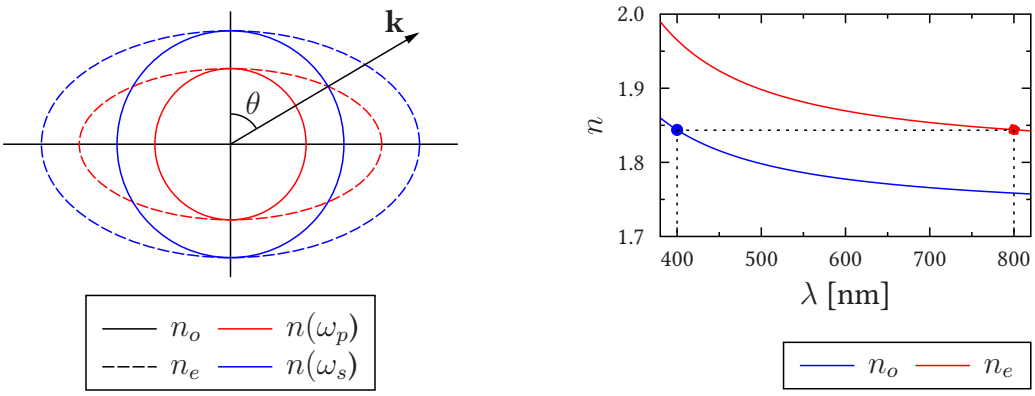

(a) (b)

Figure 1.10: Demonstration of phase-matching in positive uniaxial crystal. (a) Optimal direction of propagation represented by angle θ between optical axis and wave vector $\mathbf{k}$, where $n_e(\omega) = n_o(2\omega)$. (b) Dispersion of refractive indices of uniaxial crystal. Dashed line represents a phase-matching of frequency doubling at 800 nm.

as an extraordinary wave, while the second-harmonic as an ordinary one. Under proper orientation of the crystal (i.e. angle θ between optical axis and propagation direction), condition $n_e(\omega, \theta) = n_o(2\omega)$ can be fulfilled, where the angle can be obtained using formula (1.61). This method is, of course, usable only if dispersion (causing phase mismatch) and birefringence are in the same order.

Because this technique requires rotating of the crystal, it is known as angle tuning. There are several drawbacks of this method. First, it requires specific polarization of interacting waves, second, it needs a particular orientation of the crystal, which can lead to utilization of lower nonlinear coefficient, and finally, it suffers from phenomenon called walk-off.

In birefringent media, where angle between direction of propagation and optical axis is neither 0°, nor 90°, the Poynting vector is not parallel with the wave vector (see the figure 1.11). As a result, the ordinary and extraordinary waves diverge from each other. Walk-off therefore limits the spatial overlap of interacting fields and in consequence the effective length of nonlinear crystal.

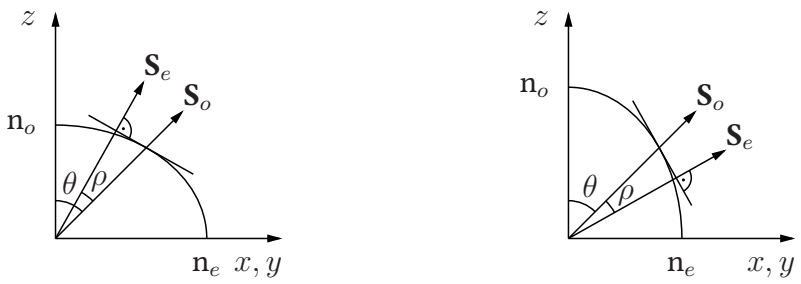

(a) Positive (b) Negative

Figure 1.11: Illustration of spatial walk-off in uniaxial positive (a) and negative (b) crystal, where the direction of Poynting vector of the ordinary and of the extraordinary wave represented by vectors $\mathbf{S}_o$ and $\mathbf{S}_e$, respectively is deflected due to the birefringence of the material by angle $\rho = (1/n_e)(\partial n_e/\partial\theta)$.

One solution to that is to use materials with strong dependence of extraordinary refractive index on temperature. Such a method is called temperature tuning (or non-critical phase-matching) and is often used, for instance, for crystals inside the cavities of the lasers, where angle tuning of crystal would cause instability of the resonator.

1.4.2 Quasi-Phase-Matching

Quasi-phase-matching as a technique to synchronize phases of interacting field was for the first time introduced by Armstrong in 1962[8]. Although it was invented shortly after invention of the laser in 1960[9] and the first observation of second-harmonic generation in 1961[3], it could not be used that time and had to waited until a suitable fabrication methods had been developed.

As already mentioned, the phase-matching technique utilizing birefringence has several serious limits. The most important one is, that it requires anisotropic materials, with orientation restricted by the phase-matching condition. In this case, since the material is anisotropic and nonlinear coefficients depends on experimental geometry, usually not the highest nonlinear coefficient is used, which results in lower conversion efficiency. The highest nonlinear coefficients are usually d_{33}, which can be used only when mixing waves with identical polarization, which is not possible to phase-matched using solely birefringence. Moreover, there can be materials with nonlinearity higher in orders of magnitude, but with birefringence not strong enough to compensate for the dispersion, and therefore not able to fulfil the phase-matching condition. In all these mentioned cases, the quasi-phase-matching can be found as a suitable solution.

The idea behind the quasi-phase-matching is quite simple. If there exists some natural phase mismatch Δk, an additional factor K can be artificially added to compensate the natural phase mismatch. For three wave mixing the quasi-phased-matching condition can be

therefore presented as

$$k_3 - k_1 - k_2 - K = 0, \tag{1.62}$$

where $K = \Delta k = \pi/L_c$. It can be shown, that such a factor can be obtained using so-called periodically-poled materials, where sign of nonlinear coefficient d_{eff} is periodically inverted along the propagation direction creating a square function

$$d(z) = d_{\text{eff}}\,\text{sign}\left[\cos\left(\frac{2\pi}{\Lambda_{\text{PM}}}z\right)\right], \tag{1.63}$$

where $\Lambda_{\text{PM}} = 2L_c$ represents the period of the modulation and d_{eff} is an effective nonlinear coefficient of non-inverted media.

As known from Fourier analysis, any periodic function can be described in terms of Fourier series

$$d(z) = d_{\text{eff}} \sum_{m=-\infty}^{\infty} d^{(m)} e^{iK^{(m)}z}, \tag{1.64}$$

where $K^{(m)} = 2\pi m/\Lambda_{\text{PM}}$ represents m-th order of periodic modulation and $d^{(m)} = (2/m\pi)\sin(m\pi/2)$ scales the effective nonlinear coefficient of m-th order $d_{\text{eff}}^{(m)}$ as $d_{\text{eff}}^{(m)} = d_{\text{eff}}\, d^{(m)}$. Since the nonlinear coefficient is no longer independent on z, the coupled differential equations have to be handle in proper manner. Final form for amplitude of second-harmonic $\mathcal{E}_s$ from equation (1.28) can be therefore derived as follows

$$\frac{d\mathcal{E}_s}{dz} = \frac{i4\omega^2 d_{\text{eff}}^{(m)}}{k_s c^2}\mathcal{E}_p^2 e^{i\Delta k^{(m)}z}, \tag{1.65}$$

where $\Delta k^{(m)} = 2k_s - k_p - K^{(m)}$ is a new phase mismatch factor. As can be seen now, proper spatial modulation of nonlinear media can lead to vanishing natural phase-mismatch originating from material dispersion of nonlinear media. The resulting spatial variation of second-harmonic intensity within the crystal is illustrated in the figure 1.12. Moreover, even though it is better to achieve quasi-phase matching through the first order of periodic modulation $K^{(1)}$ (since quantity $d^{(m)}$ decreases with m, and therefore reduces effective nonlinear coefficient), higher-orders of this modulation can be also utilized. In special cases, more orders can be utilized in the same time, which can lead to a versatile source of nonlinear processes (see chapter 2 on page 33).

One way, how to introduce such a spatial modulation of nonlinear susceptibility is process of periodic poling. With this technique, a non-modulated nonlinear crystal is used. Using a lithographic process, periodic mask of electrodes is created on the top and bottom surface. Applying strong electrostatic field in order of $\text{kV}\,\text{mm}^{-1}$, the orientation of ferroelectric domains, and thus the orientation of crystalline axis is reversed in regions under the electrodes, resulting in reversing sign of effective nonlinear coefficient (see the figure 1.13). This technique is however obviously limited to ferroelectric materials (materials containing spontaneous electric polarization, i.e. internal electric dipoles) with reasonable widths (so the electric field can penetrate the material as uniformly as possible) and with poling periods limited by the lithography precision.

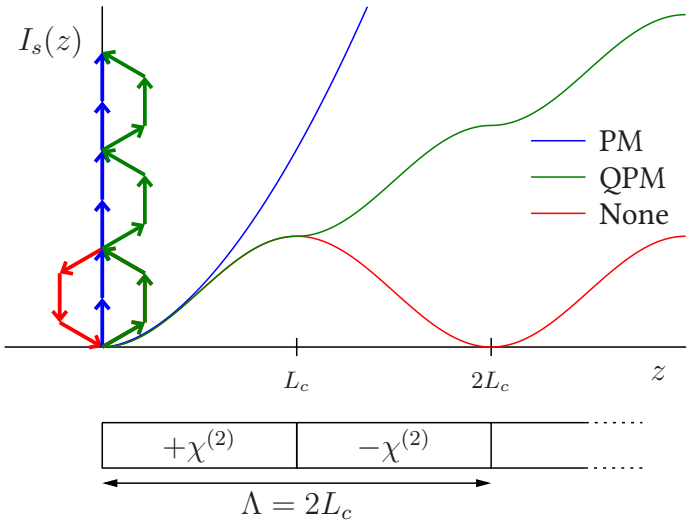

Figure 1.12: Spatial evolution of second-harmonic field generated in the case of phase-matched (blue line) and quasi-phase-matched (green line) interaction as well as for phase-mismatched one (red line). It can be seen, that even though for the quasi-phase-matching the efficiency is lower than for the perfect phase-matching, a monotonic increase of intensity can be obtained. The phasor representation of the interactions together with schematic illustration of optimal periodical poling is also presented.

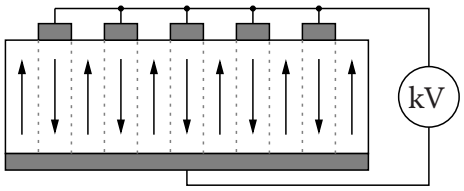

Figure 1.13: Demonstration of periodic poling technique. Ferroelectric domains orientation represented with arrows was under grey electrodes reversed by applying a strong electrostatic field.

1.4.3 Modal Phase-Matching

Besides these methods, there exist also not that common techniques which usually utilize some non-standard geometry or other property of the experiment. Phase-matching techniques in waveguides may serve as an example, where the light is propagating in form of guided modes or better as a combination of guided and radiated modes.

The classical modal phase-matching (MPM) is taking advantage of an effective modal refractive index n_{eff} from $\beta = n_{\text{eff}}(2\pi/\lambda_0)$, where β is the propagating constant of particular mode and $(2\pi/\lambda_0)$ is the vacuum wavenumber, being dependent not only on the wavelength, but also on the mode in which the light propagates. Due to this dependence the condition $n_{\text{eff}}(\omega) = n_{\text{eff}}(2\omega)$ can be fulfilled, thus the phase mismatch eliminated simply by using different guided modes of the waveguide. However, from this requirement immediately arises the main drawback of this technique. Different spatial modes have different amplitude distribution over the transverse plane of the waveguide, which limits the spatial overlap of the interaction and in consequence lower the overall conversion efficiency, especially when higher modes have to be involved. Nevertheless, if fundamental mode is used with combination with one of the lowest mode, the nonlinear interaction can be obtained with reasonably high efficiency[10].

Previous technique uses different guided modes, and it is therefore limited to multimodal waveguides only. However, there exists also different modal phase-matching method, where the phase mismatch gets vanished for combination of guided and radiated modes. This method is called Cherenkov phase-matching. In this type of phase-matching (for the case of second-harmonic generation) the fundamental wave propagates as a guided mode, while the second-harmonic is generated as a radiated one, i.e. it propagates out of the waveguide core into the cladding or substrate at angle θ determined by the phase velocity match $\theta = n_{\text{eff}}(\omega)/n_{\text{eff}}(2\omega)$. As can be shown[11], this can be obtained only if the phase velocity of the fundamental mode in the core is higher than the phase velocity of the radiated mode in the cladding. Since this is analogous to the phenomenon of Cherenkov radiation, where the speed of particle, which emits radiation is larger than the speed of light in the material the particle is propagating through, it explains the choice of name for this technique. Also this type of phase-matching has been treated both theoretically[12,13] and experimentally[14,15].

1.5 Practical Experimental Approach

In previous section, the model based on plane waves and spatially unlimited nonlinear medi-um was used. In real experiments however, the dimensions of both interacting fields together with the nonlinear material itself is usually under some restrictions. Essentially, there are two main possibilities of experimental implementation*. The first one uses bulk crystals with finite dimensions pumped by an optical beams, the other one take advantages of a wave-guiding structures, in which all interacting fields exist in form of guided modes. Both approaches benefits from some advantage features and suffers from another ones. For instance, experiments with bulk crystals are much more simple from experimental point

*Here, the nonlinear interactions on boundaries, for instance, were not considered

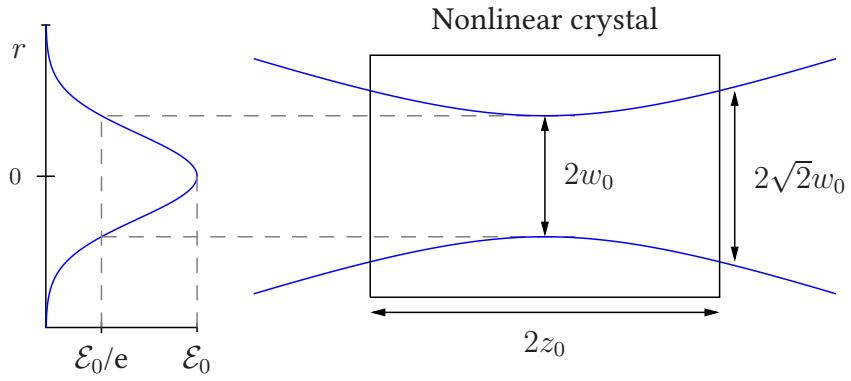

Figure 1.14: Illustration of optimal focusing of Gaussian beam into the nonlinear crystal. $2z_0$: Rayleigh range, $2w_0$: beam waist.

of view, both angle and temperature tuning for phase-matching are accessible and non-collinear geometry can be utilized in order to spatially separate the interacting beams or fulfil the phase-matching condition.

On the other hand, waveguides can provide much higher conversion efficiency thanks to usually higher power density and longer interaction length. Also since waveguides from definition supports only collinear interactions, the quasi-phase-matching is usually employed, even though the modal phase-matching could be in principle utilized. As a consequence, Type 0 interaction can be used and the highest nonlinear coefficient d_{33} utilized, which results in even higher conversion efficiency.

1.5.1 Bulk Crystals

In this paragraph, generation of second-harmonic field inside the bulk crystal using Gaussian beam will be discussed. From beginning, laser sources have been almost exclusively used as a sources for nonlinear optics. The reason was their high power density, which is an essential ingredient for efficient parametric generation. Since the lasers produce light in form of beams, it is straightforward to use them with a bulk crystal as a source of nonlinear processes.

Because the efficiency of phase-matched second-harmonic generation is directly proportional to the interaction length and inversely proportional to the cross section area of the interaction

$$\eta \simeq d_{\mathrm{eff}}^2 L^2 \frac{P_p}{A}, \tag{1.66}$$

where $P_p/A = I_p$ (compare with formula (1.33)), long crystal should be used, where the beam should be tightly focused in order to obtain maximal conversion efficiency. However, as it is depicted in the figure 1.14, there is a trade-off between these two requirements. With increasing of interaction length, the beam size is increasing also, which results in lowering the conversion efficiency. In other words, focusing limits the interaction length. As a re-

sult, there has to be optimal amount of focusing for given length of the crystal producing the highest conversion efficiency.

If the crystal length is much shorter than Rayleigh range z_0, beam size remains almost constant and plane-wave model can be adopted. As already shown, optical intensity of second-harmonic generation for perfectly phase-matched interaction can be express as

$$|\mathcal{E}_s(2\omega)|^2 = \frac{8n\varepsilon_0\omega_4 d_{\text{eff}}^2 L^2}{k^2 c_3}|\mathcal{E}_p(\omega, r)|^4, \tag{1.67}$$

where pump field amplitude $\mathcal{E}_p(\omega, r)$ is expressed in form of Gaussian beam

$$\mathcal{E}_p(\omega, r) \simeq \mathcal{E}_0 e^{-(r^2/w_0^2)}. \tag{1.68}$$

Now, the conversion efficiency can be calculated using formula $\eta = P_s(2\omega)/P_p(\omega)$, where $P(\omega) = (1/2)\sqrt{(\varepsilon_0/\mu_0)}\int |\mathcal{E}(\omega)|^2 dr$. It can be shown[16], that the second-harmonic field is effectively generated only within the confocal area (Rayleigh range) of the focused beam. The reason is not only the fact, that the beam width is expanding, but also because of angular spread of wave vectors, which induces additional phase-mismatch. It can be also shown[7], that the second-harmonic field is generated also in form of Gaussian beam with beam waist and angular diffraction $\sqrt{2}$ times smaller than the ones of the pump beam.

The final conversion efficiency of second-harmonic generation in the case of so-called confocal focusing can be found in form[16]

$$\eta_{\text{conf.}} = \frac{128\pi^2\omega^3 d_{\text{eff}}^2 L}{n^2 c^4} P(\omega), \tag{1.69}$$

where comparing with plane-wave solution from equation (1.33), the linear dependence on L instead on L^2 can be seen.

1.5.2 Waveguides

Although the bulk crystals are still used the most frequently, interest in nonlinear waveguides has been rising rapidly lately. There are several reasons to prefer guiding structures for nonlinear interactions. From the formula for conversion efficiency of second-harmonic generation (1.66) it can be seen, that for given pump power nonlinear material with the highest nonlinearity, or if the material is already given its orientation, in which the highest nonlinear coefficient is utilized has to be used in order to achieve the highest efficiency of the generation. Also the longest possible interaction length together with the smallest cross section of interaction area i.e. the highest power density is required. It can be shown, that all of these requirements can be very well matched in nonlinear waveguides.

However, even though the nonlinear waveguides may seem to be superior to bulk crystals, they are still not used that often. The reason is their lower variability, since they are usually designed for one particular application. Also it is more difficult to handle them experimentally. As a result, they are usually used in stand-alone devices like harmonic generators, OPAs, OPOs, and so on, while in laboratory proof-of-principle experiments, the bulk crystals still plays the key role. Since the waveguides are in general significantly more compact

with respect to bulk crystals, one more reason for them to become part of the complex stand alone devices is their ability to be integrated into compact optical circuits, which can nowadays consists of almost any optical component.

In order to utilize the most of the potential benefits of the nonlinear waveguides, they are usually periodically-poled, so highly nonlinear materials can be used. In the case of bulk crystals, the material is chosen not only with respect to its nonlinearity, but also to its anisotropy. There is however a large amount of materials with high nonlinear coefficients, however with no or to low birefringence to compensate the dispersion causing the phase-mismatch. On the other hand, even in the material, where the dispersion can be compensated there exist directions with higher nonlinear coefficients. To utilize them requires mixing of optical waves polarized in the same direction (Type 0 interaction). With periodic poling, any dispersion, and thus any phase mismatch can be compensated with no need for anisotropy. Therefore, almost any material in any direction with any combination of interacting polarization can be used. Table 1.2 summarized some of frequently used nonlinear media and its nonlinear coefficient in order to compare different materials not only through their nonlinearity, but their dispersion also.

Furthermore, the probably most important feature, that makes waveguides one of the most efficient sources of nonlinear processes is their possibility to reach extremely long interaction lengths. As was already discussed in previous section, the length of bulk crystals is limited by the pumping beam geometry and it is usually in orders of units of mm. In waveguides, where once the light is coupled in, it can propagate any long distance, limited only by the internal losses, while keeping its amplitude profile constant as a consequence of existing in form of superposition of guided modes. The typical length of nonlinear waveguides vary from application to application. There are such, that are only several millimetres long, the most common lengths are however in units of cm. Nevertheless, there are also cases, where the nonlinear waveguide can be several meters long, or even longer. As an example can serve a weakly doped glass fibers. Although the glass poses inversion symmetry, so no second-order nonlinear process can be generated there, some impurities can destroy this symmetry and second-order susceptibility $\chi^{(2)}$ therefore does not vanish. As a consequence, such a fiber can be used as a nonlinear medium. Although, the induced nonlinearity is extremely low, together with long interaction length and high power density within the core of the fiber, reasonably high conversion efficiency can be reached.

Moreover, the guided modes are usually well located inside small waveguide cores, with cross section dimensions typically in units of μm^2 resulting in very high power densities and as a consequence high conversion efficiency again.

Modal Structure of Guided Waves

All previous assumptions were derived based on model of a plane wave. Inside a waveguide, the electromagnetic field however does not exist in form of plane wave, but in form of guided modes. Although formally similar results are to be expected, proper mathematical treatment has to be adopted in order to describe properties of electromagnetic radiation guided inside of these structures.

Material	Nonlinear coefficients	Refractive indices at 1064 nm	Refractive indices at 532 nm
$KTiOPO_4$	d_{31} = 1.95 pm V^{-1}	n_x = 1.7400	n_x = 1.7787
(KTP)	d_{32} = 3.9 pm V^{-1}	n_y = 1.7469	n_x = 1.7924
	d_{33} = 15.3 pm V^{-1}	n_z = 1.8304	n_x = 1.8873
$LiIO_3$	d_{15} = 2.2 pm V^{-1}	n_o = 1.8571	n_o = 1.8982
		n_e = 1.7165	n_e = 1.7480
BaB_2O_4	d_{22} = 2.22 pm V^{-1}	n_o = 1.6551	n_o = 1.6750
(BBO)	d_{31} = 0.16 pm V^{-1}	n_e = 1.5426	n_e = 1.5555
LiB_3O_5	d_{31} = 1.09 pm V^{-1}	n_x = 1.5656	n_x = 1.5787
(LBO)	d_{32} = 1.17 pm V^{-1}	n_y = 1.5905	n_x = 1.6065
		n_z = 1.6055	n_x = 1.6212
KH_2PO_4	d_{36} = 0.43 pm V^{-1}	n_o = 1.4938	n_o = 1.5125
(KDP)		n_e = 1.4599	n_e = 1.4705
$ZnGeP_2$	d_{21} = 111 pm V^{-1}	n_o = 3.2324	n_o = 3.1141
		n_e = 3.2786	n_e = 3.1524
$AgGaSe_2$	d_{11} = 43 pm V^{-1}	n_o = 2.7005	n_o = 2.6140
		n_e = 2.6759	n_e = 2.5824
$AgGaS_2$	d_{34} = 31 pm V^{-1}	n_o = 2.4508	n_o = 2.3954
		n_e = 2.3966	n_e = 2.3421
GaSe	d_{21} = 63 pm V^{-1}	n_o = 2.9082	n_o = 2.8340
		n_e = 2.5676	n_e = 2.4599

Table 1.2: Table of frequently used nonlinear materials, sizes of their nonlinear coefficients, dispersion, and birefringence.

At the beginning of this chapter, nonlinear effects were formally described using nonlinear wave equation with particular form of input field. In the case of waveguides, the very same approach will be used with the exception, that proper form of interacting field has to be found first.

Formal solution of waveguides can be done in following manner. First, any component of guided electromagnetic field propagating along z direction can be expressed in form

$$\mathbf{E} = \mathcal{E}(u, v)e^{i(\omega t - \beta z)}, \tag{1.70a}$$

$$\mathbf{H} = \mathcal{H}(u, v)e^{i(\omega t - \beta z)}, \tag{1.70b}$$

where β denotes propagating constant, unique quantity for particular mode at frequency ω and (u, v) is any orthogonal coordinate system. It can be shown[17], that the longitudinal

components of the field must obey scalar Helmholtz wave equation

$$\left[\Delta_t + (\omega^2\varepsilon\mu - \beta^2)\right] \begin{bmatrix} E_z \\ H_z \end{bmatrix} = 0, \tag{1.71}$$

where $\Delta_t = \partial_u^2 + \partial_v^2$ is transverse component of Laplace operator, and where the homogeneous and isotropic media was expected.

Any solution of this equation has to also fulfil the following boundary conditions:

(i) longitudinal component of electric vector **E** and magnetic intensity **H** has to be continuous on boundary of any two media

(ii) longitudinal component of electric vector **E** has to be zero on surface of a conductor

(iii) ratio between longitudinal components of electric vector **E** and magnetic intensity **H** has to be equal to the surface impedance

(iv) radiation condition $\lim_{r\to\infty} |\mathbf{E}|^2 = \lim_{r\to\infty} |\mathbf{H}|^2 = 0$ has to be fulfilled.

Any complete solution must include not only guided modes, but also a radiated ones. In general, the solution for vector of electric field in lossless media can be written in following form

$$\mathbf{E}_t(u,v,z) = \underbrace{C\mathbf{E}_t^{(r)}(u,v,z)}_{\text{radiated modes}} + \underbrace{\sum_p A_p \mathbf{E}_{tp}^{(g)}(u,v)e^{-i\beta_p z}}_{\text{guided modes}}, \tag{1.72}$$

where any combination of guided modes in this solution has to obey following orthogonal relations

$$\int \mathbf{E}_{tp} \cdot \mathbf{E}_{tq}^* du dv = 0, \tag{1.73a}$$

$$\int \mathbf{e}_z \cdot (\mathbf{E}_{tp} \times \mathbf{H}_{tq}) du dv = 0, \tag{1.73b}$$

where indices p, q represents any combination of orthogonal modes and $\mathbf{e}_z$ is the unit vector in z direction. As a consequence, any optical field can be in any z plane expressed as a sum of independent orthogonal modes (superposition property).

Fulfilling this set of boundary conditions leads to a transcendental equation for ω and β, which if solved yields to dependence $\beta = \beta(\omega)$ known as a dispersion relation. This relation thereafter carry information about dispersion characteristics of given mode such as phase velocity ω/β, group velocity $\partial\omega/\partial\beta$, and group velocity dispersion $\partial^2\omega/\partial\beta^2$. For dielectric waveguides with reasonable refractive indices it can be concluded, that at given frequency ω, only limited number of modes can be excited, and that in any waveguide at least one fundamental mode exists.

Helmholtz equation (1.71) can be solved using separation of variables method, where longitudinal components of the electromagnetic field are expressed as

$$\begin{bmatrix} E_z \\ H_z \end{bmatrix} = \begin{bmatrix} \mathcal{E}(u,v) \\ \mathcal{H}(u,v) \end{bmatrix} e^{\pm i\beta z} = \mathcal{U}(u)\mathcal{V}(v)e^{\pm i\beta z}, \tag{1.74}$$

where optimal choice of function $\mathcal{U}(u)$ and $\mathcal{V}(v)$ depends on shape of the particular waveguide. For instance, in the case of rectangular waveguide, the solution will be in form of harmonic functions $\mathcal{U}(x) = e^{\pm ik_x x}$ and $\mathcal{V}(y) = e^{\pm ik_y y}$. On the other hand, for waveguides with circular symmetry, the cylindrical coordinate system (r, θ, z) can be used and the solution found in form $\mathcal{U}(r) = Z_\nu^{(1),(2)}(pr)$ and $\mathcal{V}(\theta) = e^{\pm i\nu\theta}$, where $Z_\nu^{(1),(2)}$ are two independent solution of Bessel differential equation of ν-th order (i.e. Bessel functions) and $p = \omega^2\varepsilon\mu - \beta^2$.

In previous paragraph, the formal analytic solution for homogeneous waveguides was introduced. However, many structures, especially these used in nonlinear optics are inhomogeneous, where $[\varepsilon, \mu] = [\varepsilon, \mu](\mathbf{r})$. In this case, a new wave equation for inhomogeneous matter has to be derived. It can be shown[7], that such an equation will have following form

$$\nabla \times \nabla \times \mathbf{E} - \frac{\nabla\mu(\mathbf{r})}{\mu(\mathbf{r})} \times \nabla \times \mathbf{E} - \omega^2\varepsilon(\mathbf{r})\mu(\mathbf{r})\mathbf{E} = 0, \tag{1.75}$$

where $\nabla \cdot [\varepsilon(\mathbf{r})\mathbf{E}] = 0$. This wave equation can be, however, solved analytically, as expected, only for limited number of particular dependencies $[\varepsilon, \mu] = [\varepsilon, \mu](\mathbf{r})$, (i.e. limited number of refractive index profiles). For any other cases, a numerical approach has to be adopted.

Numerical Solution of Inhomogeneous Waveguides

Although analytic solution can be found for some simple profiles of index of refraction, for general case a numerical approach has to be adopted.

In order to solve eigenvalue problems for inhomogeneous waveguides, several numerical methods have been developed. Two most frequently used are finite-elements method and final-difference method. The first one, method of final-elements can be used for inhomogeneous waveguides of any cross section. It is based on numerical solution of full set of Maxwell's equations with appropriate boundary conditions. The results are therefore accurate, except of numerical precision. This method is based on splitting transverse profile of the structure into small parts, where the material can be assumed to be sufficiently homogeneous. On the borders, the boundary conditions are used in order to bond the solutions together.

On the other hand, method of finite-differences uses a full system of three-dimensional Maxwell's equations with appropriate boundary conditions, which are solved in temporal domain. The equations are expressed in linearised form using final-differences. The field inside the structure is developing in time steps through the space areas with rectangular shapes. Also here, the accuracy is limited only by the numerical precision.

2

Second-Harmonic Generation in Periodically-Poled KTP Waveguide

Periodically-poled KTP waveguide and its experimental characterization will be presented in this chapter. Simultaneous existence of three different types of nonlinear processes of second-harmonic generation will be shown, and both, the spatial and spectral properties of generated fields will be studied. Experimental results will be interpreted using numerical model based on a scalar finite-elements method, which was adopted in order to calculate spatial mode profiles, propagation constants, and frequencies of interacting fields. Developed model will be also used to address the influence of waveguide parameters on second-harmonic spectra. It will be shown, that there exist correlations between spatial and spectral properties of coupled modes. In the end, the switching between individual processes using spatial and spectral filtering will be demonstrated.

In this chapter, the research published in paper by Machulka *et al.* [18] will be reported. In this paper one can also find more details especially about numerical model and also further references concerning this topic.

2.1 Introduction

The process of second-harmonic generation can be in principal produced in any nonlinear material lacking the inversion symmetry. Phase-matching of interacting fields can be reached through the birefringence of anisotropic media, or via quasi-phase-matching (QPM) as suggested by Armstrong[8]. QPM holds however several advantages, especially allowing for the highest nonlinear coefficients to be utilized[19]. The quasi-phase-matching itself is usually introduced by periodic poling, where dielectric domains inside ferroelectric material are inverted by intense electrostatic field[20,21]. As a consequence of inverting dielectric domains,

also signs of nonlinear susceptibility $\chi^{(2)}$ are inverted. Second-order nonlinearity can be therefore approximated with a dichotomic function, which as a result produces desired additional factor K into quasi-phase-matching condition $\Delta k = k_s - 2k_p - K$ (see section 1.4.2 on page 23).

Since the dichotomic function is periodic, it can be expanded into series containing also higher harmonic orders. Even though the nonlinear structure is designed only for the first-order to be utilized and potential higher-order contributions are usually considered as parasitic[22], the rich spatial and spectral modal structure can be exploited if several higher-order harmonics are significant enough[23]. As a consequence, properties of nonlinear interactions can be taken under control. In this study, utilization of the first-, the second-, and the third-order of harmonic modulation will be presented.

Since the efficiency of second-harmonic generation is inversely proportional to the transverse area of the interaction, focusing of the pump beam into the nonlinear medium may improve the efficiency. Focusing has however some optimal value given by spatial walk-off and angular spread of wave vectors. Oppose to bulk crystals, the fields inside the waveguides, which are not affected by the walk-off[24], are confined into usually vary small areas resulting in very high power densities[25]. Moreover, waveguides can offer much longer phase-matched interaction length, which results in further increase of the conversion efficiency.

The fundamental difference between bulk crystals and waveguides is however the presence of guided modes. If the cross section dimensions of the waveguide are big enough for the structure to be multimodal at employed wavelength, the propagation of not only the fundamental mode, but also higher modes is supported. In this case, a modal phase-matching (MPM) relying on phase velocity matching (i.e. modal dispersion) between different modes can be utilized together with quasi-phase-matching. Since each mode possess different propagation constant, the phase-matching condition, and therefore efficient second-harmonic generation, can be reached for several combinations of these spatial modes[26–28] at once. For any of these combinations, certain spatial and also spectral properties of fundamental beam are needed.

Here, second-harmonic generation pumped by pulsed laser source will be studied. The second-harmonic field is therefore excepted to be polychromatic, with the spectral profile determined by the spectral profile of the fundamental field giving, if considering only energy conservation relation, formula $\Delta\lambda_s = (\sqrt{2}/4)\Delta\lambda_p$. To observe signal spectral profile $\Delta\lambda_s$, the width of the pump $\Delta\lambda_p$ has to be however larger, since the phase-matching conditions put additional constraints to the nonlinear process.

The differences in both spectral and spatial profiles of interacting fields can be afterwards useful in tuning a specific nonlinear process. Besides the phase-matching conditions, also a sufficient spatial overlap of interacting modes is necessary. This disqualifies higher modes, whose amplitude oscillate quickly in transverse plane of the waveguide. So even though the higher modes can propagate through the structure, only the lower modes are therefore expected to be generated. As a consequence, different nonlinear processes caused by different orders of involved spatial nonlinearity modulation together with different combination of interacting spatial modes can coexist in periodically-poled nonlinear waveguide together.

This research was motivated by the fact, that waveguides have become more popular in real applications, since they can be integrated into more complex miniaturized optical circuits. Because of that, the potential influence of manufacture imperfections on the properties of generated fields was also investigated. Here presented characterization through the process of second-harmonic generation can be further used also for the inverse process of spontaneous parametric down-conversion[26,28,29].

2.2 Theory

Both the fundamental and generated second-harmonic fields represented by their electric field amplitudes E_p and E_s, respectively have to inside the waveguide obey nonlinear wave equation[1,30]

$$\nabla \times (\nabla \times \mathbf{E}_i) + \frac{\overleftrightarrow{\varepsilon}}{c^2}\frac{\partial^2 \mathbf{E}_i}{\partial t^2} = -\mu_0 \frac{\partial^2 \mathbf{P}^{(2)}}{\partial t^2}, \tag{2.1}$$

where ∇ is del operator and $\overleftrightarrow{\varepsilon}$ denotes tensor of linear permittivity, which is assumed to have a diagonal form in used Cartesian coordinate system $\{x, y, z\}$. Constant c in equation (2.1) represents the speed of light in vacuum and μ_0 is the permeability of vacuum. Second-order nonlinear polarization $\mathbf{P}^{(2)}$ can be expressed as $\mathbf{P}^{(2)} = 2\varepsilon_0 \overleftrightarrow{d} : \mathbf{E}_p\mathbf{E}_p$, where $\overleftrightarrow{d}$ represents the third-order nonlinear tensor and symbol : stands for tensor shortening.

Both polychromatic fields can be spectrally decomposed as follows

$$\mathbf{E}_i(x, y, z, t) = \sum_n \sum_m \int \mathcal{E}^{(i)}_{nm}(z, \omega_i)\mathbf{e}^{(i)}_{nm}(x, y, \omega_i)e^{i(\beta^{(i)}_{nm}(\omega_i)z - \omega_i t)}d\omega. \tag{2.2}$$

The normalized amplitudes $\mathbf{e}^{(i)}_{nm}(x, y, \omega_i)$ represent the mode functions and can be found as a solutions to corresponding Helmholtz equation. More precisely, solving the Helmholtz equation represents eigenvalue problem, where the mode functions act as the eigenfunctions, while the propagation constants $\beta^{(i)}_{nm}$ as the corresponding eigenvalues. The first summation over n in equation (2.2) represents the summation over two differently polarized modes, (quasi-) TE and (quasi-) TM[31], while the second summation over m runs over all possible transverse guided modes. Finally, $\mathcal{E}^{(i)}_{nm}(z, \omega_i)$ denotes the envelope of spectral amplitude of corresponding mode propagating in z direction. The (quasi-) TE means, that the mode has the electric field vector polarized in direction nearly parallel to the x axis, while for (quasi-) TM modes the electric field vector is nearly perpendicular to the x axis.

Substituting the decomposed electric fields from equation (2.2) into the nonlinear wave equation (2.1), a set of nonlinear differential equations for the envelopes $\mathcal{E}^{(i)}_{nm}$ is obtained. Using approximations of slowly varying amplitude and non-depleting pump, following formula for amplitude of second-harmonic field $\mathcal{E}^{(s)}_{ak}(L, \omega_s)$ at the output of the waveguide is obtained

$$\mathcal{E}^{(s)}_{ak}(L, \omega_s) = i\left(\frac{\omega_s}{\beta^{(s)}_{ak}(\omega_s)c}\right)^2 \sum_{b,c}\sum_{l,m}\int D^{abc}_{klm}(\omega_s, \omega_p)\Gamma^{abc}_{klm}(L, \omega_s, \omega_p)\times$$
$$\times\, \mathcal{E}^{(p)}_{bl}(0, \omega_p)\mathcal{E}^{(p)}_{cm}(0, \omega_s - \omega_p)d\omega_p, \tag{2.3}$$

where integration over frequencies ω_p incorporates all frequency contributions present in the polychromatic pump field. The coefficients $D^{abc}_{klm}(\omega_s, \omega_p)$ introduced in equation (2.3) are defined as

$$D^{abc}_{klm}(\omega_s, \omega_p) = d_M \iint \overleftrightarrow{d} : \mathbf{e}^{(s)*}_{ak}(x, y, \omega_s)\mathbf{e}^{(p)}_{bl}(x, y, \omega_p)\mathbf{e}^{(p)}_{cm}(x, y, \omega_s - \omega_p)dxdy. \tag{2.4}$$

This coefficient represents weakly frequency dependent effective nonlinear coefficient, which among the polarization properties incorporates also a spatial overlap of all interacting fields. The coefficient d_M in equation (2.4) denotes the amplitude of decomposition of the actual spatial modulation of nonlinear coefficient into the M-th order of quasi-phase-matching. As already mentioned, the effective nonlinear coefficient $D^{abc}_{klm}(\omega_s, \omega_p)$ is usually small if it incorporates higher-order spatial modes due to a frequent changes in the sigh of their electric field amplitudes. Finally, the coupling coefficient $\Gamma^{abc}_{klm}(L, \omega_s, \omega_p)$ from equation (2.3) is defined as

$$\Gamma^{abc}_{klm}(L, \omega_s, \omega_p) = i\frac{e^{-i\Delta\beta^{abc}_{klm}(\omega_s,\omega_p)L} - 1}{\Delta\beta^{abc}_{klm}(\omega_s, \omega_p)}. \tag{2.5}$$

It characterize the evolution of generated field along the z axis. The $\Delta\beta^{abc}_{klm}(\omega_s, \omega_p)$ from equation (2.5) represents the phase mismatch, and therefore determines the efficiency of the generation. It is defined as follows

$$\Delta\beta^{abc}_{klm}(\omega_s, \omega_p) = \beta^{(s)}_{ak}(\omega_s) - \beta^{(p)}_{bl}(\omega_p) - \beta^{(p)}_{cm}(\omega_s - \omega_p) - \frac{2\pi M}{\Lambda_{\mathrm{PM}}}, \tag{2.6}$$

where the last contribution $2\pi M/\Lambda_{\mathrm{PM}}$ originates in the M-th harmonic of periodic modulation of nonlinear coefficient.

2.2.1 Spatial Profiles of Guided Modes

In order to calculate spatial profiles of the field guided by the structure, the profile of refractive index has to be known. This section will therefore contain description and basic properties of nonlinear element used for this particular research.

PP-KTP-WG Element

The element used in this study was periodically-poled KTP chip fabricated by AdvR Inc. with about 50 waveguides created on its top surface (for detailed images see figure 2.1).

The KTP ($KTiOPO_4$) nonlinear crystals are commonly used nonlinear materials due to their high optical quality, broad transparency window, and high damage threshold (for more detailed description see table 2.1). All here mentioned features together with relatively high nonlinearity makes them adequate choice for frequency doubling of solid-state lasers, particularly at low or medium power densities or an optical parametric oscillator for near IR generation. Moreover, they are suitable especially as an electro-optic modulators or as any optical waveguide devices.

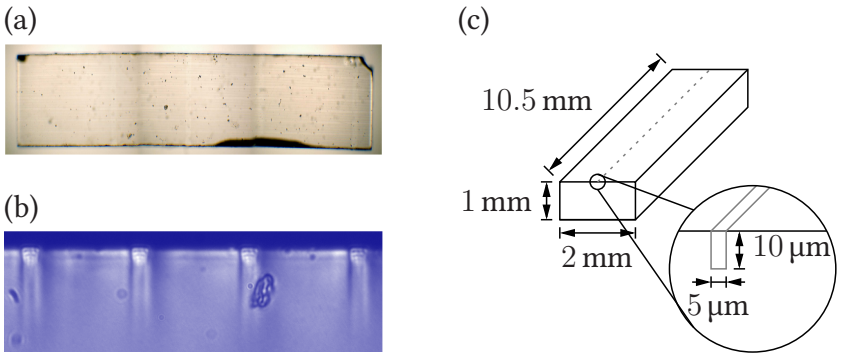

Figure 2.1: Periodically-poled KTP waveguide used in this experiment: (a) top view, (b) front facet of the chip, and (c) schematic sketch of the element with its dimensions. On both real images, waveguides together with some damages in the substrate can be identified.

Transparency range	350 nm to 4500 nm
Crystal structure	orthorhombic
Point group	mm2
Non-linear coefficient	d_{31} = 1.4 pm V^{-1}
	d_{32} = 2.65 pm V^{-1}
	d_{33} = 10.7 pm V^{-1}
Refractive index @ 800 nm	n_x = 1.75719, n_y = 1.84546
@ 400 nm	n_x = 1.84435, n_y = 1.96775
Optical damage threshold	500 MW cm^{-2} @ 1064 nm, 20 ns, 20 Hz

Table 2.1: The main optical properties of KTP nonlinear crystals.

In the fabrication process, an ordinary bulk KTP crystal with dimensions $10.5 \times 2 \times 1$ mm^3 was used as a substrate. The substrate was firstly periodically-poled using lithographic technique as described in the previous chapter (section 1.4.2, page 23). The poling period was chosen to fulfil quasi-phase-matching condition for Type II frequency doubling at 800 nm (800 nm $\rightarrow$ 400 nm). The manufacturer considered the optimal value of the poling period for this interaction to be 7.62 µm. After that, the waveguides were formed by Rb^+ ion diffusion through another lithographic mask. The diffused ions locally raise the refractive index and as a consequence form the waveguide with numerical aperture about 0.2.

In the fabrication process, both horizontal and vertical dimensions of the future waveguide are under control. The horizontal dimension is controlled through the mask boundaries and stays relatively stable due to highly anisotropic ion diffusion in vertical direction. On the other hand in the vertical dimension, the profile depends on the ion concentration, which decreases with the distance from the top surface and once it is temporally stable it can be approximated with the error function[32]. It can be shown[24,32,33], that the refractive index profile

of waveguide formed with this technique can be approximated with following function

$$\begin{aligned} n_\xi(x,y)\big|_{y\geq 0} &= n_{\xi 0} + \Delta n_\xi \mathrm{Rect}_{[w]}(x)\mathrm{Erfc}\left(\frac{y}{h}\right), \\ n_\xi(x,y)\big|_{y<0} &= 1, \end{aligned} \tag{2.7}$$

where $n_{\xi 0}$ denotes the refractive index of the KTP substrate and Δn_ξ is step in refractive index on the top of the waveguide with respect to undoped material. The values for refractive indices used for later calculations can be found in the table 2.1. Operators $\mathrm{Rect}_{[w]}(x)$ and $\mathrm{Erfc}(y/h)$ from equation (2.7) represent the rectangular function equal to unity on the interval $\langle -w/2; w/2\rangle$ and zero elsewhere and the error function of height h, respectively. As can be seen from formula (2.7), the air is assumed above the waveguide. The index $\xi = x, y, z$ indicate the anisotropic behaviour of the KTP crystal, which is assume to be oriented in such a way, that only diagonal elements of linear susceptibility ($\varepsilon_x, \varepsilon_y, \varepsilon_z$) are nonzero, and where the crystallographic axes $\{x_c, y_c, z_c\}$ coincide with used coordinate system $\{z, x, y\}$. The refractive indices can be therefore expressed as $n_\xi = \sqrt{\varepsilon_\xi}$.

The dimensions w, h of the waveguide were obtain experimentally using white light coupling inside the waveguide to excite all guided spatial modes. The intensity profile measured at the output face of the waveguide was then compared with the profile calculated by the model (see figure 2.2). Based on this comparison, the waveguide dimension $w = 5\,\mu\mathrm{m}$ and $h = 10\,\mu\mathrm{m}$ was obtained, which was found in good agreement with values specified by the manufacturer.

Equations for Spatial Profiles of Guided Modes

In order for the spatial profiles of guided optical fields to be determined, the electric field vector is usually used because of its larger magnitude. However, due to the spatial profile of refractive index, the solution can be found more easily using magnetic field represented by the vector of magnetic intensity **H**. Moreover, obtained equations are also symmetrical for both polarizations in this case.

It can be shown, that magnetic field has to obey appropriate linear wave equation

$$\nabla \times \left(\frac{1}{\overleftrightarrow{\varepsilon}} \times \mathbf{H}\right) = -\frac{1}{c^2}\frac{\partial^2 \mathbf{H}}{\partial t^2}. \tag{2.8}$$

The vector of magnetic intensity can be expressed as $\mathbf{H}(x,y,z,t) = \mathbf{h}(x,y,\omega)e^{i(\beta z - \omega t)}$, where quantity $\mathbf{h}(x,y,\omega)$ represents magnetic field envelope of particular guided mode characterized by its frequency ω and propagation constant β. Substituting this expression into the wave equation (2.8), following set of coupled differential equations for transverse mode

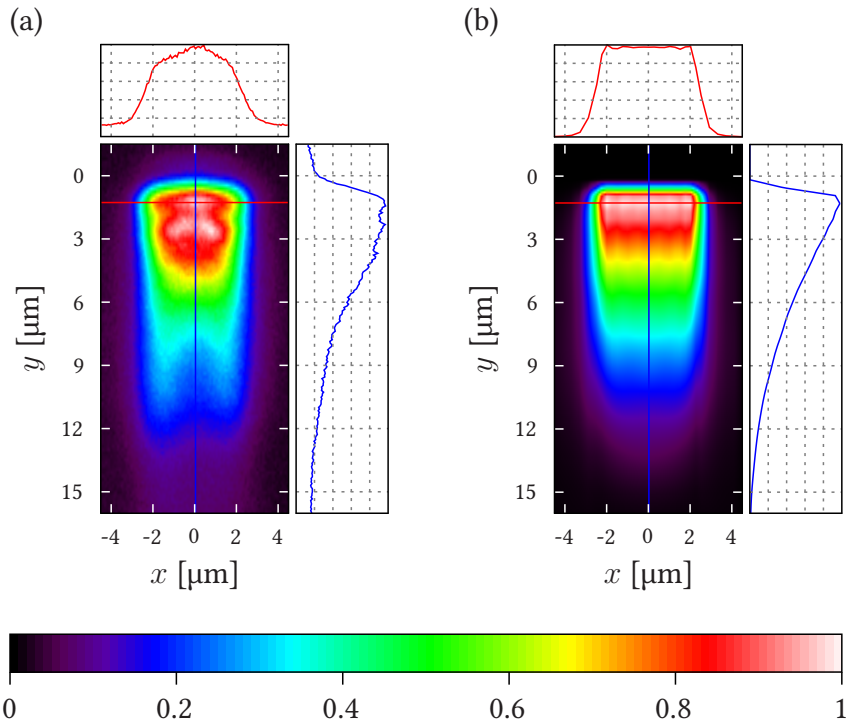

Figure 2.2: Topo graphs of intensity $I_t = |\mathcal{E}_t|^2$ in the transverse plane of the waveguide in the case of thermal light propagation. Intensity profiles along both horizontal and vertical slices indicated in the topo graphs are also shown. (a) Experimental result obtain after white light coupling, (b) theoretical prediction based on numerical model.

components $\mathbf{h}_x$ and $\mathbf{h}_y$ can be obtained

$$\frac{1}{\varepsilon_y}\frac{\partial^2 \mathbf{h}_x}{\partial x^2} + \frac{1}{\varepsilon_z}\frac{\partial^2 \mathbf{h}_x}{\partial y^2} + \frac{1}{\varepsilon_y}\frac{\partial^2 \mathbf{h}_y}{\partial x \partial y} - \frac{1}{\varepsilon_z}\frac{\partial^2 \mathbf{h}_y}{\partial y \partial x} - \left[\frac{\partial \mathbf{h}_y}{\partial x} - \frac{\partial \mathbf{h}_x}{\partial y}\right]\frac{\partial}{\partial y}\left(\frac{1}{\varepsilon_z}\right) = \left(\frac{\beta^2}{\varepsilon_y} - k_0^2\right)\mathbf{h}_x, \tag{2.9a}$$

$$\frac{1}{\varepsilon_z}\frac{\partial^2 \mathbf{h}_y}{\partial x^2} + \frac{1}{\varepsilon_x}\frac{\partial^2 \mathbf{h}_y}{\partial y^2} + \frac{1}{\varepsilon_x}\frac{\partial^2 \mathbf{h}_x}{\partial y \partial x} - \frac{1}{\varepsilon_z}\frac{\partial^2 \mathbf{h}_x}{\partial x \partial y} + \left[\frac{\partial \mathbf{h}_y}{\partial x} - \frac{\partial \mathbf{h}_x}{\partial y}\right]\frac{\partial}{\partial x}\left(\frac{1}{\varepsilon_z}\right) = \left(\frac{\beta^2}{\varepsilon_x} - k_0^2\right)\mathbf{h}_y, \tag{2.9b}$$

where $k_0 = \omega/c$, and where relation $\mathbf{h}_z = i(\partial_x \mathbf{h}_x + \partial_y \mathbf{h}_y)/\beta$ originating from Maxwell's equation $\nabla \mathbf{H} = 0$ was considered. The desired electric field amplitudes can be in the end calculated from Maxwell's equation as

$$\mathbf{e}(x, y, \omega) = \frac{1}{\overleftrightarrow{\varepsilon}\varepsilon\omega} i\nabla \times \mathbf{h}(x, y, \omega) - \beta \mathbf{z} \times \mathbf{h}(x, y, \omega), \tag{2.10}$$

where **z** denotes the unit vector in direction of propagation. It can be show, that the cross contributions

$$\frac{1}{\varepsilon_y}\frac{\partial^2 \mathbf{h}_y}{\partial x \partial y}, \quad \frac{1}{\varepsilon_z}\frac{\partial^2 \mathbf{h}_y}{\partial y \partial x}, \quad \left[\frac{\partial \mathbf{h}_y}{\partial x} - \frac{\partial \mathbf{h}_x}{\partial y}\right]\frac{\partial}{\partial y}\left(\frac{1}{\varepsilon_z}\right),$$
$$\frac{1}{\varepsilon_x}\frac{\partial^2 \mathbf{h}_x}{\partial y \partial x}, \quad \frac{1}{\varepsilon_z}\frac{\partial^2 \mathbf{h}_x}{\partial x \partial y}, \quad \left[\frac{\partial \mathbf{h}_y}{\partial x} - \frac{\partial \mathbf{h}_x}{\partial y}\right]\frac{\partial}{\partial x}\left(\frac{1}{\varepsilon_z}\right)$$

from equations (2.9a) and (2.9b) can be omitted, since they are usually very small, and thus does not contribute significantly[34]. As a consequence, two independent equations for (quasi-) TE and (quasi-) TM modes are obtained

$$\frac{\partial^2 \mathbf{h}_x}{\partial x^2} + \frac{\varepsilon_y}{\varepsilon_z}\frac{\partial^2 \mathbf{h}_x}{\partial y^2} = \left(\beta^2 - \varepsilon_y k_0^2\right)\mathbf{h}_x, \tag{2.11a}$$

$$\frac{\varepsilon_x}{\varepsilon_z}\frac{\partial^2 \mathbf{h}_y}{\partial x^2} + \frac{\partial^2 \mathbf{h}_y}{\partial y^2} = \left(\beta^2 - \varepsilon_x k_0^2\right)\mathbf{h}_y. \tag{2.11b}$$

Derived equations (2.11a) and (2.11b) can now be treated independently. These equations can be however solved analytically only for some certain profiles of permittivity $\overleftrightarrow{\varepsilon}$[26,31,35]. For real waveguides however, the numerical approach has to be usually used. In order to do that, several numerical methods has been developed[34], nevertheless the finite-element and finite-difference method[34,36] have become the most popular ones among the others. Here, the finite-element method based on Galerkin method[34] has been developed[18].

Using developed numerical model, the transverse intensity profiles $I_t(x, y) = |\mathbf{e}(x, y)|^2$ of guided modes characterized by their propagation constants β and angular frequencies ω were obtained. It was found, that analysed waveguide support approximately 10 modes at fundamental wavelength 800 nm and more than 40 modes at second-harmonics, i.e. 400nm. The first few modes for both, fundamental as well as for second harmonics for both the TE and TM polarizations are displayed in the figure 2.3.

Once having full set of guided modes at both the fundamental as well as at the second-harmonic frequency, the overall second-harmonic spectra consisting of individual spectral lines can be calculated. For the calculations, the spatial overlap of interacting modes together with their propagation constants with respect to the poling period has to be considered. The resulting spectral profile is depicted in the figure 2.4. Note, that sufficiently broad pump spectrum together with uniform excitation of fundamental spatial modes is necessary in order to observe the whole presented spectral profile.

2.2.2 Fabrication Imperfections

In any waveguide produced with a real fabrication technique, the fabrication imperfection inevitably occur. Generally speaking, any parameter of the waveguide, which is manipulated during the construction can be affected by the imperfections of the process. The parameters suffering the most are namely the dimensions of the waveguide and the poling properties. Since, as was shown, the modal structure, and therefore the phase-matching conditions depend strongly on these parameters, any variations of them will significantly affect the final

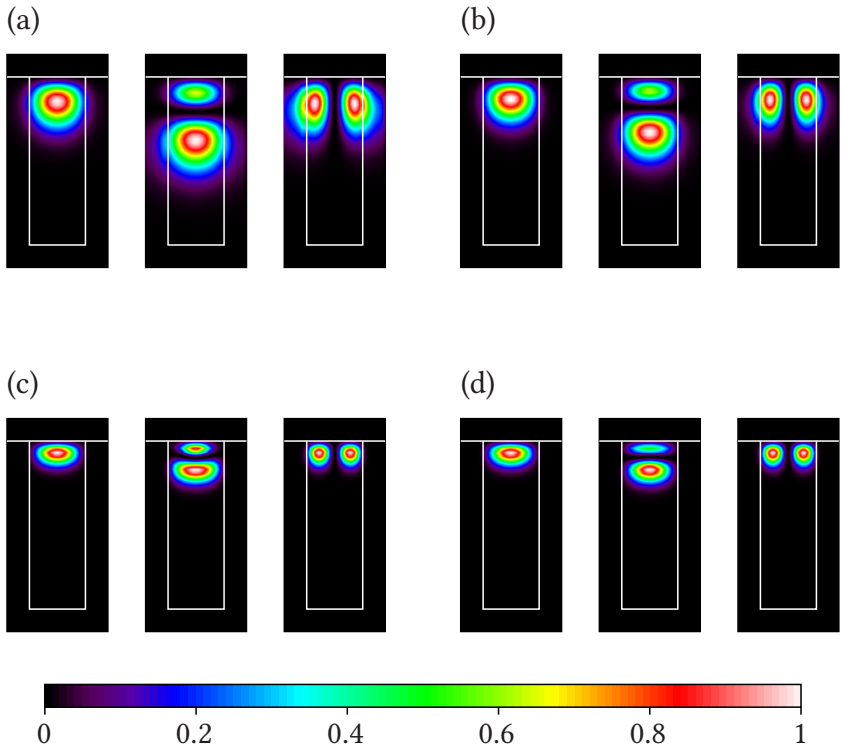

Figure 2.3: Topo graphs of calculated intensity distributions of TE- and TM-polarized fundamental as well as second-harmonic fields in the transverse plane of the waveguide for the first three spatial modes denoted as (0,0), (0,1), and (1,0). (a) TE @ 800 nm: $I_t(x,y) = |e(x,y,\omega_p)|^2$. (b) TM @ 800 nm: $I_t(x,y) = |h(x,y,\omega_p)|^2$. (c) TE @ 400 nm: $I_t(x,y) = |e(x,y,\omega_s)|^2$. (d) TM @ 400 nm: $I_t(x,y) = |h(x,y,\omega_s)|^2$. The white frames indicate the borders of the waveguide with dimension $5\times15\,\mu m^2$, while the upper horizontal lines represent the boundary between the chip and the air. Note, that the value 15 µm characterizes the depth of the waveguide given by error function (2.7) with the parameter $h = 10\,\mu m$.

spectral profile of generated fields. Because the influence of these modifications on generated fields is experimentally observable, it was necessary to adopt these variations also into our numerical model.

The tolerances of fabrication process were obtained directly from the manufacturer and are summarized in table 2.2. Based on the numerical model, these fluctuations will result in broadening of the second-harmonic spectra. In order to judge the amount of the spectral broadening, the dependence of second-harmonic peak spectral shift $\delta\lambda_s$ on each particular variation was calculated (see plots in the figure 2.5). Calculating spectral profile of generated field using values of tolerances given by the manufacturer, spectral broadening of individual peaks corresponding to particular process was obtained. Values of this broadening caused

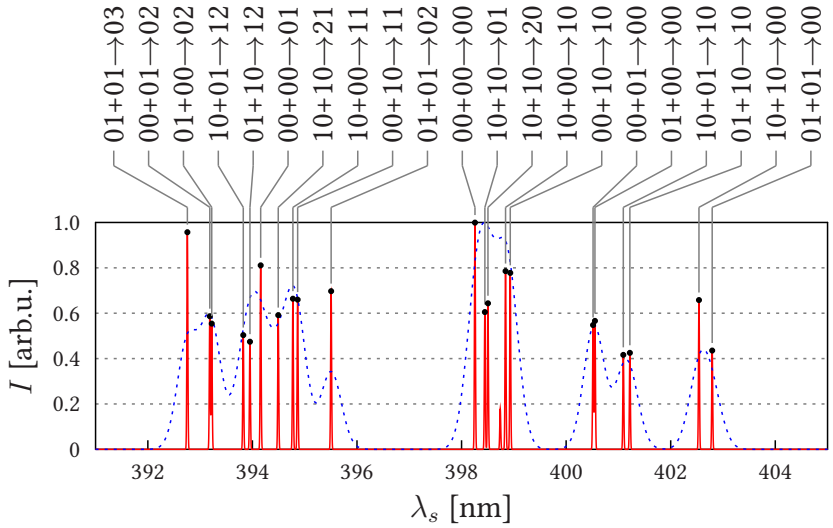

Figure 2.4: Theoretical spectral intensity I of the second-harmonic containing individual spectral lines, which corresponds to individual processes. The solid red line represents ideal case, where the width of each line is given by the phase-matching conditions only. The dashed blue line on the other hand represents broadening caused by fabrication imperfections of a real structure (see text for more details).

Property	Variance	Spectral broadening
Width	$\pm$ 0.1 µm	0.05 nm
Height	$\pm$ 2.0 µm	0.10 nm
Λ_{PM}	$\pm$ 0.1 µm	2.00 nm
Duty Ratio	50 % to 75 %	

Table 2.2: Table of manufacturing tolerances specified by the manufacturer together with resulting spectral broadening expected from the numerical model.

by imperfections in the width, height, and poling period were 0.05 nm, 0.1 nm, and 2 nm, respectively. Fluctuations of the poling period thus represent the main source of observed spectral broadening of second-harmonic field. In the case of sufficiently broad pump spectrum, the differences in values of width w, height h, and poling period Λ_{PM} will lead to significant spectral drift of particular lines also causing their broadening, as can be seen from plots in the figure 2.6.

There are several other variants of broken symmetry of poling. Except the fluctuations itself caused by the imperfect lithographic masks, also the variation in duty ratio is present. The duty ratio here means the ratio between poled and unpoled layers in a single poling period. For the perfect poling the duty ratio 50 % is expected, however because

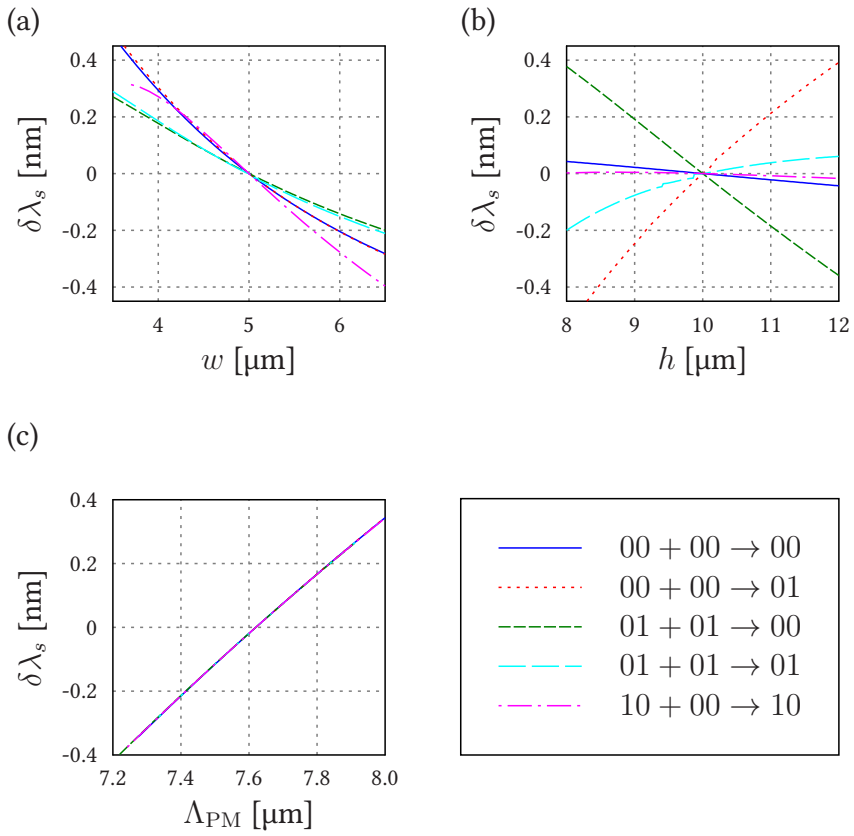

Figure 2.5: Spectral shift of second-harmonic peak $\delta\lambda_s$ as a function of the width w (a), depth h (b), and the poling period Λ_{PM} (c) of the waveguide for several selected combinations of interacting modes.

of the anisotropic penetration of the electrostatic field through the material during poling, the layers are formed in wedge shapes with slope depending on the material itself together with its thickness and the poling period. As can be shown for the case of perfectly symmetric poling with duty ratio 50 %, the dichotomic function representing the poling is also fully symmetrical and the Fourier series therefore contains only odd harmonics[37]. If however the poling is not perfectly symmetrical, then also even harmonics of the poling period will occur (see plots in the figure 2.7). Since the higher harmonics of the poling period can also be used for fulfilling the quasi-phase-matching (see equation (2.6)), the real duty ratio of the poling can be estimated observing ratio between processes phase-matched through the first and the second harmonic of poling. As will be shown later, the imperfection in the poling duty ratio is the reason for simultaneous coexistence of three different nonlinear processes in this structure (see section 2.3.2 on page 46).

The imperfect fabrication procedure causes not only the variations in the domain length, but because of inhomogeneous penetration of electrostatic field, some parts of the chip may not be poled at all. Moreover, there are several areas on the chip, which are not poled on pur-

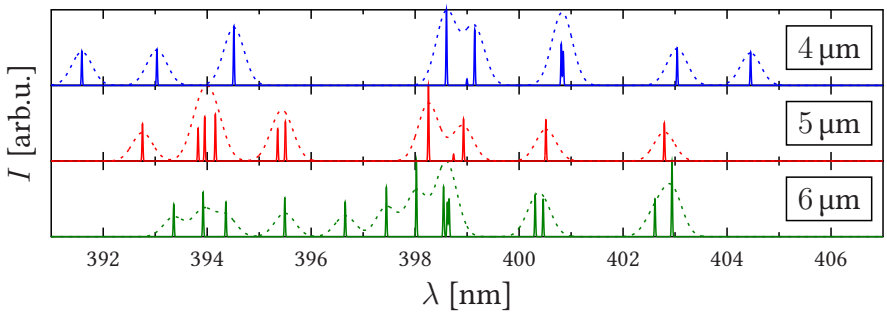

(a) Width

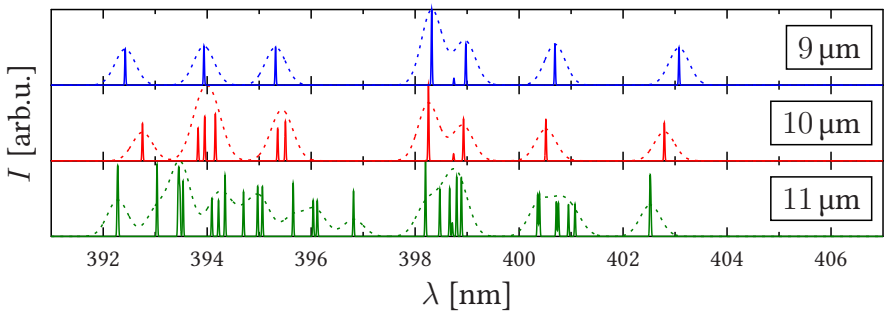

(b) Depth

Figure 2.6: Second-harmonic spectral intensity I calculated for three different values of width (a) and depth (b) of the waveguide. Solid lines correspond to ideal spectral broadening 0.13 nm given by phase-matching condition in 10.5 mm long waveguide including material and waveguide dispersion. Dashed lines then correspond to real spectral broadening expected due to the fabrication imperfections.

pose[38]. All this causes according to the simulations additional broadening of poling spectra (see again figure 2.7).

2.3 Experiment

In this section, a basic characterization of periodically-poled KTP waveguide will be introduced by means of experimental demonstration of second-harmonic generation.

2.3.1 Experimental Setup

The experimental realization of second-harmonic generation inside the periodically-poled KTP waveguide was performed using experimental setup sketched in the figure 2.8. As a laser

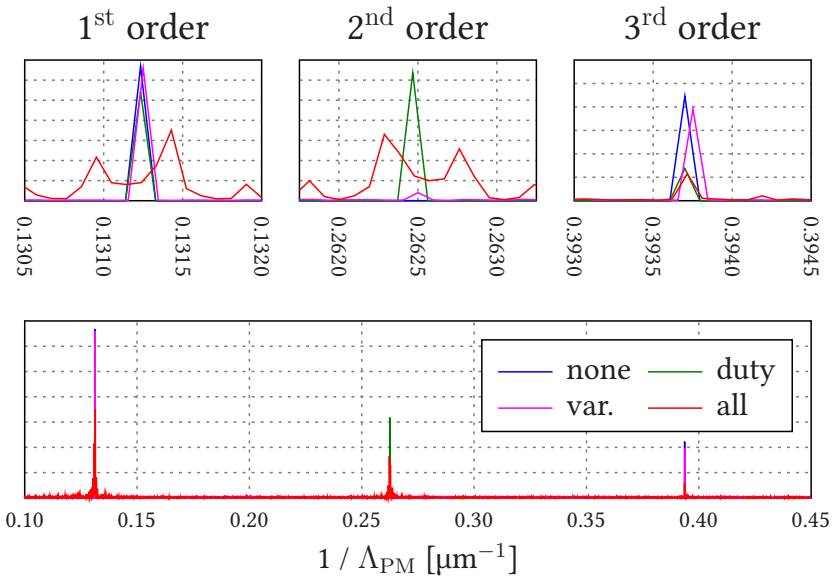

Figure 2.7: Fourier analysis of periodic poling. Three upper plots represent zoomed spectral areas containing the first-, second-, and the third-order of periodic modulation. Blue curve ('none') corresponds to perfect poling without second-order peak. Green curve ('duty') represents influence of non-symmetrical duty ratio resulting in presence of even-harmonics of periodic modulation. Impact of variation in domain lengths on poling spectra is shown using the magenta curve ('var.'). Finally, the red curve ('all') summaries all imperfections, and represents thus overall spectral profile of poling, that affects second-harmonic generation.

source, the mode-locked Ti:Sapphire oscillator Mira (Coherent) was used, producing pulses with duration about 100 fs at 87 MHz repetition rate with central wavelength 800 nm and spectral width 10 nm.

First, the laser beam was attenuated using combination of half-wave plate (HWP) and linear polarizer (LP) to about 20 mW. Also the central wavelength could be shifted by tilting the interference filter (F_I) with bandwidth 3 nm in the pump beam. The second half-wave plate was used to control the polarization of the pump. The position and spatial profile of prepared pump beam was monitored with the CCD camera, as they are the crucial parameters for ideal coupling of the pump beam into the waveguide.

Finally, the pump beam was coupled inside the waveguide using 10× microscope objective (Olympus). The KTP chip itself was placed on the Peltier element with the feedback loop allowing to thermally stabilize the structure, since the thermal drift also shifts the phase-matching condition about 1 nm per 25 °C (see figure 2.9a). Both the KTP chip and the microscope objectives were placed on precise XYZ linear stages with 20 nm resolution allowing for the precise positioning of the objectives with respect to both the beam and the waveguide (see figure 2.9b).

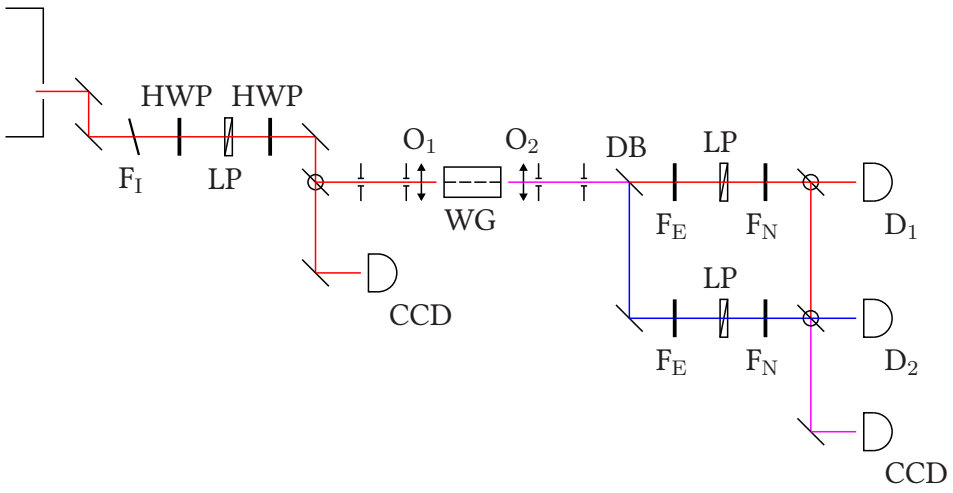

Figure 2.8: Sketch of the experimental setup for second-harmonic generation in periodically-poled KTP waveguide. F_I: interference filter, HWP: half-wave plate, LP: linear polarizer, O: microscope objective, CCD: CCD camera, WG: KTP waveguide, DB: dichroic beamsplitter, F_E: edge filter, F_N: neutral density filter, and D: detector.

Both, the residual pump together with the generated second-harmonic were decoupled and collimated using 20× objective with higher numerical aperture and separated using dichroic beamsplitter (DB). After passing through the linear polarizer (LP) and set of edge (F_E) and neutral density filters (F_N), the signal was analysed using the CCD camera, power meter, or the spectrometer. As for the spectrometer, the PC2000 (OceanOptics) with resolution 0.1 nm and Triax 320 (Jobin-Yvon) with resolution about 0.06 nm were used.

2.3.2 Individual Processes

Looking at the nonlinear coefficient matrix d_{ij} for chosen orientation of the KTP chip (see equation (1.21) in section 1.3.2 on page 10), three different processes can occur if appropriate phase-matching conditions are satisfied

$$P_y = 2d_{32}E_yE_z, \tag{2.12a}$$
$$P_z = d_{32}E_yE_y + d_{33}E_zE_z. \tag{2.12b}$$

The schematic illustration of these processes is depicted in the figure 2.10.

The first process described with equation (2.12a) represents Type II interaction, where both TE and TM polarization components of the pump are present, and where the second harmonic field is generated with TE polarization. The second equation (2.12b) represents combination of Type I and Type 0 processes, where Type I is generated by TE polarization, while Type 0 by TM polarization of fundamental field, and where both generate TM polarized second-harmonic field. As a consequence, with proper polarization manipulation

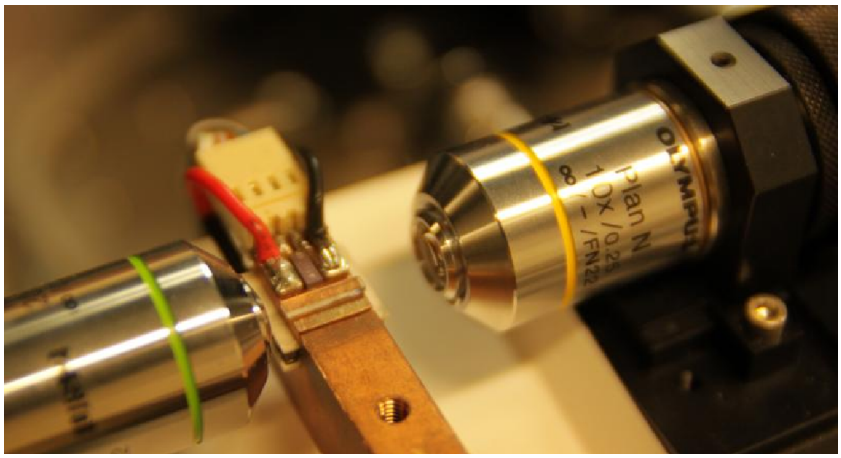

(a) Detail image of KTP waveguide sitting on a Peltier element, together with two coupling objectives.

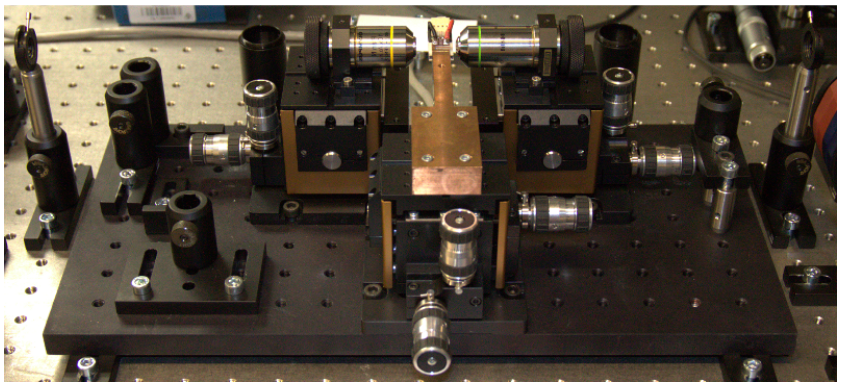

(b) Detail image of whole platform containing three precise linear XYZ stages for two coupling objectives and the element itself.

Figure 2.9: Detail images depicting mount of the nonlinear waveguide on the optical table.

of the pump field together with proper polarization projection of the signal field, any of these processes can be observed in such a material if appropriate phase-matching is satisfied. The final efficiency of the generation is then controlled via quasi-phase-matching, and therefore via poling period Λ_{PM} or through its higher harmonics.

The experimental evidence of presence of all three mentioned processes is clear from the graphs in the figure 2.11, where power oscillations of generated field depending on direction of linear polarization of the pump are depicted for two orthogonal orientations of linear polarizer after the waveguide. From these oscillations all three processes can be easily identified. The final summary is shown in table 2.3, where all relevant parameters are revealed. From this table it can be seen, that despite of utilizing the lower nonlinear coefficient, the most effective process is Type II process due to the most optimal poling period.

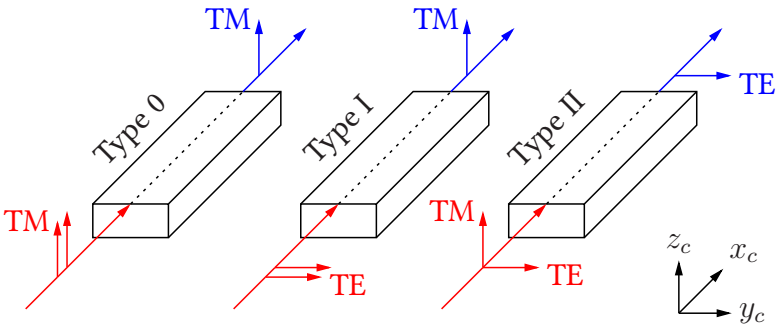

Figure 2.10: Schematic representation of three different nonlinear processes, which may occur in the waveguide if proper polarizations are involved and appropriate phase-matching conditions satisfied.

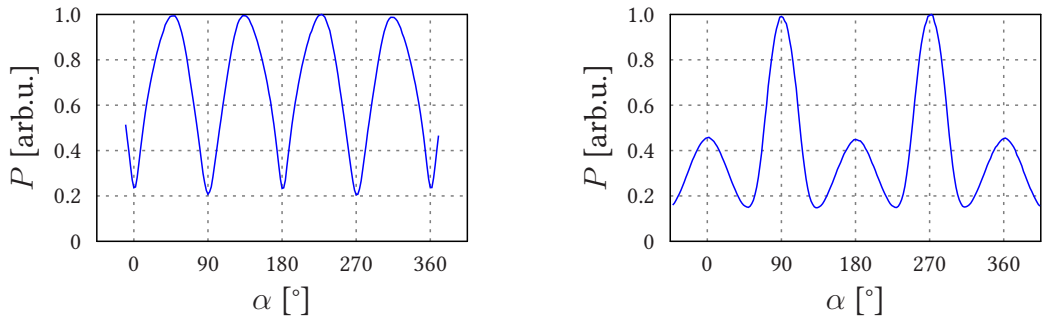

(a) TE (b) TM

Figure 2.11: The power of second-harmonic measured after passing through the linear polarizer transmitting TE (a) and TM (b) polarization as it depends on angle of polarization α, where $\alpha = 0°$ corresponds to the TE-polarization, while $\alpha = 90°$ corresponds to the TM-polarization.

Process		$\Lambda_{PM}^{(opt.)}$ [μm]	d_{eff} [pmV^{-1}]	η [W^{-1} cm^{-2}]
Type 0	TM + TM → TM	3.08	d_{33} = 10.7	2.83 ± 0.06
Type I	TE + TE → TM	1.83	d_{32} = 2.65	4.44 ± 0.12
Type II	TE + TM → TE	7.80	d_{32} = 2.65	4.78 ± 0.03

Table 2.3: Summary of processes of different types together with their optimal poling periods $\Lambda_{PM}^{(opt.)}$, effective nonlinear coefficients d_{eff}[1], and experimental conversion efficiencies η calculated according to formula $\eta = P_{SHG} P_{in}^{-1} L^{-2}$, where P_{SHG} (P_{in}) represents power of outgoing SH (coupled incident pump) and L is the length of the waveguide[25].

In the next section, the further analysis will be therefore concentrated on this process only. This process is also interesting from the point of view of the reversed process of parametric down-conversion. In this case two photons with orthogonal polarizations are generated and can be thus separated using polarizing beamsplitter.

2.4 Properties of Second-Harmonic Field Generated in Type II Process

The modal structure of the waveguide was found in a good agreement with the numerical analysis. The waveguide at fundamental frequency supports three different spatial modes for TE and five modes for TM polarization. As expected, the number of supported modes at second harmonic is much higher due to the fact, that the effective dimensions of the waveguide (i.e. the ratio between waveguide dimensions and wavelength) are doubled. The first three spatial modes for both TE- and TM-polarized fundamental as well as for the second-harmonic field are depicted in the figure 2.12. The selection of typical experimentally observed processes are depicted in the figure 2.13. As can be seen, the spatial profiles differ from these obtained from the numerical analysis (see figure 2.3), especially due to the imperfections in waveguide fabrication and non-ideal coupling of the fundamental mode.

As can be seen from figure 2.4, if the pump spectrum is wide enough or more fundamental modes are excited simultaneously, more individual nonlinear processes can be generated in the same time, resulting in broad second-harmonic spectra and modal structure. Since the spectra belonging to individual processes are relatively close to each other, but also wide overall, only spectral filtering is not sufficient to distinguish and separate them. Nevertheless, after spectral filtering, when only several individual processes are observed, a spatial filtering can be use in order to isolate only one particular nonlinear process.

By spatial filtering, the excitation of only specific fundamental modes is meant. It can be shown[17], that for the rectangular waveguide illuminated with plane wave, the higher order modes can be excited simply by tilting the incident wave. For chosen experimental configuration, tilting the incident beam would be however rather difficult, so the proper excitation of desired spatial modes was technically accomplish by misaligning the waveguide with respect to both the coupling objective and the pump beam, while monitoring the spatial profile of coupled mode on the CCD camera. Even though this technique leads to excitation of proper spatial mode, it also reduces the coupling efficiency, especially for higher modes. The overall coupling efficiency, additionally affected also by poor quality of the waveguide, was in the case of a single mode excitation only about 20 %.

Combining the spectral filtering of generated second harmonic field and careful alignment of the pump beam together with selecting only small part of pumping spectrum by tilting the interference filter, several spectral lines from expected spectra were observed. Their central wavelengths λ_s, spectral widths $\Delta\lambda_s$, as well as the relative powers P are summarized in table 2.4, where the comparison with the theoretical model is also presented. The differences between the theoretical data and the experimental results can be explained by the difficulties in reaching the efficient coupling of the pump mode.

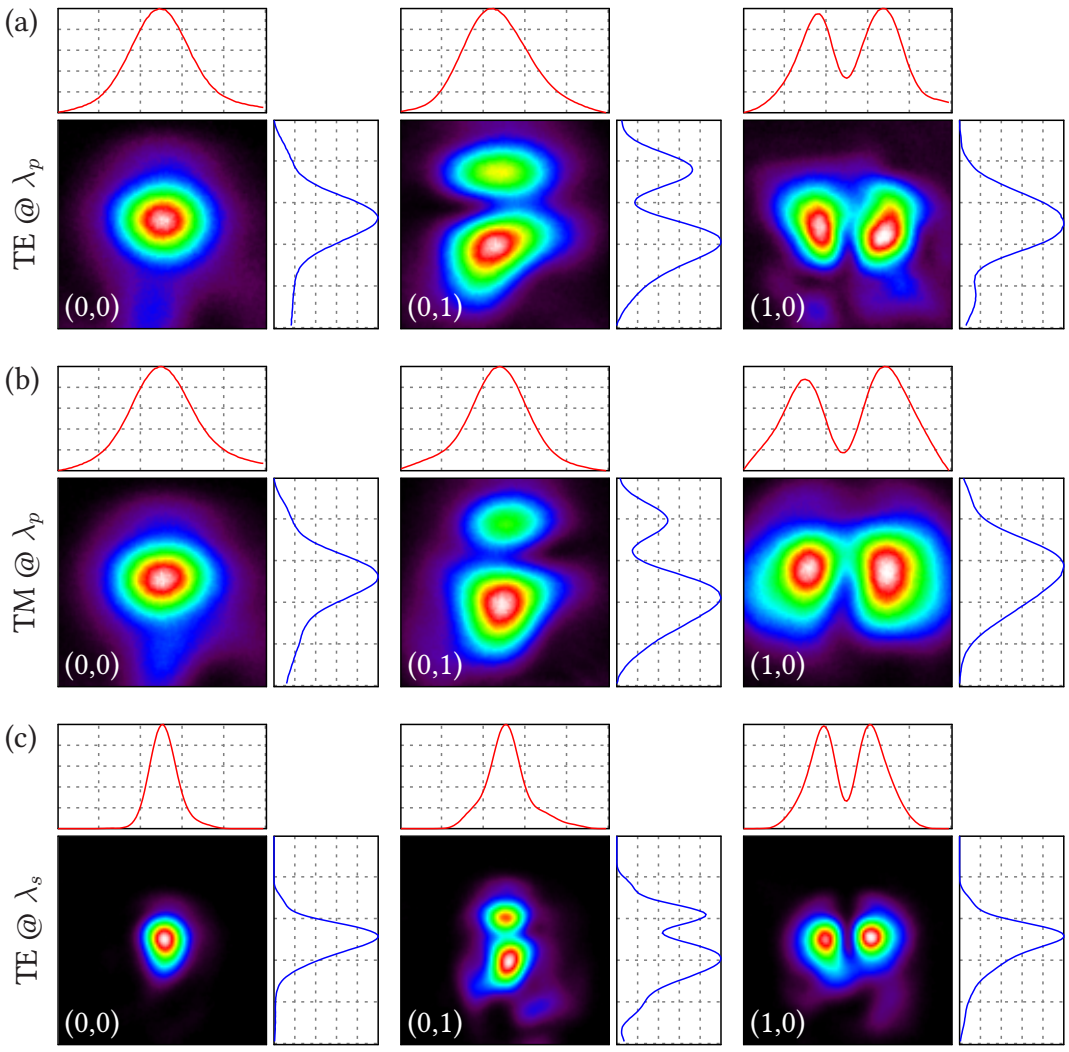

Figure 2.12: Measured topo graphs of spatial intensity profile $I_t(x, y)$ in transverse plane of the waveguide for the first three modes (0,0), (0,1), and (1,0) for (a) TE- and (b) TM-polarized pump and (c) TE-polarized second-harmonic field. The red and blue lines represent the intensity profile along the horizontal and vertical direction, respectively.

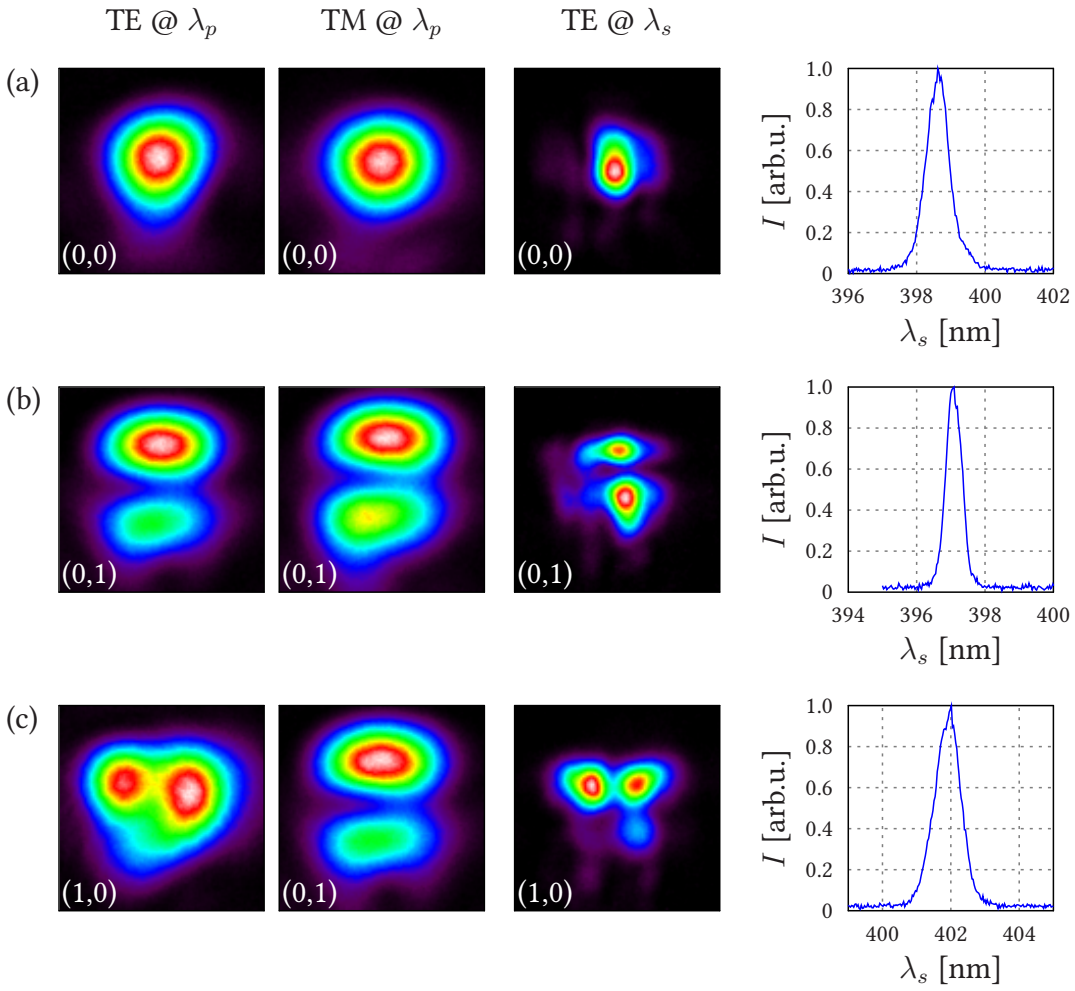

Figure 2.13: Measured topo graphs of spatial intensity profile $I_t(x, y)$ in transverse plane of the waveguide of TE- and TM-polarized pump and TE-polarized second-harmonic together with experimental spectral profiles of generated second-harmonic field for three different combination of interacting spatial modes. (a): (0,0) + (0,0) $\rightarrow$ (0,0), (b): (0,1) + (0,1) $\rightarrow$ (0,1), and (c): (1,0) + (0,1) $\rightarrow$ (1,0).

Modes (TE + TM → TE)	λ_s^{exp} [nm]	λ_s^{thr} [nm]	$\Delta\lambda_s^{exp}$ [nm]	P^{exp} [arb.u.]	P^{thr} [arb.u.]
00 + 00 → 00	398.3	398.6	0.8	1.00	1.00
00 + 00 → 01	394.2	394.4	0.9	0.65	0.81
10 + 00 → 10	398.8	399.5	0.6	0.42	0.78
01 + 01 → 00	402.8	403.0	0.8	0.38	0.43
10 + 01 → 10	401.1	401.9	0.9	0.35	0.42
01 + 01 → 01	398.7	397.1	0.6	0.32	0.18

Table 2.4: Individual processes of second-harmonic generation identified in the waveguide. Experimentally measured central wavelengths λ_s^{exp}, spectral widths $\Delta\lambda_s^{exp}$, and relative power P^{exp} are presented together with central wavelengths λ_s^{thr} and relative power P^{thr} obtained from the numerical model.

These results however documents the capability of controlling spatial and spectral properties of generated second-harmonic field. Moreover, if the analysed waveguide would be used in opposite process of parametric down-conversion, the signal and idler fields will be composed of contributions from different spatial modes, for instance $(0,0) \rightarrow (1,0) + (1,0)$ and $(0,0) \rightarrow (0,1) + (0,1)$. Therefore, by generating photon pairs using two different processes, photon pairs in modal spatial profile superposition state could be generated. This allows to generate entanglement of the two photon state in their spatial profile degree of freedom[39].

2.5 Summary

In this particular research activity, the experimental characterization of second-harmonic generation in periodically-poled KTP waveguide was addressed. In order to interpret the experimental data, numerical model based on the finite-elements method was developed. It was theoretically predicted and experimentally demonstrated, that three different types of nonlinear interaction, Type 0, Type I, and Type II can be generated simultaneously utilizing different orders of periodic modulation of the nonlinearity.

It was also shown, that due to the broad spatial and spectral structure of the fundamental mode, the second-harmonic field is generated also in spectrally wide range with rich modal structure. After that, the possibility of selecting only one particular interaction using spatial and spectral filtering of the pump together with spectral filtering of the second-harmonic field was presented. Finally, the experimental results were compared and found in a very good agreement with developed theoretical model.

Further to that, the imperfection during the fabrication was considered and adopted into the numerical model. The analysed waveguide was proven to be a versatile device for second-harmonic generation and it can be also promising source for generation of entangled photon pairs in process of spontaneous parametric down-conversion.

3

Quantum Entanglement

Quantum entanglement is phenomenon describing a very specific type of correlations. These mean, that two or more particles can not be described independently by their individual quantum states, but a single quantum state for whole physical system has to be used instead. Even though the therm entanglement mostly describes correlation in a single physical property of set of different particles, this type of correlation can exists also between different degrees of freedom (i.e. physical properties) of a single particle.

In this chapter, basic experimental tools for determination and characterization of nonclassical quantum states will be presented. This study was performed by the author at the University of Insubria in Como, Italy and published in paper by Sciarrino *et al.* [40].

3.1 Introduction

Quantum entangled states has become useful not only for testing fundamentals laws of quantum mechanics, but also for their practical value in many real applications. For instance in quantum optics the entangled states can be used for quantum computing[41,42], quantum communications[41,43,44], quantum metrology[45], or ghost imaging[46,47].

For most of these applications, high quality of entangled states is required. Photonic entanglement itself can be in principle carried by any property that characterizes light (polarization, orbital angular momentum, frequency, or momentum), or even by a combination of them[48]. However, the polarization entanglement is the most popular one due to availability of optical elements manipulating the polarization states and also due to the simplicity of its generation.

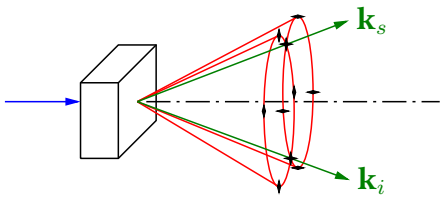

Figure 3.1: Source of entangled photon pairs based on Type II nonlinear interaction. Black arrows indicates direction of polarization[49]. Propagation directions of signal and idler photons forming entanglement in polarization are depicted using green lines.

3.2 Theory

In this section, the theoretical background covering quantum entanglement will be presented. Also Bell's inequalities and quantum tomography technique as a tool to experimentally characterize given quantum state will be mentioned.

3.2.1 Source of Entangled Photon Pairs

In order to demonstrate the effect of quantum correlations, the source of entangled photon pairs based on spontaneous parametric down-conversion (SPDC) will be used.

This source is schematically illustrated in the figure 3.1. In process of SPDC, single fundamental photons split into a photon pairs in the nonlinear crystal with second-order nonlinearity $\chi^{(2)}$. Due to 3D geometry, the phase-matching condition can be fulfilled for numberless combinations of directions (see figure 1.5b on page 14). As a consequence, the photons are emitted in a cone shape and are spatially correlated in such a way, that two photons from one pair lie on the opposite side of the cone with respect to the cone axis.

In the case of Type II interaction, where generated photons have orthogonal polarizations, the cones for each polarization are spatially displaced due to the birefringence of the nonlinear material*. For historical reason, photons emitted in these directions and originating from one pair are called *signal* and *idler*. As can be seen from figure 3.1, the cones overlap in two directions, where photons from both cones can be detected. Generated state is in these directions due to this overlap in coherent superposition of both contributions and can be described with following quantum state

$$|\psi\rangle = \frac{1}{\sqrt{2}} \left(|H\rangle_s |V\rangle_i + |V\rangle_s |H\rangle_i \right) . \tag{3.1}$$

*Anisotropic material is assumed to fulfil phase-matching condition.

3.2.2 EPR Paradox and Bell's Inequalities

In the 1935 A. Einstein, B. Podolsky, and N. Rosen (EPR) published their famous paper, where thought experiment similar to following was presented[50]. Let the entangled photons from source mentioned in the previous paragraph propagate through the space. Each of them has the same probability to have H or V polarization. If however the polarization state of one of them is measured, the polarization state of the second one is know in that very moment (the wave function describing the quantum state collapses). This happens even though the state was random an instant ago, no matter how far it is from the first one.

Einstein and the others considered this behaviour impossible since it violates the local realism stating, that all physical quantities have to have a pre-existing value for any possible measurement before the measurement is done, and that an object is influenced directly only by its surroundings, and therefore no action on one system can change the physical reality of spatially separated object. The authors therefore concluded, that the description of quantum state with a single wave function can not be complete, and thus some hidden variables must exist in order to determine results of all possible experiments in advance.

As an answer to the EPR paradox, 30 years later physicist J.S. Bell demonstrated, that no physical theory of local hidden variables can ever reproduce all of the predictions of quantum mechanics, that are consistent with experimental results[51]. He also introduced a set of inequalities, which may be measured experimentally, and whose violation contradicts the validity of local realism or any local hidden variables model. As a consequence, if any physical system is found to violate these inequalities, it has to be described using quantum mechanical apparatus and can not be described classically. The Bell's inequalities can therefore serve to distinguish, whether the system is 'classical' or 'quantum'.

3.2.3 CHSH Inequality

The Bell's inequalities can be used directly to prove, whether the hidden variables model is valid for given system or not and as a consequence, whether the system is in classical or a quantum state. The experiment however requires statistical analysis of a large number of measurements of an entangled system. From experimental point of view it is much more convenient to use another, Clauser-Horne-Shimony-Holt (CHSH) inequality, which also provides the information about non-classicality of given system[52].

In order to obtain the CHSH inequality, let there be an operator S defined as

$$S = E(a, b) - E(a, b') + E(a', b) + E(a', b'), \tag{3.2}$$

where a, a' and b, b' represent settings on two detectors (observable) and $E(i, j)$ experimentally obtained correlations for corresponding settings. For sake of this analysis, two-particle system will be assumed. It can be shown[52,53], that for any classical system or any system, which can be described by a local hidden variables model, the quantity S from equation (3.2) has to satisfy following inequality

$$|\langle S \rangle_{\mathrm{LHV}}| \leq 2. \tag{3.3}$$

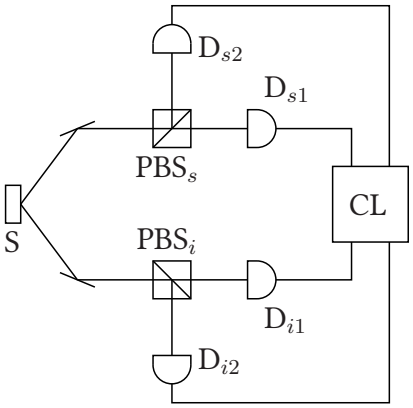

Figure 3.2: Schematic illustration of two channel Bell test. Each photon from single photon pair produced by source (S) is sent into one channel consisting of polarizing beamsplitter (PBS) and two detectors (D_1) and (D_2). During experiment, the beamsplitter PBS can be rotated by angle θ. In the experiment transmitted and reflected photons are detected with detectors D with overall coincidence rates registered by coincidence logic (CL).

Equation (3.3) is the expected Clauser-Horne-Shomony-Holt inequality, which if violated proves, that the system is in quantum state and can not be described classically.

It should be noted, that no all quantum states violate inequality (3.3). It is therefore necessary, however not sufficient condition for the CHSH inequality violation. In order for this inequality to be violated, the projections of quantum state (i.e. the settings a, a' and b, b') has to be set properly. Moreover, also the amount of the CHSH inequality violation depends on these settings.

In order to illustrate violation of CHSH inequality, two channel Bell test of an entangled state $|\psi\rangle$ from equation (3.1) produced by presented source based on SPDC will be demonstrated. For this demonstration, the scheme depicted in the figure 3.2 will be considered. Since the entanglement is encoded into the polarization degree of freedom, polarization projection measurements will be performed. In order to obtain quantity S, four different projection measurements will be done and four correlation functions $E(i, j)$ from equation (3.2) will be calculated from a coincidence measurements $C(\theta_i, \theta_j)$ as

$$E(\theta_i, \theta_j) = \frac{C(\theta_i, \theta_j) + C(\theta_i^\perp, \theta_j^\perp) - C(\theta_i^\perp, \theta_j) - C(\theta_i, \theta_j^\perp)}{C(\theta_i, \theta_j) + C(\theta_i^\perp, \theta_j^\perp) + C(\theta_i^\perp, \theta_j) + C(\theta_i, \theta_j^\perp)}, \tag{3.4}$$

where $C(\theta_i, \theta_j)$ represents the coincidence rates if signal and idler are projected into angles θ_i and θ_j, respectively and where angle θ denotes projection angle in $\{H, V\}$ basis. $\theta = 0°$ represents horizontal, while $\theta = 45°$ diagonal polarization. Symbol $\theta^\perp$ then represents orthogonal output of polarizer with respect to setting θ.

In the end, four coincidence measurements for four correlation functions, therefore sixteen measurements overall, has to be performed. As can be shown[54], the maximal violation is

obtained for following settings: $\theta_a = 0°$, $\theta_{a'} = 45°$, $\theta_b = 22.5°$, and $\theta_{b'} = -22.5°$. Since in this basis the greatest violation is observed, these angles are sometimes called Bell test angles. As can be shown, this two photon Bell test of quantum state $|\psi\rangle$ from equation (3.1) will result in $|\langle S\rangle| = 2\sqrt{2} \simeq 2.828 > 2$, which violates the CHSH inequality with the highest possible value.

3.2.4 Quantum State Tomography

For practical applications, which are taking advantages of quantum nature of entangled systems, it is usually necessary to build a source of some particular quantum state. In real experiments the entanglement also degrades by decoherence and dissipation processes resulting from unavoidable coupling with the environment[55]. For these reasons the ability to characterize the input state is important. Even though the Bell's inequalities can be used to distinguish, whether the state is entangled or not, in real experiments this is usually not sufficient information.

In order to fully characterize any general quantum state, the density matrix represented by linear density operator

$$\hat{\rho} = \sum_i p_i |\psi_i\rangle\langle\psi_i| \tag{3.5}$$

has to be determined. Here, set of states $|\psi_i\rangle$ represents any arbitrary basis and p_i are probabilities, that investigated system is in corresponding state $|\psi_i\rangle$. Since the density matrix is rather complex and describe studied system completely, different quantities like purity or fidelity can be derived in order to characterize some specific property of given quantum state.

Density matrix $\hat{\rho}$ can be reconstructed by measuring a complete set of observables. This technique is called quantum state tomography and it is a fundamental tool to explore the properties of particular quantum state[56].

Quantum Tomography of Two-Qubit State

Technique of quantum state tomography is based on Born's statistical rule, which determine probability, that a measurement E_i performed on quantum system will give particular result

$$P(E_i|\hat{\rho}) = Tr(E_i\hat{\rho}). \tag{3.6}$$

Having a statistical set of the same measurement E_i, quantity $P(E_i|\hat{\rho})$ can be substituted by this histogram. The density matrix can be therefore obtained by linear inversion according to following schematic notation

$$E_i\hat{\rho} = p_i \tag{3.7}$$

$$\hat{\rho} = E_i^{-1}p_i. \tag{3.8}$$

This can be however performed only when the measurements E_i are tomographically complete, i.e. corresponding operators form a basis in equivalent Hilbert space.

In case of generally mixed two qubit state, sixteen linearly independent measurements overall (four measurements for each qubit) are necessary to determine the density matrix $\hat{\rho}$. Although this number of measurements is sufficient, the complete set of measurements consists of six different projections per qubit, and therefore 36 measurements overall[57]. In this case of over-complete polarization tomography, the density matrix is over-determined, which can afterwards improve the accuracy of the experiment and provide a better sensing of the quantum state.

Maximum Likelihood Estimation

Using linear inversion as described above has however one great drawback. The density matrix $\hat{\rho}$ is by the definition positive definite, Hermitian, and with a unit trace. Nevertheless, due to an experimental imperfections, a negative eigenvalues (i.e. probabilities) can be obtained, for instance, which obviously represents a non-physical solution.

As an answer to this issue a Maximum Likelihood Estimation (MLE) can be used. It is a method, that estimates the parameters of given statistical model when applied to experimental data. In this case, the MLE method finds a physical density matrix, which most-likely produces the measured data by maximizing the likelihood (i.e. the probability) of the obtained density matrix to correspond to the experimental data. Practical implementation of such a method is therefore based on some iterative techniques[58].

3.3 Experiment

In this section, experimental generation and characterization of entangled quantum states will be presented. Investigated states were generated using continuous wave (CW) laser at 266 nm with long coherence time, pumping a Kwiat's source based on two Type I crystals. Even though the preparation of polarization entangled state was in this spectral region already demonstrated using femtosecond pumping[59], with CW pumping the standard Type II phase-matching[60] is difficult to adopt due to several dispersion effects of nonlinear crystals[61].

In this configuration, the full set of so-called Bell's states with polarization entanglement was generated. These states are defined as a maximally entangled quantum states of two qubits. Assuming the most simple examples of two-photon qubits, following set of Bell's states is typically introduced

$$|\Phi^+\rangle = \frac{1}{\sqrt{2}}(|H\rangle|H\rangle + |V\rangle|V\rangle), \tag{3.9a}$$

$$|\Phi^-\rangle = \frac{1}{\sqrt{2}}(|H\rangle|H\rangle - |V\rangle|V\rangle), \tag{3.9b}$$

$$|\Psi^+\rangle = \frac{1}{\sqrt{2}}(|H\rangle|V\rangle + |V\rangle|H\rangle), \tag{3.9c}$$

$$|\Psi^-\rangle = \frac{1}{\sqrt{2}}(|H\rangle|V\rangle - |V\rangle|H\rangle), \tag{3.9d}$$

where H and V correspond to the horizontal and vertical polarizations, respectively.

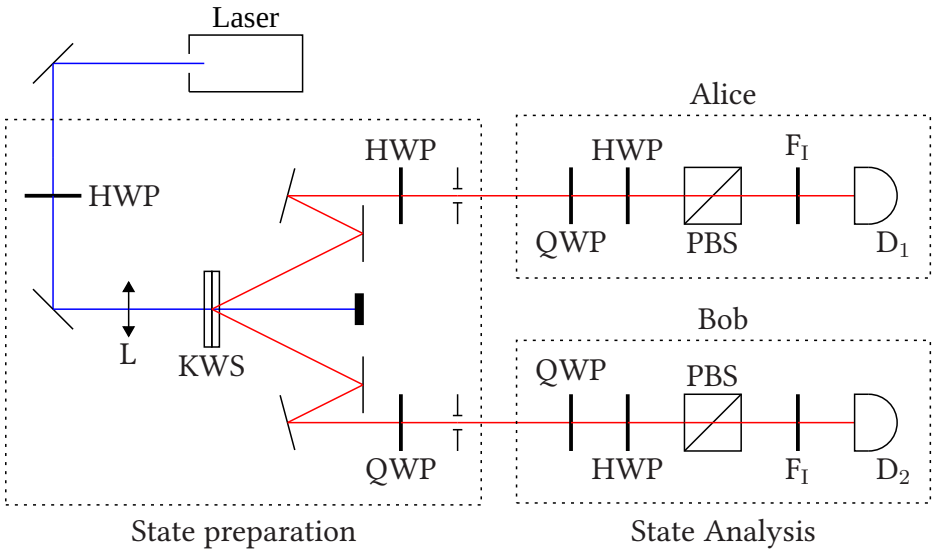

Figure 3.3: Sketch of experimental setup used for generating full set of Bell's states and for their future analysis through a standard quantum tomography technique and non-locality test. HWP: half-wave plate, L: positive lens, KWS: Kwiat's source, QWP: quarter-wave plate, PBS: polarizing beamsplitter, F_I: interference filter, and D: detector.

3.3.1 Experimental Setup

Experimental setup depicted in the figure 3.3 consisted of three different parts: the laser source, state preparation, and state detection part. The two symmetrical detection parts operating on signal and idler photons will be for the future reference called *Alice's* and *Bob's* detection blocks, respectively, as it is typical in quantum information processing experiments.

As the source, the MBD-266 (Coherent) doubling unit pumped by Verdi V-2 (Coherent) laser was used. This unit emitting in UV region at 266 nm produced vertically polarized light with typical power about 150 mW and coherence time nearly 0.2 µs.

The most simple source of polarization entangled photon pairs would be a single Type II nonlinear crystal. Here however more sophisticated source based on Kwiat's design[62] was used for its versatility.

3.3.2 Kwiat's Source

Kwiat's source is composed of two thin nonlinear crystals of Type I with orthogonally oriented optical axes as it is shown in the figure 3.4. As a result, when it is pumped by vertical (horizontal) polarization, only the first (second) crystal generates one single SPDC cone with polarization orthogonal to the pump. If the crystals are however pumped by diagonal

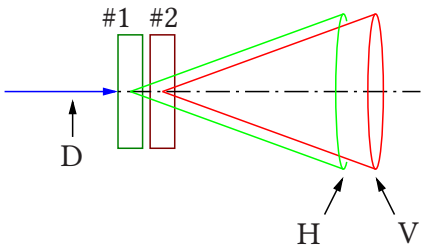

Figure 3.4: Schematic illustration of Kwiat's source based on two identical Type I nonlinear crystals with perpendicular optical axes. The crystals are oriented in such a way, that their optical axes together with the pump beam define the vertical and horizontal plane, respectively. Labels D, H, and V represent diagonal, horizontal, and vertical polarizations, respectively.

	$\|\Phi^+\rangle$	$\|\Phi^-\rangle$	$\|\Psi^+\rangle$	$\|\Psi^-\rangle$
δ	0°	0°	0°	0°
γ	45°	−45°	45°	−45°
HWP	out	out	in	in

Table 3.1: Kwiat's source settings for generating particular Bell's state. Parameters δ and γ corresponds to these from equation (3.10).

polarization, both crystals will generate with the same probability orthogonally polarized and spatially overlapped cones. Important point is, that as long as the emitted spatial modes are indistinguishable (the crystals are thin enough with respect to the coherence length of the pump and to the collecting aperture), these particular processes are coherent. As a result, the photons are created in state

$$|\phi\rangle = \cos\gamma|HH\rangle + \sin\gamma e^{i\delta}|VV\rangle, \tag{3.10}$$

where angle γ represents direction of polarization of the pump and additional phase factor δ is determined by the phase-matching together with the thickness of the crystals and can be adjusted by controlling relative phase shift between orthogonally polarized components.

From a general state described by formula (3.10) and produced by a Kwiat's source, the full set of Bell's states can be obtained by tailoring parameters γ and δ according to table 3.1, where 'HWP in' means inserting an additional half-wave plate into one arm in order to swap H and V polarizations.

In this particular case the BBO crystals with length 0.5 mm were used, while two portions of generated cones were spatially selected symmetrically with respect to the cone axis using two irises in order to obtain spectrally degenerate photon pairs ($\omega_s = \omega_i$).

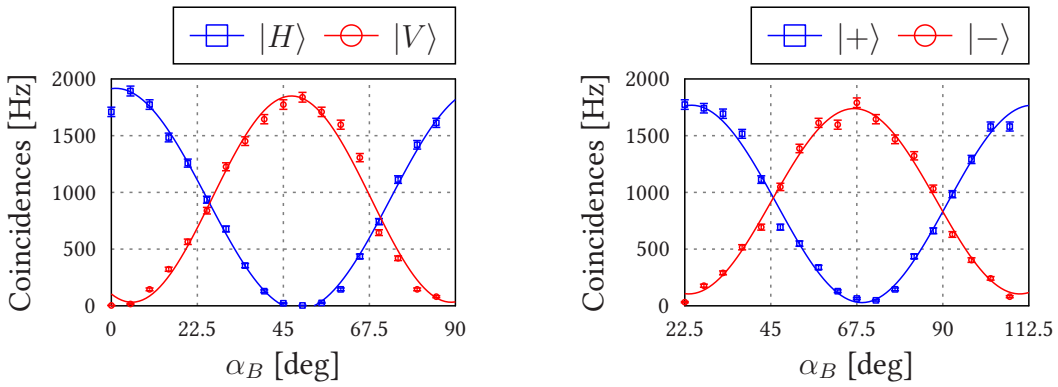

(a) HV base

(b) PM base

Figure 3.5: Coincidence fringe patterns measured with fixed half-wave plate orientation for Alice ($|H\rangle$, $|V\rangle$, $|+\rangle$, and $|-\rangle$), while rotating Bob's wave plate. The measurements lasted 10 s for each point and accidental coincidences were subtracted. Error bars were estimated assuming Poisson distribution of coincidence counts.

3.3.3 Source Optimization

In order to obtain maximally bright source, the pump beam was focused using lens with focal distance 50 cm so the beam waist lied in the plane together with the irises[63]. Next, the source was adjusted to generate state $|\Phi^+\rangle$. Now if the signal photon is detected by Alice with horizontal polarization $|H\rangle$, while the coincidences with Bob are measured after projecting the idler photon into specific polarization state $|\psi\rangle = \cos\theta|H\rangle + \sin\theta|V\rangle$, the coincidence rate (i.e coincidence probability) as function of θ should be ideally characterized by formula $P(|H\rangle, |\psi\rangle) = \cos^2\theta$. Alternatively, if signal photon is by Alice detected with vertical polarization $|V\rangle$, with the same projection done by Bob, the coincidence probability should follow formula $P(|V\rangle, |\psi\rangle) = \sin^2\theta$. Both expressions derived for coincidence probabilities were experimentally verified by measuring the coincidence rate depending on half-wave plate rotation angle $\alpha = \theta/2$ on Bob's side, while keeping fixed the projection into $|H\rangle$ and $|V\rangle$ states on Alice's side, respectively. The outcome in form of coincidence fringes is depicted on plots in the figure 3.5a.

In order to quantify the results, the visibility of fringe pattern can be calculated as

$$V = \frac{C_{\max} - C_{\min}}{C_{\max} + C_{\min}}, \tag{3.11}$$

where $C_{\max}$ and $C_{\min}$ are the maximal and minimal coincidence rates, respectively. Experimentally obtained values $V = 1.00 \pm 0.01$ (for both cases) were found in a very good agreement with the theoretical prediction.

The coherence of contributions $|HH\rangle$ and $|VV\rangle$ can be determined in the same manner with the only difference, that the signal photons on Alice's side is projected into the di-

agonal $|+\rangle$ and anti-diagonal $|-\rangle$ states. As can be shown, since the diagonal and anti-diagonal states can be expressed as $|+\rangle = 1/\sqrt{2}(|H\rangle + |V\rangle)$ and $|+\rangle = 1/\sqrt{2}(|H\rangle - |V\rangle)$, respectively, the coincidence probability for diagonal and anti-diagonal projections with polarization state $|\psi\rangle = \cos\theta|H\rangle + \sin\theta|V\rangle$ is determined by formulas $P(|+\rangle, |\psi\rangle) = \cos^2\theta - \pi/4$ and $P(|-\rangle, |\psi\rangle) = \sin^2\theta - \pi/4$, respectively. On the other hand, if the contributions $|HH\rangle$ and $|VV\rangle$ are in incoherent superposition, the coincidence rates should be constant as $P(|+\rangle, |\psi\rangle) = P(|-\rangle, |\psi\rangle) = 1/2$, and the visibility will therefore be zero. For the experimental results see again figure 3.5b, where phase shift of $\pi/4$ between $P(|H\rangle, |\psi\rangle)$ $[P(|V\rangle, |\psi\rangle)]$ and $P(|+\rangle, |\psi\rangle)$ $[P(|-\rangle, |\psi\rangle)]$ can be seen. Also, the obtained visibilities $V = 0.95 \pm 0.01$ are in good agreement with the theoretical predictions.

All presented data were corrected by subtracting accidental coincidences. The rate of accidental coincidences was estimated using formula

$$N_{\text{acc}} = 2N_A N_B \tau, \tag{3.12}$$

where N_A and N_B are single rates of signal and idler, respectively and $\tau = 2.8$ ns is the coincidence window. Factor 2 represents the fact, that each channel can initiate the acquisition.

3.4 Results

This section will be devoted to main results gained from the experiment. Density matrices of generated states obtained by means of quantum tomography will be presented together with value the of CHSH operator.

3.4.1 Polarization Measurement

Polarization tomography is in general set of polarization projections into different bases. With apparatus used in detection part of the setup (see figure 3.3) consisting of quarter-wave plate (QWP), half-wave plate (HWP), and a polarizing beamsplitter (PBS), the projection of incident photon into three different linearly dependent bases $\{|H\rangle, |V\rangle\}$, $\{|+\rangle, |-\rangle\}$, and $\{|R\rangle, |L\rangle\}$, where $|R\rangle = 1/\sqrt{2}(|H\rangle - i|V\rangle)$ and $|L\rangle = 1/\sqrt{2}(|H\rangle + i|V\rangle)$ was possible. Table 3.2 contains settings for each wave plates in order for the particular projection $|\psi\rangle$ to be achieved, where meaning of angles α and β are graphically illustrated in the figure 3.6. The polarizing beamsplitter is oriented in such way, that the detector measures horizontal projection of manipulated state.

3.4.2 Quantum State Tomography

In this section, polarization quantum tomography of two-qubit state will be used in order to fully characterize prepared quantum states. Source manipulation leading to optimal generation will be also presented.

$\|\psi\rangle$	α	β
$\|H\rangle$	0°	0°
$\|V\rangle$	0°	45°
$\|+\rangle$	45°	22.5°
$\|-\rangle$	45°	−22.5°
$\|R\rangle$	0°	−22.5°
$\|L\rangle$	0°	22.5°

Table 3.2: List of settings for quarter- and half-wave plates resulting in projection into state $|\psi\rangle$. Angles α and β represent rotation of wave plates' axes and are schematically illustrated in the figure 3.6.

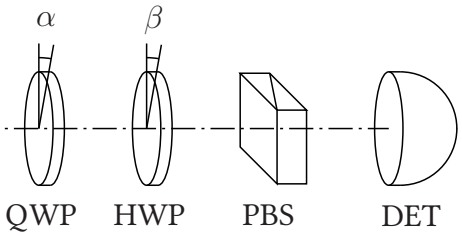

Figure 3.6: Schematic representation of single projector as an essential part for polarization tomography. QWP: quarter-wave plate, HWP: half-wave plate, PBS: polarizing beamsplitter, and DET: detector. α and β represent angle of rotation.

State Preparation

Without any optimization, the Kwiat's source generates general states $|\psi\rangle = \cos\gamma|HH\rangle + \sin\gamma e^{i\delta}|VV\rangle$. In order to obtain maximally entangled state, contributions from both crystals have to be balanced by pumping the crystals with polarization diagonal with respect to the crystals' axes. This was achieved by rotating the vertical polarization of laser beam with a half-wave plate placed in the pump in front of the Kwiat's source. Using this wave plate, switching between $|\Phi^+\rangle$ and $|\Phi^-\rangle$ was also possible by setting the pump polarization to be diagonal or anti-diagonal.

In order to set exponential factor $e^{i\delta}$ three different strategies can be adopted. In all cases, relative phase between horizontal and vertical component is controlled. The first way is to tilt the nonlinear crystals themselves. This would however change the phase-matching, and therefore the opening angle of output cones. Similar effect only without affecting the phase-matching can be achieved by tilting a quarter-wave plate in pump beam in front of the nonlinear crystals. The last option adopted here uses an additional quarter-wave plate placed in a signal path (therefore after the nonlinear crystals) with the main axes oriented in horizontal and vertical directions. In this case it does not change the polarization state, however by its tilting, the phase shift between H and V contributions can be introduced continuously, and the desired factor δ therefore adjusted as needed.

With this procedure, two Bell's states $|\Phi^+\rangle$ and $|\Phi^-\rangle$ can be generated. In order to generate the second two, additional half-wave plate rotated by 45° was used in idler arm to swap H and V polarizations. In the end, a full set of Bell's states as defined in equations (3.9a)–(3.9d) could be generated.

	$\|\Phi^+\rangle$	$\|\Phi^-\rangle$	$\|\Psi^+\rangle$	$\|\Psi^-\rangle$
P	0.951 ± 0.003	0.9700 ± 0.0008	0.968 ± 0.002	0.962 ± 0.002
F	0.947 ± 0.006	0.946 ± 0.002	0.955 ± 0.004	0.951 ± 0.005
C	0.946 ± 0.006	0.944 ± 0.002	0.955 ± 0.004	0.952 ± 0.005

Table 3.3: Measured values of purity (P), fidelity (F), and concurrence (C) for all prepared Bell's states. The errors were obtained from statistical analysis.

State Characterization

In order to fully characterize generated states, the density matrix was reconstructed from overcomplete quantum tomography measurement using maximum likelihood estimation[56]. For better understanding of the quality of generated quantum states, parameters purity, fidelity, and concurrence can be used.

Purity (P) is defined as a trace of density matrix square $P = \mathrm{Tr}\,[\rho^2]$. It can be proved, that for pure states $P = 1$, while for mixed states $0 \leq P < 1$. It should be mentioned, that all Bell's states are pure states.

Fidelity (F) characterizes the overlap of generated state with the target state. For pure target states, the fidelity can be calculated as $F = \langle\psi|\rho|\psi\rangle$, where ρ is density matrix of generated state and $|\psi\rangle$ is the target state. It can be also proved, that if fidelity with maximally entangled state is more than 1/2, the investigated state is also entangled.

Concurrence (C) can be used as a measure of entanglement, since it is increasing function of the amount of the entanglement[64]. It takes values from 0 to 1, as for $C = 0$ the state is fully separable, while for $C = 1$, the state if maximally entangled.

To estimate experimental errors, a statistical Monte Carlo method was used to simulate 50 random measurements with uncertainty given by the shot noise (as it can be considered as a dominant source of uncertainty for this measurements), thus following Poisson distribution. From these simulations, the experimental errors were calculated as a standard deviations of simulated quantities.

Reconstructed density matrices of prepared states are plotted in the figure 3.7. The values of their purity, fidelity (with corresponded Bell's state), and concurrence are then summarized in the table 3.3.

Under described experimental condition, full set of Bell's states with high average values of purity $P = 0.95$, fidelity $F = 0.96$, and concurrence $C = 0.95$ was successfully generated.

3.4.3 Entanglement Verification of Generated States

The motivation was to show, that quantum states violate Bell's inequalities. In order to do that, four Bell's states were prepared using Kwiat's source. To verify quality of generated

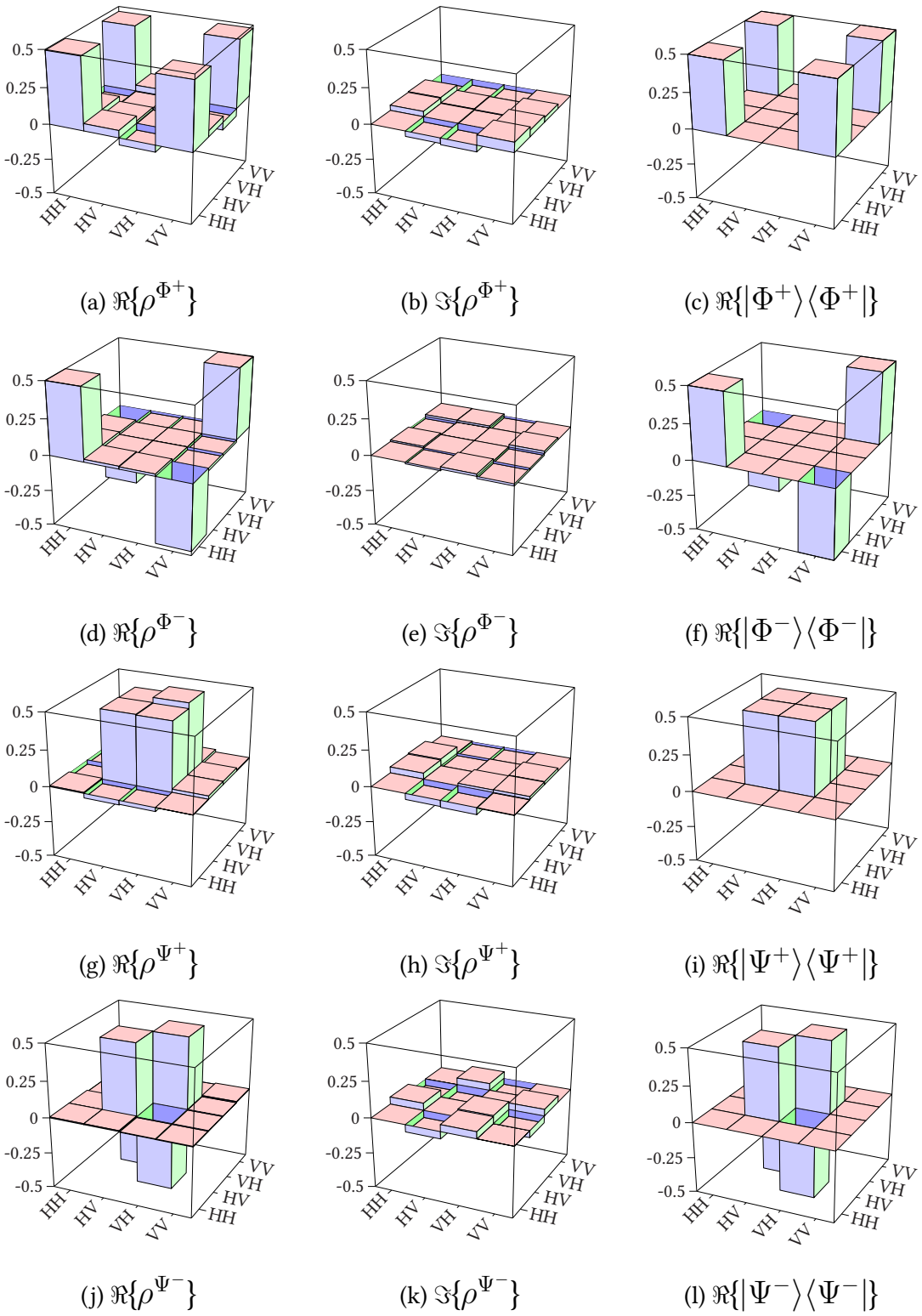

(a) $\Re\{\rho^{\Phi^+}\}$ (b) $\Im\{\rho^{\Phi^+}\}$ (c) $\Re\{|\Phi^+\rangle\langle\Phi^+|\}$

(d) $\Re\{\rho^{\Phi^-}\}$ (e) $\Im\{\rho^{\Phi^-}\}$ (f) $\Re\{|\Phi^-\rangle\langle\Phi^-|\}$

(g) $\Re\{\rho^{\Psi^+}\}$ (h) $\Im\{\rho^{\Psi^+}\}$ (i) $\Re\{|\Psi^+\rangle\langle\Psi^+|\}$

(j) $\Re\{\rho^{\Psi^-}\}$ (k) $\Im\{\rho^{\Psi^-}\}$ (l) $\Re\{|\Psi^-\rangle\langle\Psi^-|\}$

Figure 3.7: Reconstructed density matrices of prepared states. The first two columns represent real and imaginary parts of density matrices for experimentally reconstructed Bell's states $|\Phi^{\pm}\rangle$ and $|\Psi^{\pm}\rangle$. The third column represents real parts of target states whose imaginary parts are always zero, and are thus not presented.

states, quantum tomography was used. In this section it will be show, that these states will violate CHSH inequality[52] defied by formulas (3.2) and (3.4).

The final CHSH operator $\langle S \rangle$ was calculated for both, the raw data without subtracting accidental coincidences as well as for data with the subtraction. Obtained value of CHSH operator for raw data was $\langle S \rangle = 2.678 \pm 0.014$, while for data with accidental coincidences subtracted it was $\langle S \rangle = 2.731 \pm 0.014$. Using simple formula $(\langle S \rangle - 2)/\Delta\langle S \rangle$, it can be seen, that such a value violate the CHSH inequality by more than 48 standard deviations.

3.5 Summary

In this chapter, generation of four Bell's states using Kwiat's source based on two thin Type I crystals with CW pumping was presented. In order to characterize generated states, polarization quantum tomography using maximum likelihood estimation was adopted. From derived density matrices a quantitative measures purity, fidelity, and concurrence were calculated. The obtained quantum states were proven to have very high purity, fidelity, as well as the concurrence and were found to be suitable for non-locality test by CHSH inequality violation.

4

Bragg Reflection Waveguide

Quantum optics, or quantum physics in general, has already become well established with high potential benefits for many optical fields like computation, information processing, or metrology. Even though a majority of experiments taking advantages of quantum mechanics are built only as a prove-of-principle demonstrations in laboratories, a step towards a real world can be expected as soon as a easily handle devices for generation, manipulation, and analysis of quantum states will be regularly available.

In this chapter, a gallium arsenide based Bragg reflection waveguide formed by two Bragg reflectors on both sides of a core will be studied. These structures can be used as a source of second-order nonlinear interactions. It will be shown, that two completely different types of spatial modes can propagate through this device. The first type is guided by a total internal reflection while the second one is guided by a Bragg reflection instead. It will be demonstrated, that a perfect phase-matching can be achieved due to modal dispersion properties of this waveguide if the interacting fields propagate as these two modes respectively. Finally, an experimental generation of non-classical quantum states will be presented.

Research presented in this chapter was realized by the author at the Institute of Photonic Sciences in Castelldefels (Barcelona), Spain in collaboration with group of prof. Juan P. Torres and published in paper by Vallés *et al.* [65].

4.1 Introduction

As was shown in previous chapter, bulk crystals can be well fitting laboratory sources of non-classical states. On the other hand, when similar source would be requested for real practical application, design based on bulk optics will hardly be the optimal choice. One of the most advantage strategy in this case would be represented by integrated optical cir-

cuits based on waveguide structures. This is because they well respond to the requirements of practical applications such high generation efficiency and versatility, compactness, and solidness of the overall design. High efficiency of the source is important in order to reduce power requirements, and therefore for a low power consumption pumping diode lasers to be integrated on the very same chip. The versatility can be advantageous for generation of various types of different quantum states. Finally, the solid and compact design can allow for the device to be used as a standalone, easily handled black-box device without the need for constant maintenance.

As it was already stated, a periodically-poled waveguides can be used as an efficient source with huge potential for integration. However, Bragg reflection waveguides (BRWs) based on gallium arsenide (GaAs) open the possibility to take advantage of well mastered GaAs growth technologies. From the nonlinear optics point of view, the advantages are especially high nonlinear coefficients ($d_{36} = 170\,\mathrm{pm\,V^{-1}}$[66]), large transparency window in IR region (from 0.9 µm to 17 µm), and high optical damage threshold. The most beneficial advantage is however mature fabrication technology, which can be adopted in order for various different elements including pump laser[67] to be fabricated on the very same chip.

Even though GaAs possess high nonlinear coefficient, it also suffers from large dispersion, which makes it difficult to achieve a phase-matching. Although a range of different approaches was used in order to fulfil the phase-matching condition[10,68–73], only technique exploiting modal dispersion properties of the waveguide leaves the structure still suitable for later monolithic integration. The modal phase-matching technique used for this structure is taking advantage of two different spatial modes being supported, where the effective refractive index for spatial mode guided by the Bragg reflection is lower than effective index of conventional mode based on total internal reflection (TIR). Therefore, the effective refractive index of TIR mode on long wavelength can be equal to the one of BRW mode on short wavelength, so as a consequence the exact phase-matching can be tailored via proper design of the structure.

In recent years, various nonlinear processes have been observed experimentally in GaAs-based BRWs, such second-harmonic generation[74,75], sum-frequency generation[76], and even spontaneous parametric down-conversion[77]. It is evident though, that together with also demonstrated diode laser source based on BRW, which emits light directly in form of spatial Bragg mode[67], GaAs-based BRWs possess high potential in creating monolithic integrated devices. Another advantage, that also pushes these devices towards a real applications is the possibility to operate them in infrared spectral region, especially at 1550 nm, which is the dominant spectral region for long-distance telecommunications. Therefore, a standard communication networks and elements can be used in order to distribute or manipulate generated fields.

4.2 Theory

In this section, the introduction into theory behind BRW will be presented. It will be demonstrated, how it is possible to confine optical fields to these structures and how to fulfil phase-matching condition for different guided modes.

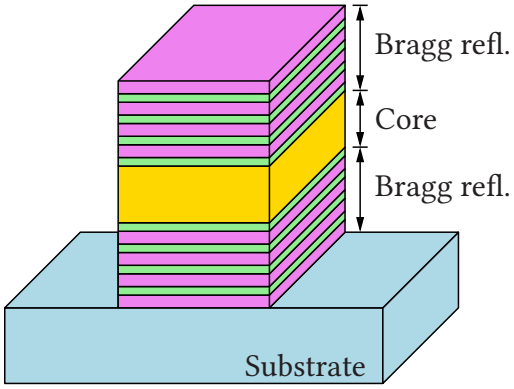

Figure 4.1: Schematic illustration of Bragg reflection waveguide based on two symmetrical Bragg reflectors made of two periodically alternating layers separated with a core layer. The whole structure is grown on a substrate by a chemical vapor deposition technique and etched to form a ridge.

4.2.1 Material and Design

Bragg reflection waveguides (BRWs) stand in general for any waveguide, where the light is confined within some restricted region by the Bragg reflection and not by the total internal reflection (TIR) as it is in the case of conventional waveguides. Even though these structures can be designed in various shapes, a planar slab design will be here considered. Additionally, a structure in form of ridge can be created by etching from planar slab device as illustrated in the figure 4.1. As can be seen from the figure, the core of the waveguide, where the most of the field energy is concentrated, is sandwiched in two symmetrical Bragg reflectors made of periodically alternating layers with different refractive indices. The whole waveguide is grown on a substrate which defines the length of the waveguide, and which can be afterwards etched to form a ridge of particular width and depth.

Naturally, the modal structure will depend on the material, respectively on the refractive indices of all layers and their thickness. As for the material, the BRW was based on layers of $Al_xGa_{1-x}As$. Changing the alloy composition index x, layers with different refractive indices can be created. Concerning the layout, there exist several typical designs, like quarter-wave BRWs (QW-BRWs)[78] or matching-layer BRWs (ML-BRWs)[79]. The first one, the QW-BRWs have cladding layers of thickness of one quarter of the wavenumber of guided wave, which provides the most rapid field decay in the claddings[80], and therefore the highest confinement in the core. Since the quarter-wave condition puts restrictions over the waveguide design, the QW-BRWs can suffer from lower efficiency in nonlinear interactions due to smaller spatial overlap. The solution to that is to separate the core from the Bragg's mirrors with additional layer called matching layer, which can be under a special circumstances understood as a part of the core.

Let it be known, that due to the presence of layers with different refractive indices, a conventional spatial mode based on total internal reflection can be also guided through the struc-

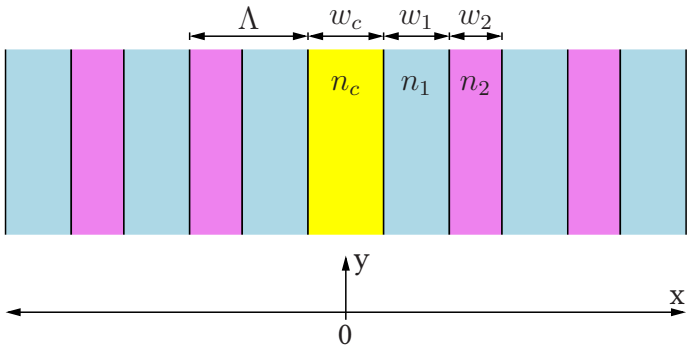

Figure 4.2: Schematic illustration of slab Bragg reflection waveguide used for derivation of transverse mode profile of Bragg mode.

ture. From this perspective it is important to understand the meaning of the term 'core'. Core here means the single layer (or combination of multiple layers) between two Bragg's reflectors, not a layer surrounded by medium of lower refractive index as it is usually understood when conventional waveguides are considered. The coexistence of Bragg modes and modes based on total internal reflection will become important, when the phase-matching of nonlinear interaction will be investigated.

For the case of nonlinear interaction, the waveguide has to be designed not only to fulfil the phase-matching through modal dispersion by manipulating the material itself and its layout, but also to ensure high spatial overlap. Even though the design, especially with use of matching layers, can be straightforward, in reality it is usually product of numerical optimization with respect to the efficiency of nonlinear interaction, where the fabrication limitations and imperfections have to be taken into account.

4.2.2 Spatial Profile of Guided Mode

In order to obtain transverse field distribution for Bragg reflection waveguide, let us consider a slab structure schematically depicted in the figure 4.2 made of core of the width w_c with refractive index n_c sandwiched in two identical periodic Bragg reflector consisting of two thin layers of widths w_1 and w_2 and refractive indices n_1 and n_2, respectively. Periodicity of the structure can be expressed as $n(x) = n(x + i\Lambda)$, where $x \in \langle -\infty; -d_w/2\rangle \cup \langle d_w/2; \infty\rangle$, $\Lambda = w_1 + w_2$ is the period and i is a natural number.

The propagation of field inside such structure can be formally described with plane wave reflected by a Bragg reflections at the interface $x = \pm w_c/2$, where for well guided modes, the incident angle θ must satisfy Bragg condition $m\lambda = 2\Lambda\cos(\theta)$, where λ is the wavelength and m is a natural number. To derive a spatial distribution of the electromagnetic field, TE mode will be considered.

Guided mode is assumed to propagate along z axis through an infinite medium ($x, z \in \langle -\infty; \infty\rangle$) symmetrical along y axis ($\partial_y = 0$). In this case, the only component E_y of electric

vector **E** can be expressed as

$$E_y(x,z,t) = \begin{cases} \left[C_1 \cos(k_c x) + C_2 \sin(k_c x)\right] e^{i(\omega t - \beta z)} & |x| \leq \dfrac{w_c}{2}, \\ E_K\left(|x| - \dfrac{w_c}{2}\right) e^{-iK(|x| - \frac{w_c}{2})} e^{i(\omega t - \beta z)} & |x| > \dfrac{w_c}{2}, \end{cases} \tag{4.1}$$

where $E_K(x)e^{\pm iKx}$ is Bloch wave function of electric field in the layered medium with Bloch wave vector K given by periodicity of the cladding and $E_K(x)$ is periodic with period Λ[7]. Parameter k_c from the equation (4.1) denotes the wave vector in the core and ω and β are the angular frequency and propagation constant of guided mode. Finally, the parameters $C_{1,2}$ are constant and determine, whether the mode is odd or even.

The overall solution can be obtained simply by matching particular solutions from equation (4.1) to be continuous on the boundaries together with their first derivative $\partial_x E_y$. Final mode condition (i.e. dispersion relation) for TE wave is therefore

$$ik_{1x}\left(\frac{e^{iK\Lambda + \frac{k_{1x}}{k_{2x}}}}{e^{iK\Lambda + \frac{k_{2x}}{k_{1x}}}}\right) = \begin{cases} -k_c \tan\left(k_c w_c\right) & \text{for even modes,} \\ k_c \cot\left(k_c w_c\right) & \text{for odd modes,} \end{cases} \tag{4.2}$$

where $k_{ix} = \{[(\omega/c)n_i]^2 - \beta\}^{1/2}$ are the transverse wave vectors in two layers of Bragg mirror.

Considering a quarter-wave layered stack it is ensured, that a confined propagation is obtained. This is due to the fact, that Bragg reflectors create a stop-bands in energy, where the solution is complex with Bloch vector in following form

$$K = \frac{m\pi}{\Lambda} \pm i\mathcal{K}, \tag{4.3}$$

where parameter m denotes m-th order of forbidden band, while imaginary part $\mathcal{K}$ ensures evanescent exponential decay of Bragg mode envelope.

The final solution for one particular design of Bragg waveguide with finite number of layers in Bragg stacks is depicted in the figure 4.3, where high confinement of the filed in the core as well as the exponential decay in the cladding can be identified. For real structures the number of layers is always limited to some small number. This however results only in non-unity reflectivity of the Bragg mirrors, and it does not affect the intensity distribution in the waveguide or propagation constants of guided modes.

4.2.3 Principle of Phase-Matching

GaAs is a cubic crystal with symmetry class $\bar{4}$3m. Since it is optically isotropic the usual birefringence technique can not be therefore used in order to phase-match nonlinear processes. Several different techniques of phase-matching have been however adopted so far to fulfil the phase-matching. Except of quasi-phase-matching techniques[68,70,71], also methods offering full exact phase-matching like form-birefringence method[69] or technique of modal phase-matching[10] have been utilized. The disadvantages of these methods are, that the resulting elements are not suitable for further integration.

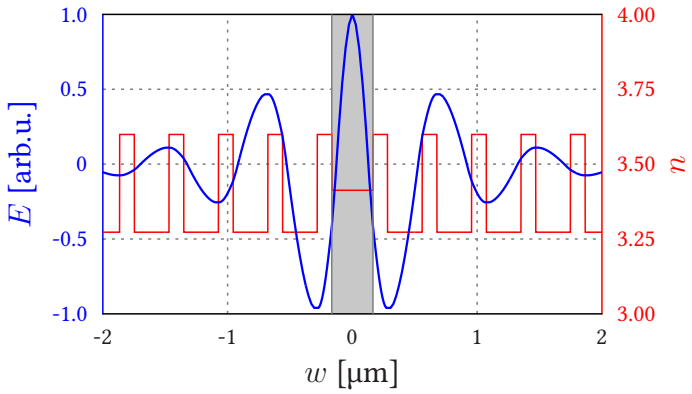

Figure 4.3: Numerically calculated distribution of electric field vector E of a Bragg mode in transverse plane of real Bragg reflection waveguide characterized by spatial profile of refractive indices also depicted in the plot. The core of the waveguide is highlighted with grey filing.

In contrast to that, a technique presented here represents an exact phase-matching utilizing strong modal dispersion properties of propagating modes. The main feature responsible for modal phase-matching in BRWs is, that Bragg modes possess effective modal indices $n_{\text{eff}} = \beta/k_0$ much lower than the ones of conventional modes based on total internal reflection. This fact can for properly designed structure lead to situation, where effective modal index of Bragg mode at shorter wavelengths (2ω) is equal to TIR mode at longer wavelength (ω). The complete analytic description of such modal phase-matching will not be introduced here though, since it requires usually numerical solution of dispersion relations of both Bragg and TIR modes simultaneously[81].

4.3 Experiment

In this section, generation of entangled photon pairs in Al_xGa_{1-x} BRW will be studied using spontaneous parametric down-conversion (SPDC) at typical telecommunication wavelength 1550 nm. Although the SPDC process was already observed as well, no further steps towards synthesizing more complex non-classical quantum states were taken and only intensity correlation measurements were done[77].

In order to generate SPDC we first decided to create a spatial field distribution in form of Bragg mode using spatial light modulator (SLM) and couple it into the BRW structure. According to phase-matching condition, the down-converted photons should be created in form of conventional TIR mode. By measuring violation of Bell's inequalities, the quantumness of generated states can be demonstrated.

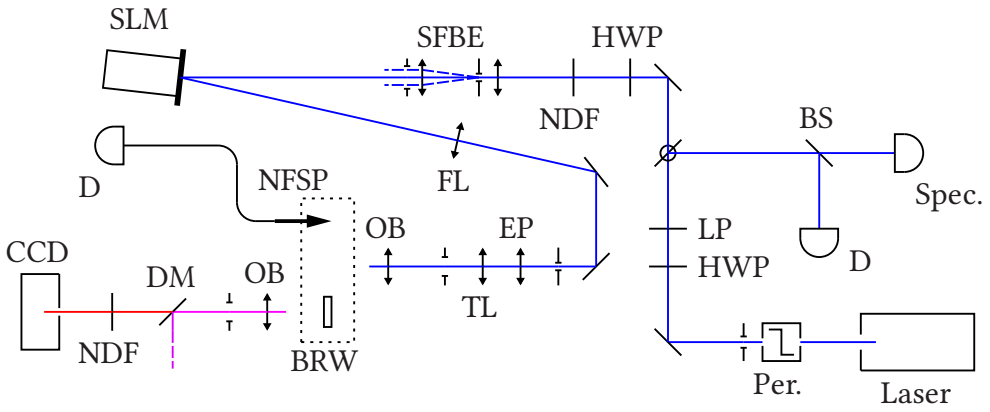

Figure 4.4: Sketch of an experimental setup used in the first stage of the experiment with generation of Bragg mode. HWP: half-wave plate, LP: linear polarizer, NDF: neutral density filter, SFBE: spatial filter with beam expander, SLM: spatial light modulator, FL: Fourier lens, EP: eyepiece, TL: tube lens, OB: microscope objective, NFSP: near-field scanning probe, BRW: Bragg reflection waveguide, DM: dichroic mirror, CCD: CCD camera, BS: beamsplitter, D: detector, and Spec.: spectrometer.

4.3.1 Experimental Setup I

The experimental setup used in this stage of experiment is depicted in the figure 4.4. As a source, tunable semiconductor laser with external cavity DLX 110 (Toptica Photonics) was used in CW regime. The laser beam passed through the optical attenuator consisting of half-wave plate (HWP) and linear polarizer (LP) and additional HWP for setting optimal pump power and polarization. Next, the beam was spatially filtered and expanded by a beam expander (SFBF) for optimal performance of the spatial light modulator (SLM) PPM X8267 (Hamamatsu). The hologram from SLM was reconstructed with a Fourier lens (FL) in its focal plane. Since the reconstructed mode is approximately thousand times bigger with respect to the BRW's dimensions, it had to be resized down to the desired size using home-made microscope consisting of eyepieces (EP), tube lens (TL), and microscope objective (OB).

After that, the mode could be either coupled into the waveguide or analysed with near-field scanning probe (Veeco) in order to check its intensity distribution. Both the waveguide and the probe were placed on precise 3-axis linear stage NanoCube P-611.3S (Physical Instrumente) with sub-nm resolution to precisely position the waveguide in the beam or to make fine three-dimensional scan of the mode (see figure 4.5). If the mode was coupled into the structure, the decoupled pump was monitored with CCD camera to check the coupling.

Mode Preparation and Reconstruction

The spatial light modulator (SLM) in phase modulation regime was used in order to create a desired light intensity distribution of the Bragg mode, which was to be coupled into

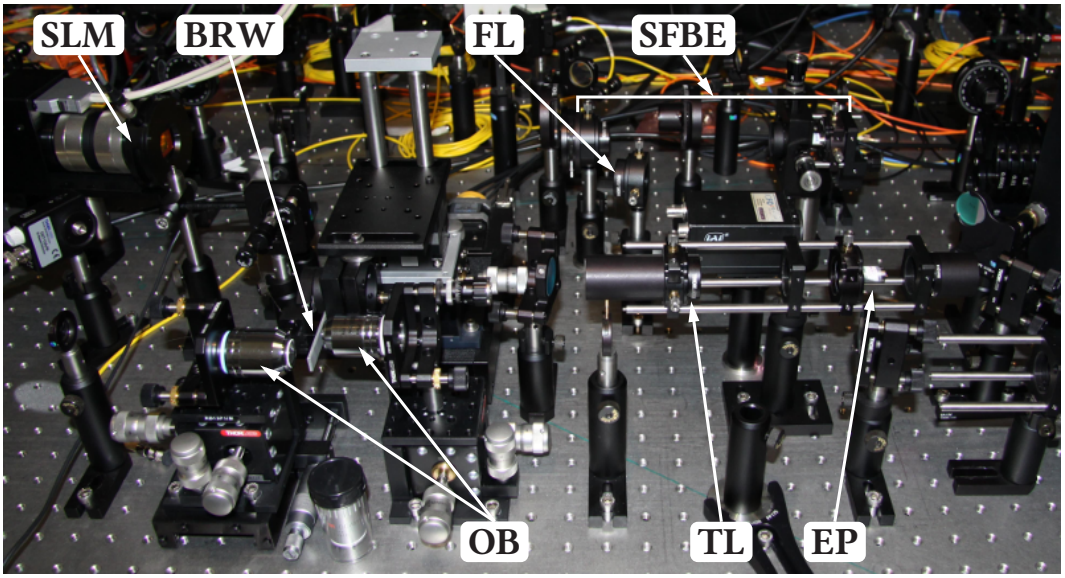

Figure 4.5: Photo of the main part of the experimental setup showing positioning of Bragg waveguide with scanning probe as well as mode preparation stage (labels correspond to those from figure 4.4). At this moment, the waveguide is removed and the probe is used to scan profile of the pump beam prepared for coupling.

the waveguide. The SLM modulates the phase distribution according to displayed hologram. The hologram was afterwards reconstructed with the Fourier lens.

Even though the calculation of the optimal hologram should be relatively straightforward, if the real parameters of the SLM like resolution, range, phase shift, etc. are taken into account, it appeared to be much more difficult. Finally the hologram depicted in the figure 4.6 was found to be optimal choice, also from the diffraction efficiency point of view. The reconstruction of the mode was performed using a simple Fourier lens and the resulting intensity distributions can be seen in the figure 4.7, where both first diffraction orders are depicted.

Pump Mode Coupling

Together with the mode preparation, this was the most challenging part of the experiment due to the fact, that the typical size of the fine features of desired mode was about 300 nm, which was in order of diffraction limit for pump wavelength 775 nm. Also, since the reconstructed mode was approximately 1000 times larger than the structure, the size had to be reduced accordingly.

To sufficiently reduce the mode dimensions together with maintaining high spatial frequencies of the mode, the infinity corrected microscope was build. The microscope consisted of single lens eyepiece, tube lens, and 100× microscope objective (Nikon). Using tube lenses of different focal lengths a different magnification was achieved as $M = f_{tl}/f_{ob}$. It was however found, that especially due to the limited aperture of the microscope objective, the optimal magnification was possible to achieve only at expenses of high quality reduction

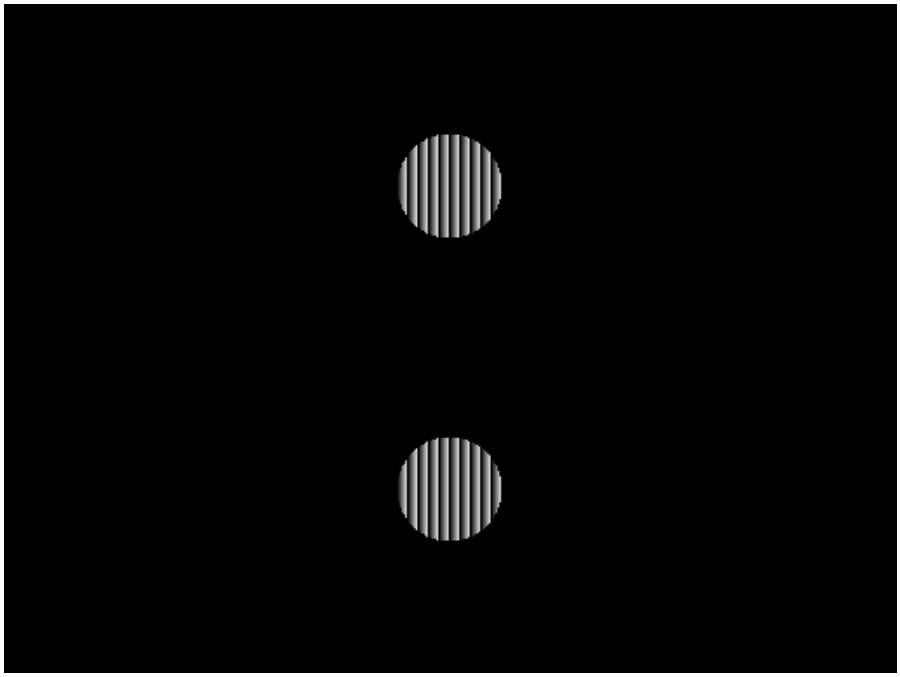

Figure 4.6: Phase hologram projected on spatial light modulator (SLM) in order to generate desired Bragg mode. The hologram was created as a blazed diffraction grating covered with two circular aperture mask.

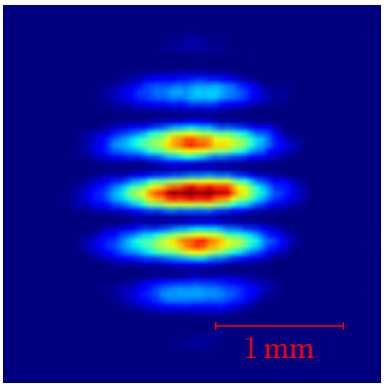

(a) +1 Diffraction order

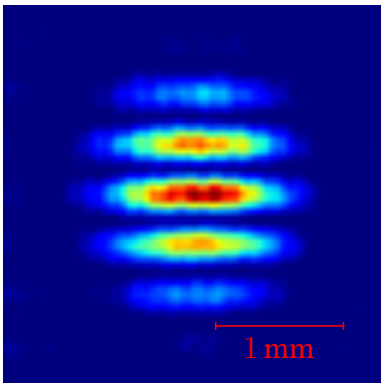

(b) -1 Diffraction order

Figure 4.7: The reconstruction of hologram projected on spatial light modulator (SLM) using Fourier lens (FL) in its focal plane. Both fist diffraction orders are shown, however due to the blazed grating the intensity of minus first one is significantly lower. The images were captured with CCD camera.

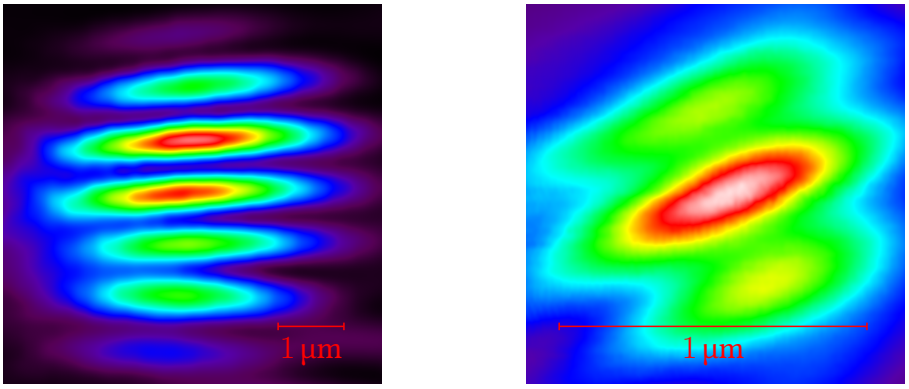

(a) (b)

Figure 4.8: Demonstration of resizing of reconstructed hologram with home made microscope under two different magnification. (a) Size approximately twice larger with respect to the waveguide. (b) Size of the mode which fits the requirements, however its shape is significantly corrupted due to the limited aperture of the microscope objective.

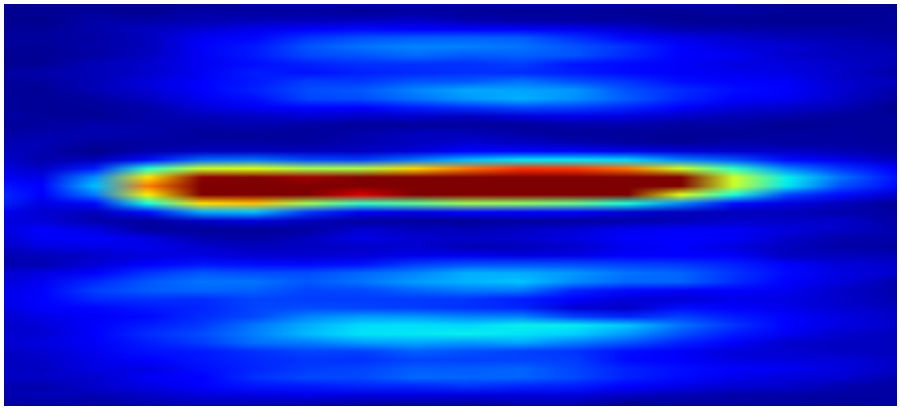

Figure 4.9: Intensity distribution of light inside the waveguide after coupling a Bragg mode (see figure 4.8b). High intensity confinement in the core can be identified in the centre of the image together with a side lobs significantly weaker due to the non-optimal profile of coupled mode.

together with high losses. The minimal obtained size of the mode was about 4 µm, which was still twice bigger than the structure itself. Figure 4.8 shows intensity profiles of both modes measured using scanning probe with aperture 50 nm connected to a single photon detector.

Even though the intensity profile of the Bragg mode of correct size was already corrupted due to the limited aperture of the microscope objective, it was coupled into the waveguide. The light decoupled from the structure using another microscope objective and captured by CCD camera can be seen in the figure 4.9. In this figure, the centre core with high power confinement together with side lobs can be identified. The coupling efficiency was however critically low, with pump power limited by the SLM damage threshold, in order to perform any nonlinear experiment.

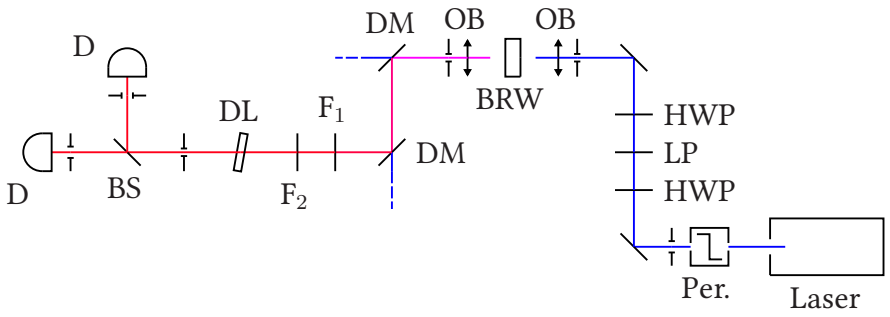

Figure 4.10: Schematic sketch of an experimental setup used in the second attempt with using Gaussian pump mode instead of the Bragg mode. HWP: half-wave plate, LP: linear polarizer, OB: microscope objective, BRW: Bragg reflection waveguide, DM: dichroic mirror, F_1 and F_2: band-pass and long-pass interference filters, DL: birefringence delay line, BS: beamsplitter, and D: detector.

4.3.2 Experimental Setup II

Due to the difficulties in coupling Bragg mode into the structure, different BRW element based on matching-layer design was used. Because of that, it was possible to use Gaussian mode as a pump directly. This resulted in more efficient coupling together with higher final conversion efficiency, even though the spatial overlap of Gaussian and Bragg modes is only 20 %.

The waveguide itself consisted of 500 nm wide core surrounded by two 375 nm wide matching layer, sandwiched by Bragg reflectors[82]. The structure was afterwards etched to form a ridge with dimensions w×d×l = 4.4 µm×3.6 µm×1.2 mm. The overall layout was designed to fulfil Type II phase-matching at 775 nm (775 nm→1550 nm).

Since due to the fabrication imperfections, both the dimensions as well as the aluminium concentrations may vary, the device was first characterized in the process of second-harmonic generation in order to check for the proper phase-matching wavelength. After that, an experimental setup depicted in the figure 4.10 was used for generation of entangled two photon states[83] and later for obtaining the CHSH inequality violation[52]. The setup was rebuild as shown in the figure 4.10. Since the Gaussian mode from the laser was used directly, the SLM with Fourier lens was removed. The pump power was about 6.5 mW.

Decoupled SPDC signal was first separated from the residual pump using set of dichroic mirrors (DM) and interference filters (IF). The quality of entanglement was reduced as a consequence of using Type II process, where both generated photons have orthogonal polarization. They can be therefore distinguished by their arrival time and also by their spectra[84]. In order to compensate for that, a birefringence delay line (DL) and band pass filter (F_1) were used.

With 50/50 beamsplitter, Bell's state $|\Psi^+\rangle = (1/\sqrt{2})(|H\rangle|V\rangle + |V\rangle|H\rangle)$, where $|H\rangle$ and $|V\rangle$ denotes horizontal and vertical polarization states, respectively was generated in 50 % cases, when both photons propagated to different output of the beamsplitter. This was per-

formed by measuring in coincidences only (post-selection technique). The quality of entanglement was measured using Bell's like CHSH inequality violation. The detectors used for this measurements were InGaAs single-photon counter modules ID201 (ID Quantique).

4.4 Results

First, the correlations in polarizations were verified. In this case, when signal is projected into horizontal polarization for instance, a coincidence rate of idler photon projected into state $|\theta_2\rangle = \cos\theta_2|H\rangle + \sin\theta_2|V\rangle$ should form a fringes described by formula $P(|H\rangle, |\theta_2\rangle) = \cos^2\theta_2$. Experimentally obtained visibilities of coincidence fringes for two different settings of signal projection $|\theta_1\rangle$ were $V(\theta_1 = 0°) = 98\,\%$ and $V(\theta_1 = 45°) = 91\,\%$ with subtraction of accidental coincidences. The accidental coincidence rate was measured experimentally by introducing additional delay to the trigger of one detector, thus measuring accidental correlation of physically uncorrelated events.

The CHSH inequality violation test was performed exactly as described in chapter 3. The maximum violation ($S = 2\sqrt{2}$) should be obtained for signal and idler photons projected into states characterized by angles $\theta_1 = 0°$, $\theta_1' = -45°$ and $\theta_2 = 22.5°$, $\theta_2' = 67.5°$. Experimentally obtained Bell factor S was 2.61 ± 0.16, which proved, that the generated photon pairs were quantum correlated by violation the CHSH inequality by more than 3 standard deviations.

4.5 Summary

It was shown, that Bragg reflection waveguides can serve as an alternative to more convenient nonlinear devices such a PP-KTP or PP-LN. It was demonstrated both theoretically and experimentally, that it is possible to achieve exact phase-match between spatial modes guided by a total internal reflection and Bragg reflection, respectively. Due to hight nonlinear coefficient of GaAs, this device is more than suitable for nonlinear optics. Using already well developed fabrication techniques, similar devices may be easily integrated into more complex structures including laser sources. It was also mentioned, that manipulating its dimensions together with aluminium concentration, the parameters of the waveguide such a group velocity dispersion can be tailored.

Finally, the generation of polarization-entangled photon pairs in process of spontaneous parametric down-conversion in Bragg waveguide based on matching layer design was demonstrated. The non-classicality of generated quantum state was verified by violating Bell's like CHSH inequality.

It is however clear that further technological development is needed in order to achieve better performance of this device and overcome currently more conventionally used devices.

5

Spatial Correlations in Spontaneous Parametric Down-Conversion

Photons pairs generated by spontaneous parametric down-conversion are due to its nature correlated in several degrees of freedom. These correlations are responsible for the non-classical behaviour of generated fields. It is however important to stress out, that these correlations exist only between two photons from a single pair, not between any successive sets.

In this chapter, the spatial correlations of optical fields generated by parametric down-conversion in bulk crystal will be characterized in far-field. The attention will be given especially to spatial correlations and their evolution when moving from regime with single-photon rates of generated down-conversion to regime where macroscopic fields are generated. It will be demonstrated, that spatial correlation functions measured at single-photon level correspond in the same experimental setup to speckle pattern formed at high intensity regime, since both these effects have the same quantum origin.

This experiment was performed by the author at the University of Insubria in Como, Italy under the supervision of prof. Maria Bondani and published in paper by Machulka *et al.* [85].

5.1 Introduction

The process of (spontaneous) parametric down-conversion [(S)PDC] in nonlinear media has become a well established source of optical fields possessing both spatial and spectral correlations[86] as well as correlations in photon numbers[87,88] and time[5,89,90]. Correlations in intensity and time result from the fact, that photons are generated in pairs, even though the nature of this process is completely probabilistic and the pairs are generated randomly. Correla-

tions in momentum and frequency result, on the other hand, from momentum and energy conservation laws, respectively.

The existence of spatial correlations between photons generated in SPDC process has already been well known and also experimentally verified several times using either scanned single-photon detectors[63,91,92] or intensified CCD cameras (iCCD)[88,93]. These experiments were however performed in low-gain regime at single-photon level containing mostly one photon per time only. The aim of these measurements was to determine the size of correlated areas.

On the other hand, if the PDC process is generated with extremely intense pump (high-gain regime)[94,95], the process becomes stimulated by itself. This leads to formation of speckle pattern as a consequence of partial coherence of successively generated photons. Both, the low-gain regime and the high-gain regime can be understood as two opposite sides of the same coin, since they both originate in the same nonlinear interaction. While in the low-gain regime the field is well described by highly non-classical multi-mode Fock states with completely random phases, in the high-gain regime the generated field can be characterized by classical multi-mode thermal state with well defined phase properties[96]. It is therefore interesting to study the coherence properties simultaneously in both regimes.

5.2 Theory

In this section, a basic theoretical treatment of both regimes will be presented. In low-gain regime the coherence areas will be defined, while in hi-gain regime the formation of characteristic speckle pattern will be discussed.

5.2.1 Coherence Areas

In ideal case, when the SPDC process in nonlinear medium of infinite dimensions is pumped with a monochromatic plane-wave, the down-converted fields are generated in the form of monochromatic plane waves with frequencies ω_s and ω_i for signal and idler wave, respectively. These frequencies are determined by the energy conservation law, while the propagation directions of these two waves are restricted by the phase-matching condition (i.e by the momentum conservation law). This means, that if the signal photon is detected, the frequency and emission direction (position) of the idler photon is determined exactly with no uncertainty.

However, in the case of finite crystal and beam dimensions and nonmonochromatic pump, the correlations in spatial positions are blurred due to the uncertainties in frequencies and wave vectors of interacting fields. First, the finite length of the crystal and width of the pump beam result in imperfect phase-matching, where a momentum mismatch of wave vectors is tolerated to some extent. Second, the finite spectral width of the pump allows for more relaxed energy conservation. As a consequence, light emitted to any direction is no longer monochromatic, and if the signal photon is detected in one particular emission direction, the corresponding idler photon can be located in the so-called coherence area defined by

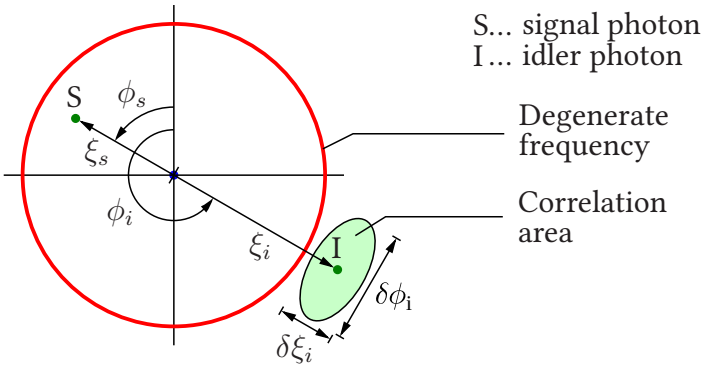

Figure 5.1: Schematic illustration of coherence area in transverse plane with polar coordinate system (ξ, ϕ). Relative position of idler photon (I) with respect to the signal one (S) is determined by perfect phase-matching condition, while the uncertainties in both directions $(\delta\xi, \delta\phi)$ forming the coherence area are consequences of finite dimensions of crystal and pump beam together with finite spectral width of the pump.

a finite angles in radial (ξ) and azimuthal (ϕ) directions. It is essentially an area in detection plane defined usually as a FWHM of appropriate cross-correlation function, where the probability of occurrence of corresponding photon from a pair is sufficiently high. The graphical representation of such coherence area is schematically illustrated in the figure 5.1, where the uncertainties in both the radial and the azimuthal directions are depicted. Moreover, although the pump beam is spatially coherent, the down-converted fields generated in different directions are statistically uncorrelated. Also as there is no phase relation between different photon pair emission, the phases of signal and idler fields are also completely random[97].

Coherence area defined above is given by the fourth-order cross-correlation function (photon coincidence probability) $\Gamma^{(4)}_{si}$[97,98]. Since the correlation function Γ is usually smooth one peak function, it can be quantitatively described by its widths in both radial and azimuthal directions $\Delta\Gamma_{si,\xi}$ and $\Delta\Gamma_{si,\phi}$, respectively.

It was already shown both theoretically[97,99,100] as well as demonstrated experimentally[86,101], that it is possible to tailor coherence areas by pump beam properties. It can be shown, that in the radial direction, the width of the correlation function is determined mainly by the spectral profile of the pump and by the length of the crystal, while in the azimuthal direction the correlation function size is modulated especially by the transverse profile of the pump beam. Going into more details, the crystal length together with the finite spectral width of the pump affect the radial width through the imperfect phase-matching in longitudinal direction. As can be shown, the radial width of coherence area increases with increase of pump spectral width and decrease of crystal length.

On the other hand, width of the coherence area in the azimuthal direction is dominantly determined by the spatial profile of the pump beam. As can be shown, the size of coherence area in the azimuthal direction is increasing with decrease of the pump beam size. Reason,

why the radial width is not significantly affected by the width of the pump beam is, that for commonly used crystals with typical length in units of millimetres, the phase-matching conditions in longitudinal direction are much more restricting than these in the transverse (radial) direction[86].

5.2.2 Speckle Pattern

Due to the fact that the SPDC process is spontaneous (i.e. stimulated by vacuum fluctuations), the overall efficiency is rather low (typically about 10^{-10}). Adopting combination of standard laser source with common nonlinear crystal, the generated fields are extremely weak, containing low mean number of photons per one spatio-temporal mode. In this case the SPDC belongs to a linear region with parametric gain $g \ll 1$*.

On the other hand in hi-gain regime ($g \gg 1$), the number of photons generated in each mode grows according to equation (1.55) rapidly with $\sinh^2(gz)$. Every coherence area is then therefore filled with large number of photons, thus forming a macroscopic field. As a consequence, the intensity profile in transverse plain resembles speckle pattern formed by partially coherent light scattered off a rough surface. Although the physical origin of both phenomena is completely different, the term speckle pattern is here also used. Individual speckle is thus created by stimulated parametric conversion initiated by spontaneous generation at the very beginning of the crystal.

Since the stimulated conversion was initiated by a pair of correlated photons, the final speckle pattern therefore has to preserve these correlations. For each speckle with approximate dimension of a coherence area there exists a symmetrical one located in area corresponding to phase-conjugated mode with ideally the same number of photons (the corresponding speckles are therefore correlated also in photon numbers), while the number of speckles roughly coincide with number of degrees of freedom, i.e. number of spatio-temporal modes. The corresponding speckles propagate behind the crystal symmetrically with respect to the pump beam in direction restricted by the phase-matching, while their sizes are determined mainly by the size of coherence area, thus by the phase mismatch and partially by the gain-controlled stimulation of the conversion.

It was already theoretically predicted and experimentally demonstrated[94] and it will be here demonstrated as well, that size of the speckles is determined not only by the pump beam diameter as it is in the case of coherence areas, but also by a gain factor, thus by the pump power. This dependence stems from the fact, that in high-gain regime, the photons are produced closer to the centre of the beam, which effectively reduces the amplification area with respect to pump beam profile. Due to the inverse dependence of coherence area on the pump beam profile, the speckles are therefore slightly larger than the coherence areas.

In order to analyse the speckle pattern, the correlation functions have to be adopted as well. To experimentally estimate the size of the speckles, an intensity autocorrelation function $\Gamma_{\alpha\alpha}$, where $\alpha = s, i$ can be adopted[101]. On the other hand, the spatial cross-correlation function $\Gamma_{\alpha\beta}$, where $\{\alpha, \beta\} = \{s, i\}$, and which has origin in momentum entanglement of twin beams can be used to compare spatial correlations between couples of phase-conjugate

* $g = 1$ represents situation, where both spontaneous and stimulated contributions are in equilibrium.

modes in low- and high-gain regimes. Let it be noted, that an autocorrelation function in the case of low-gain regimes is identically equal to zero, since there usually exists no more than one photon per each mode.

While for the low-gain regime a perturbation approach can be adopted[93,102], the complete theoretical treatment of the high-gain regime requires a stationary, plane-wave pump approximation in order for the analytic description of the output state to be expressed[96]. However, for scope of this analysis the definition of the intensity correlation functions is sufficient.

If generated field is detected by CCD-like device, the intensity (i.e. number of photoelectrons) detected by one pixel at position $\mathbf{r}$ can be written as $I_\alpha(\mathbf{r})$, where $\alpha = s, i$ represent signal or idler region. The variance $\Delta I_\alpha(\mathbf{r})$, which represent fluctuations around the mean value, can be therefore defined as $\Delta I_\alpha(\mathbf{r}) = I_\alpha(\mathbf{r}) - \langle I_\alpha \rangle$, where $\langle I_\alpha \rangle = (1/N) \sum_{x=1}^{N} I_\alpha(x)$, and where the summation is performed over all N pixels. The intensity spatial correlation functions can be therefore defined as

$$\Gamma_{\alpha\beta}(\Delta\mathbf{r}) = \langle \Delta I_\alpha(\mathbf{r}) \Delta I_\beta(\mathbf{r} + \Delta\mathbf{r}) \rangle, \tag{5.1}$$

where $\langle \cdot \rangle$ denotes statistical averaging over all symmetrical pixel pairs.

5.3 Experiment

This section will be devoted to the experimental characterization of PDC process in both regimes. Special attention will be given to the iCCD camera as a unique detector capable of operating in both regimes thanks to its high dynamic range.

5.3.1 Experimental Setup

In order to study both intensity regimes simultaneously, an experimental setup schematically depicted in the figure 5.2 was designed. Presented experimental setup allowed to investigate both intensity regimes simply by changing the power of the pump together with an acquisition parameters of the detector.

As a source, a third-harmonic of picosecond pulsed mode-locked Nd:YLF laser (High-Q Laser) at wavelength 349 nm with repetition rate about 500 Hz was used. First, a telescope with negative lens (Galilean type, GT) was used in order to reduce beam width and ensure good collimation of the beam. Second, the pump power was adjusted using attenuator (Att.) consisting of a single half wave plate and linear polarizer. Available power for this experiment ranged from 20 µW giving small number of photon pairs in generated field (low-gain regime) up to 50 mW, where speckle pattern occurs (high-gain regime). Finally, the UV beam pumped 8 mm long BBO crystal with cut angle $\theta = 37°$ designed for Type I phase-matching. Down-converted photon pairs at frequency degeneracy were therefore emitted into a cone with half opening angle 11.9°. One part of the cone layer (signal beam) was captured by the iCCD camera (DH734, Andor) directly, while the second, corresponding part (idler beam) was deflected to the camera by highly reflective dielectric mirror. The camera was placed 38.5 cm behind the crystal ensuring the far-field condition and was equipped

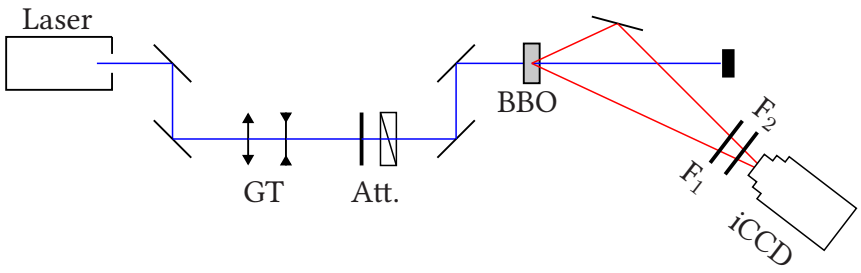

Figure 5.2: Schematic sketch of an experimental setup for measuring spatial correlations in field generated in process of (S)PDC. GT: Galilean telescope consisting of positive and negative lens, Att.: optical attenuator including half-wave plate and linear polarizer, BBO: BBO crystal, F_1 and F_2: long-pass and band-pass interference filters, respectively, and iCCD: iCCD camera.

with two interference filters. One long-pass edge filter F_1 to filter out a scattered pump and one band-pass filter F_2 with 40 nm bandwidth centred at 710 nm to determine (reduce) the width of the cone layer.

As a consequence, the image on the camera has a shape of two strips, one for the signal part of the cone layer and one for the idler one. On each camera frame, two virtual regions of interest (ROIs) can be thus defines in order to identify to which part of cone layer the particular detection event belongs. Let it be pointed out, that due to the reflection on the mirror, the idler strip is horizontally flipped. Since the second filter F_2 was relatively wide and not perfectly centered at degenerate frequency, slightly asymmetric non-degenerate photon pairs were detected. The camera was triggered by the synchronization logical pulse from the laser with detection window set to 5 ns to ensure that (S)PDC from a single pump pulse only was detected and to minimize the thermal noise and spurious ambient light. In order to minimize the thermal noise, the CCD chip was cooled down to $-20\,°C$. During the experiment, the pump power and pump beam size were monitored using power meter and scanning knife-edge technique, respectively. The pump beam was found to be slightly elliptical with excentricity of about 1.22.

5.3.2 iCCD Camera

The iCCD stands for intensified charge coupled device. Essentially, it is standard CCD chip equipped with an image intensifier. The whole device consists of several main parts. The image intensifier, CCD chip, cooling, and some control electronic. The electronic allows for a precise synchronization of the camera and for reading out the data from the CCD chip which can be done under various different settings usually representing a trade-off between speed and performance (especially noise level). The thermoelectric cooling (two-stage Peltier element) can significantly reduce the thermal noise of the CCD chip. The lowest achievable temperature without additional water cooling is about 40 °C below the ambient temperature, thus about $-20\,°C$ in standard laboratory environment. The CCD chip was a standard sci-

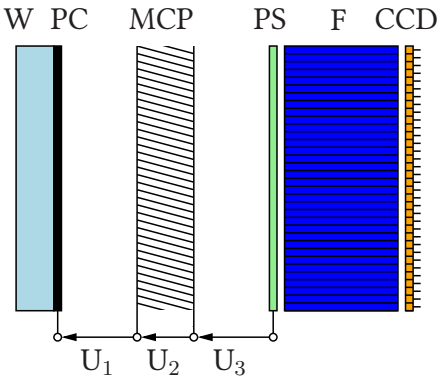

Figure 5.3: Schematic illustration of an iCCD image intensifier. W: glass window, PC: photocathode, MCP: micro-channel plate, PS: phosphor screen, F: fiber optics tapered bundle, and CCD: CCD chip. Typical voltage levels are: $U_1 \sim 100\,\mathrm{V_{pp}}$, $U_2 \sim 1\,\mathrm{kV_{pp}}$, and $U_3 \sim 10\,\mathrm{kV_{pp}}$.

entific CCD chip with resolution $1024\times1024\,\mathrm{px}^2$ of size $13\times13\,\mu\mathrm{m}^2$, therefore with the total active area of $13.3\times13.3\,\mathrm{mm}^2$. The most important part is however image intensifier which is responsible for the single-photon sensitivity of this device.

The intensifier schematically depicted in the figure 5.3 consists of three parts, the transmission photocathode, micro-channel plate (MCP), and a phosphor screen. The photocathode made of some photosensitive compound (usually alkali metals with very low work functions) coated upon a glass window if struck by light emits a photo-electron. The material of photocathode is responsible for the spectral sensitivity and quantum efficiency of the camera. In the case of this particular device, the overal quantum efficiency reaches maximum of 27 % at 500 nm.

Emitted photo-electron is then accelerated towards an MCP made of small parallel tubes with diameter in units of μm and tilted at small angle with respect to the plate, ensuring the electrons will hit the walls of the tube. Each of these tubes serves as a continuous-dynode electron multiplier, in which the multiplication of electrons through the secondary emission takes place under the presence of strong electric field. The amplification, usually of several orders of magnitude, depends on the electric field strength and can be controlled via so-called MCP gain. The important feature of the MCP is the possibility to be closed by removing the electric field, and thus gating the detection. This feature has strong positive impact on noise performance of the camera. After that, the amplified electron stream hits the phosphor screen, where it causes light flash (i.e. the electrons are converted back to light).

These flashes are coupled into a fiber array and decoupled on the CCD chip (can be done also with a bulk optics), where they are detected in a standard way. Due to the amplification, the iCCD in this regime can serve as a multi-channel device, where each pixel acts as a binary detector with single-photon sensitivity. Because the MCP plate provides the spatial resolution, the spatial information about detection events on photocathode is transmitted to the CCD chip. However, since for technological reasons the contrast transfer is not perfect,

a single detection event is usually distributed over several pixels on CCD chip, thus effectively reducing its resolution. Because of that, the pixels can be physically grouped together during readout without losing spatial resolution, which not only improve readout rate, but also the dynamic range. Product of this grouping (or binning) is called super-pixel (s-px).

5.4 Results

In this section, results obtained in both regimes will be presented. In the low-gain regime the size of coherence areas will be determined, while in the hi-gain regime dependence of sizes of speckles on pump power and beam properties will be evaluated.

5.4.1 Single-Photon Regime

First, a coherence area in single-photon regime characterized by the intensity cross-correlation function $\Gamma^{(4)}_{si}$ in the transverse plane was measured. During this measurements, the MCP gain of the camera was set to its maximum value to provide single photon sensitivity. Hardware binning 8×8 was used in order to speed up the acquisition. Other acquisition parameters were adjusted to provide optimal trade-off between the speed of the acquisition and the noise level. The attenuator was adjusted so that the number of detected events was much lower than number of super-pixels, so all detection events could be spatially distinguishable. It was found that optimal photon rate is about 30–50 photons on average per frame (i.e. both signal and idler), which corresponds to pump power $P \simeq 20\,\mu\text{W}$. This ensured the probability of one photon being detected in one super-pixel to be much lower than unity, consequently neglecting probability of two or more photons falling into the same super-pixel.

The typical readout image from the camera can be seen in the figure 5.4, where the single shot frame (5.4a) is presented together with an accumulated image (5.4b) to demonstrate intensity distribution over the active area of the camera. Under such intensity regime, the camera serves as a photon number resolving detector for signal and idler separately. However, since the number of detection event per frame is relatively low, a long sequence of frames (of the order of 10^5) has to be acquired for purposes of statistical processing. This is the reason, why any speed up in acquisition is important, since such typical measurement can last up to 15 or more hours, in which the data might be corrupted by instability of the laser.

Figure 5.4a shows a typical read-out frame from the camera. In order to calculate correlation function, it is necessary to pre-process it first to identify particular detection events with their location. The pre-processing usually consists of removing a background (mainly thermal and readout noise) and applying the first threshold to separate individual detection events. After that, a special algorithms usually used for identification multiple stars in astronomical images[103] can be adopted in order to identify exact location of detection events, which are usually spread over more super-pixels or eventually to distinguish and separate two close, partially overlapping detections. Finally, the second threshold is applied to separate real photon events from the noise. This final step is important, since it determines the trade-off between quantum efficiency and the noise level. Essentially,

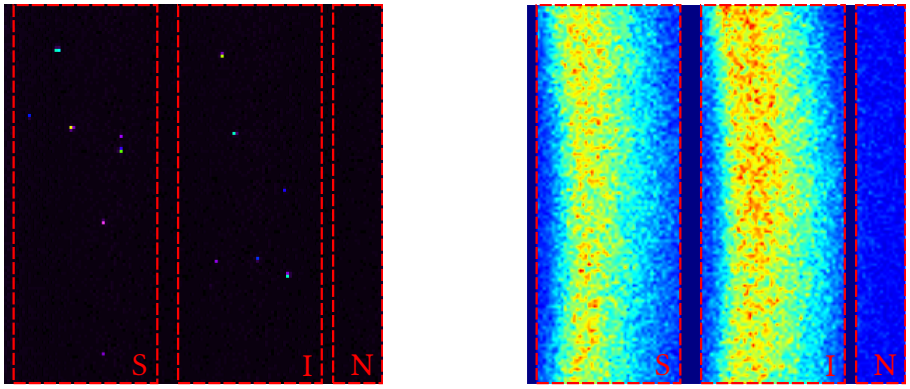

(a) Single frame (b) Accumulated frame

Figure 5.4: Typical single readout image from the iCCD camera without any pre-processing (a) and image formed as an accumulation of individual detection events (single readout frames) after pre-processing (b). Regions of interest (ROIs) S, I, and N denotes signal, idler, and noise areas, respectively, where the noise ROI is used for simultaneous dark count monitoring.

the higher the threshold is, the lower is the quantum efficiency but the number of false detection events (i.e. noise) also.

Now, the list of positions of detection events is obtained. It however contains not only photon pairs, but broken pairs and noise events, too. This 'signal-to-noise' ratio can be in principle improved applying some a priori information about the coherence areas, in order to avoid such combinations, that can not be definitely correlated. However, if no a priori assumption is made, all possible combinations of detection events in signal and idler ROIs have to be taken into account. Each frame is therefore processed as follows: For both x and y coordinates of each detection from signal ROI, a respective x and y coordinate of all detection events from idler ROI is plotted with appropriate normalization as it is schematically depicted in the figure 5.5. The plots of each frames are afterwards accumulated into single image. This procedure can be for horizontal coordinates in transverse plane mathematically described with following formula

$$\Gamma_x(x_s, x_i) = \sum_{p=1}^{N} \sum_{m=1}^{M_p} \sum_{l=1}^{L_p} \delta(x_s^{(pm)} - x_s)\delta(x_i^{(pl)} - x_i), \tag{5.2}$$

where the first summation over p summarize results from all N frames and the second and third summations counts particular signal (m) and idler (l) detection events, up to M_p and L_p in p-th frame for signal and idler, respectively. For the vertical direction, the formula can be derived in the same manner[86,88]. The majority of the combinations however does not possess any correlations at all and they are therefore distributed uniformly across the plot surface creating a bias level. If sufficient number of frames (or detection events) is evaluated, the correlation pattern can be identified on top of homogeneous background if the 'signal-to-noise ratio' is sufficiently high.

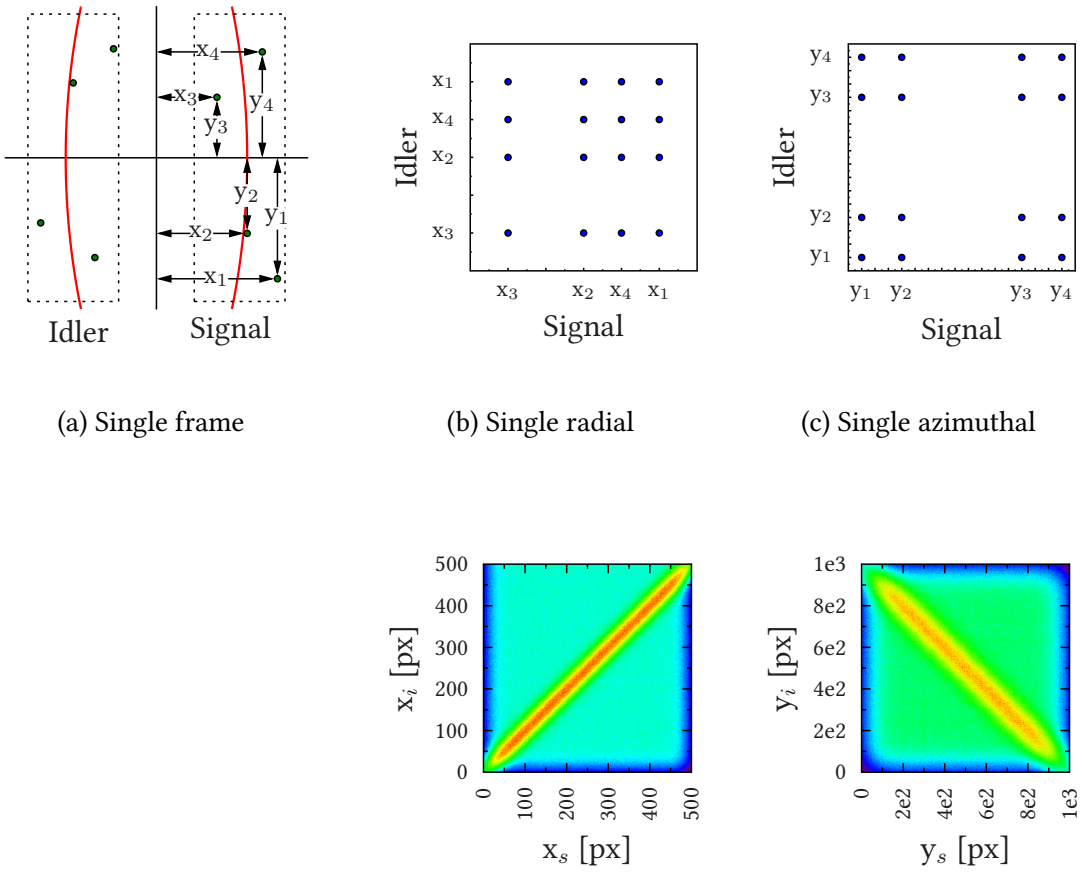

(a) Single frame (b) Single radial (c) Single azimuthal

(d) Accumulated radial (e) Accumulated azimuthal

Figure 5.5: Schematic illustration of simulation of image processing at single-photon level, where one million frames ($1000\times1000\,\mathrm{px}^2$), each with 50 detection events, were created with uncertainty of 25 px in radial and 75 px in azimuthal direction following Gaussian distribution. (a) the transverse plane of detection with individual detection events. (b) and (c) cross-correlation function Γ_{si} in radial and azimuthal direction for one particular frame (a), respectively. (d) and (e) resulting correlogram in radial and azimuthal direction, respectively as an accumulation of individual results (b) and (c), respectively.

The experimental results are plotted in the figure 5.6. On the left-hand side images, there are depicted cross-correlation functions in radial $\Gamma_{si,\xi}$ and azimuthal $\Gamma_{si,\phi}$ directions, respectively, where characteristic diagonal pattern can be easily identified. As a quantitative measure of size of the coherence area i.e. the width in corresponding direction, a slice $\Delta\Gamma$ through the correlation function Γ can be used. They are depicted on the right-hand side together with a Gaussian fit. From this fit the width (FWHM) of spatial correlation function can be obtained. Evaluated sizes of coherence areas in both radial and azimuthal directions were $\Delta\Gamma_\xi$ = $490 \pm 52\,\mu m$ and $\Delta\Gamma_\phi$ = $710 \pm 52\,\mu m$, respectively. From this results it can be seen, that the coherence area is elliptical with higher uncertainty in azimuthal direction.

Using processing technique presented here, the quantum detection efficiency can be easily determined from covariance of the signal and idler photon counts as well[104]. The values obtained for signal (8.5 %) and idler (7.2 %) differ due to non-unity reflectivity of used mirror and Fresnel reflection at the output face of the crystal and are both relatively low due to the non-optimal spectra with respect to sensitivity of the photocathode. It should be noted, that these values represent detection efficiency including losses of all components behind the crystal (e.g. transitivity of the interference filters).

5.4.2 High-Gain Regime

By increasing the power to 50 mW the high-gain regime with visible speckle pattern in generated field was reached (it can be obtained for pump power above 20 mW). Typical single shot readout image from the iCCD camera in this regime is displayed in the figure 5.7.

In this regime, when each pixel of camera detects high number of photons, the single-photon sensitivity is no longer necessary. Because of that, the MCP gain of the camera was reduced to prevent the sensor from saturating. Due to this possibility to tailor the sensitivity of the camera from single-photon level to classical regime with high number of detected photons, the identical detector could be used in both regimes with no need for realignment. The setup was therefore kept the same and only by rotating a single wave-plate and by changing the acquisition parameters of the camera it was possible to switch between these two regimes. This guaranteed that the results from both experiments would be consistent.

Even though the speckle sizes are larger than coherence areas, lower binning of 4×4 was used, since lower number of frames (typically 1000) is necessary for processing, and slower acquisition rate is therefore possible. Higher spatial resolution also resulted in smoother profiles. Finally, the measurements were taken under different experimental conditions with different pump powers and beam diameters.

The processing involved direct computation of auto and cross-correlation functions from measured data (after subtraction of the background consisted dominantly of thermal and readout noise of the CCD chip) according to formula (5.1), where each single shot frame provide a different ensemble of realizations for the statistical averaging. The correlation functions were however calculated only for 100 points, randomly selected in the fringe patterns close to the frequency degeneracy. This approach gives better results (signal-to-noise ratio) with respect to calculating correlation functions from the whole image, since only small parts of the frame are covered with light. These correlation functions were afterwards

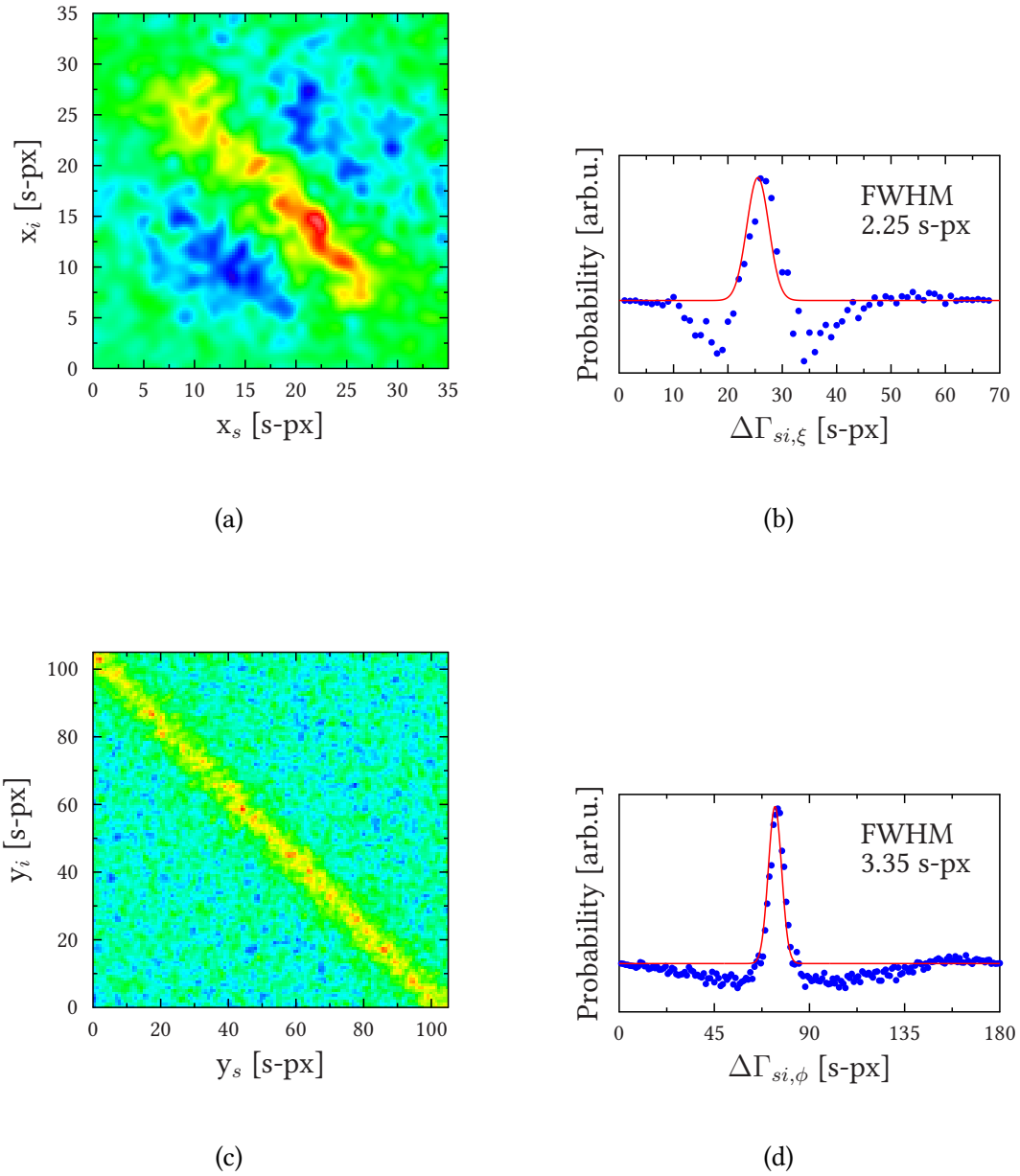

Figure 5.6: Results of measurement of coherence area in low-gain regime. Left-hand side images show accumulated results of single image processing revealing spatial correlations in radial (a) and azimuthal (c) directions as a diagonal feature. Right-hand side images represent cross section of the diagonal in perpendicular direction together with a Gaussian fit for both radial (b) and azimuthal (d) directions. FWHM of the Gaussian fit is considered as a width of the coherence area. Different orientation of the diagonal in comparison with figure 5.5 is caused by reflection on the mirror and can be corrected by appropriate transformation[88].

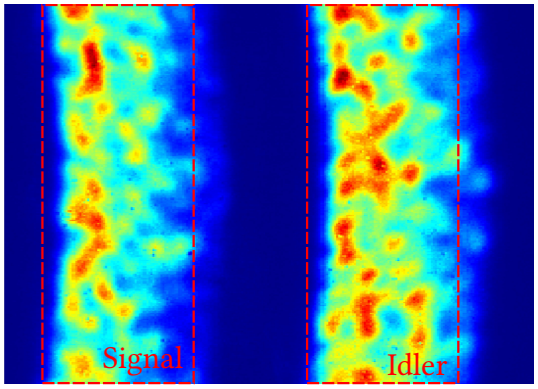

Figure 5.7: Single shot image from iCCD in high-gain regime ($P = 45\,\mathrm{mW}$) showing typical speckle pattern as a consequence of partial internal coherence in each of spatially and intensity correlated phase-conjugate modes.

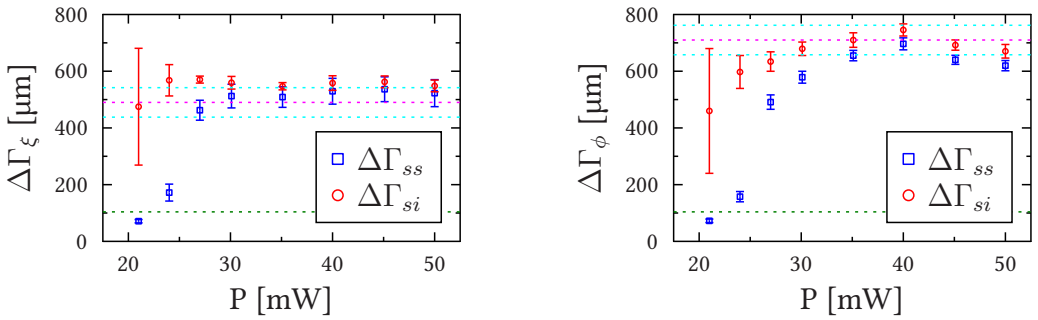

(a) Radial

(b) Azimuthal

Figure 5.8: Dependence of radial (a) and azimuthal (b) widths of auto and cross-correlation functions on pump power P. Upper dashed magenta lines represent width of cross-correlation functions measured in low-gain regime, cyan ones the standard deviation of that measurements. Bottom dashed green lines represent size of one super-pixel, thus showing a minimal width of correlation functions caused by the pixel structure of the detector.

quantitatively characterized by their horizontal (radial) and vertical (azimuthal) widths $\Delta\Gamma_x$ and $\Delta\Gamma_y$ ($\Delta\Gamma_\xi$ and $\Delta\Gamma_\phi$).

The results for the dependence of correlation function on the pump power are plotted in the figure 5.8. As can be seen, in region from 30 mW to 50 mW the widths of correlation functions, thus the sizes of individual speckles are relatively stable. Below this power the width of autocorrelation function drops down, while the width of cross-correlation function remains unchanged. This is due to the fact, that while the internal coherence of emitted fields originates from stimulated nonlinear process[105], the coherence between photons of twin beams arises from initial simultaneous creation. Therefore, if the pump field is not sufficiently intense, the probability of stimulated emission is reduced, resulting in lower internal

coherence, thus lower width of autocorrelation function. Below pump power level of 20 mW the width of autocorrelation function corresponds to dimension of the super-pixel, therefore representing only discrete pixel structure of the detector.

The second effect evident in the data in the figures 5.8 is systematically larger cross-correlation with respect to the autocorrelation. The explanation may be the fact, that although the camera was placed relatively far from the crystal (38.5 cm), it might still not be enough to reach exact far-field condition. This could be solved using Fourier lens in $2f$ configuration to perform Fourier transform of output fields and artificially moving the detector into the true far-field.

The most important is however the correspondence between width of intensity correlation function in high-gain regime and width of coherence area obtained at single-photon regime indicated in plots in the figures 5.8 with dashed magenta lines. This coincidence can be considered as an experimental evidence, that correlation function measured in both regimes represent the same physical phenomenon.

Next, the dependence of correlation function on pump beam diameter was investigated. Our experimental observation proved, that the radial profile of both autocorrelation and cross-correlation functions $\Delta\Gamma_\xi$ do not significantly depend on pump beam diameter. Nevertheless, in the azimuthal direction both correlation functions follow roughly hyperbolic dependence, as was expected. Since these results are consistent with theory developed for single-photon regime, it further links both regimes and serves as an additional confirmation, that coherence areas and speckles originates from the same nonlinear effect.

5.5 Summary

The very same experimental setup was used in order to demonstrate transition between low-gain regime characteristic by low number of photons per mode and high-gain regime, where the partial coherence macroscopic fields in each mode causes formation of typical speckle pattern. It was found, that the cross-correlation functions are in both regimes almost identical, since they both originate from the same non-linear phenomenon.

In contrast to the cross-correlation functions, which represent internal coherence between generated fields (signal and idler) and are given by spontaneous emission, the coherence in each field (signal or idler itself) represented by the autocorrelation function is caused by the stimulated process. Because of that the width of the autocorrelation functions drops down for low pump powers and is zero in low-gain regime.

Finally, the dependencies of intensity auto and cross-correlation functions on pump power and beam diameter in high-gain regime were investigated. It was found, that the dependencies follow behaviour expected from the theoretical model developed for single-photon level, confirming the correspondence between both regimes.

6

Luminescence of Nonlinear Materials

The non-parametric luminescence of BBO crystals will be studied in this chapter as a source of non-removable noise inevitably accompanying process of spontaneous parametric down-conversion. The problem of luminescence of nonlinear crystals will be addressed through time-resolved spectroscopy. Both spectral and temporal properties of generated field will be analysed in order to propose optimal strategy for potential filtering of the luminescence. By filtering out the luminescence, the signal-to-noise ratio in the experiment involving parametric down-conversion can be improved. Finally, the impact of luminescence noise on a single-photon source based on spontaneous parametric down-conversion will be estimated.

This research was highly motivated by our needs. Most of experiments performed in our laboratories use parametric down-conversion and the noise level is crucial for obtaining high quality results. This investigation was published in paper by Machulka *et al.* [106], where one can also find additional information.

6.1 Introduction

In previous chapters it was shown, that the process of parametric down-conversion (SPDC) in nonlinear media is well established source of optical fields correlated in many degrees of freedom.

Independently on the application, the success of any operation on correlated photons is achieved if and only if the two used photons originate from the same pair. This process however suffers from an inherent source of noise, the non-parametric luminescence of the medium itself, generated by the very same pump beam. Since both the SPDC and the luminescence are superimposed, it makes it complicated, if even possible, to separate

them from each other. Such non-removable noise will have consequently impact on quality of prepared single-photon state. In quantum cryptography, it can for instance lead even to security breach[90]. In quantum metrology, on the other hand, it can negatively influence the precision of the required measurement[107].

The scope of our study was to investigate spectral and temporal properties of luminescence, which can be afterwards used for effective filtering and also to roughly investigate its influence on typical single-photon source. As a nonlinear medium, β-BaB_2O_4 (BBO) crystals were used, since they are prominent material often used in nonlinear optics especially in UV region[108,109], where the problem with luminescence is dominant. Moreover, the BBO crystals are also frequently used to build second- and third-harmonics generators or parametric amplifiers, so the BBO induced luminescence may get to the experimental setup from the pumping laser system, even though no BBO crystal is used in the main setup.

This problem can be solved by shifting towards longer pump wavelengths, where as will be shown later the luminescence is no longer present. Nevertheless, in some situations the use of shorter pump wavelength is crucial as have been demonstrated several times[40,59]. One example of great importance of using pump in UV region is to reach maximum detection efficiency of detector at about 550 nm[110], which is among others important in quantum key distribution, where it guarantees security of the protocol[111,112].

Luminescence of BBO material has been already discussed in some papers[113–115]. These publications however focus on thermally stimulated luminescence[113,114] or impurities in BBO powders only[115].

6.2 Experiment

This section will contain information regarding the setup used for experimental characterization of the luminescence. Detailed description of a streak camera as a very fast detector will be given.

6.2.1 Experimental Setup

Used experimental setup is depicted in the figure 6.1. This setup was designed to simulate typical configuration used for common photon pairs generation, and therefore analyse the luminescence as it would contribute to the signal.

As a laser source, an optical parametric amplifier (OPA) pumped by amplified femtosecond Ti:Sapphire oscillator was used. The OPA generated pump beam with typical power about 100 mW, repetition rate 1 kHz, and pulse duration less than 150 fs with central wavelength ranging from 240 nm to 300 nm. Additional advantage in using OPA was presence of second beam at double wavelength (with respect to the output one) and the possibility to use it as a seed for stimulated generation, which significantly simplified the alignment.

At the beginning, the pump beam passed through neutral density filter (NDF) and half-wave plate (HWP) allowing to set required pump power and polarization. After that, beam impinged BBO crystal, where it induced both the SPDC and the luminescence. The BBO

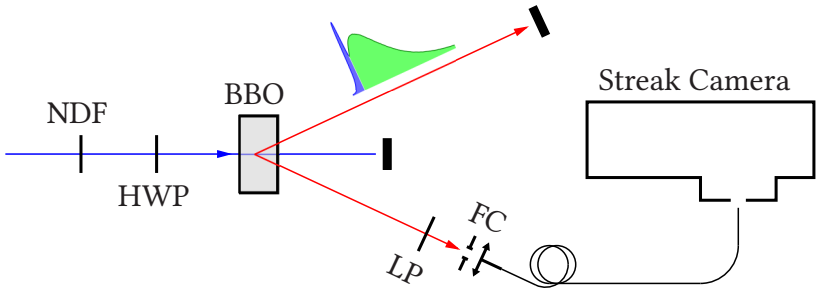

Figure 6.1: Sketch of the experimental setup for time-resolved spectroscopy. NDF: neutral density filter, HWP: half-wave plate, BBO: BBO crystal, LP: linear polarizer, FC: fiber coupler.

crystal was mounted on a rotation stage allowing for the crystal to be oriented in such a way, that spectrally-degenerate Type I component of SPDC was always emitted in the direction of a fixed fiber coupler. Here, the seeded generation was used to help with this alignment for different pump wavelengths. The fiber coupler was equipped with linear polarizer (LP) allowing for the polarization analysis of the signal to be performed. Finally, the collected light was sent to a detector via multi-mode optical fiber.

As a detector, two different devices were used. First, the signal was analysed with simple, but high sensitive grating spectrometer QE65Pro (Ocean Optics) and after alignment check and preliminary spectral analysis, the signal was analysed with a streak camera (Hamamatsu). The streak camera itself was equipped with Czerny-Turner spectrograph, where the signal was spectrally decomposed in horizontal direction, while in vertical direction, it was separated in time by the streak tube itself. Consequently, the image with spectral resolution in horizontal and time resolution in vertical axis was captured. Typical record of the signal from streak camera is depicted in the figure 6.2, where both parametric and non-parametric processes can be identified.

6.2.2 Streak Camera

Streak camera is apparatus capable of monitoring ultra-fast modulation of optical intensity up to hundreds of femtoseconds by transforming the time profile of the pulse into the spatial profile. As the CCD (as a final part of detection chain) is in general two dimensional detector, it provides simultaneous information about two different components, time and spatial profile (however only in one dimension) of the incident pump pulse. In our case the streak camera is equipped with monochromator, where the remaining spatial profile is transformed into the spectral profile, resulting in spectrometer with time resolution.

Essentially, the streak camera is very similar to the iCCD camera and in some sense it is also similar to a monochromator also. In default configuration it consists of a streak tube responsible for the time resolution and standard CCD chip (see figure 6.3 for schematic illustration). The light that impinges the camera through adjustable slit strikes the photocath-

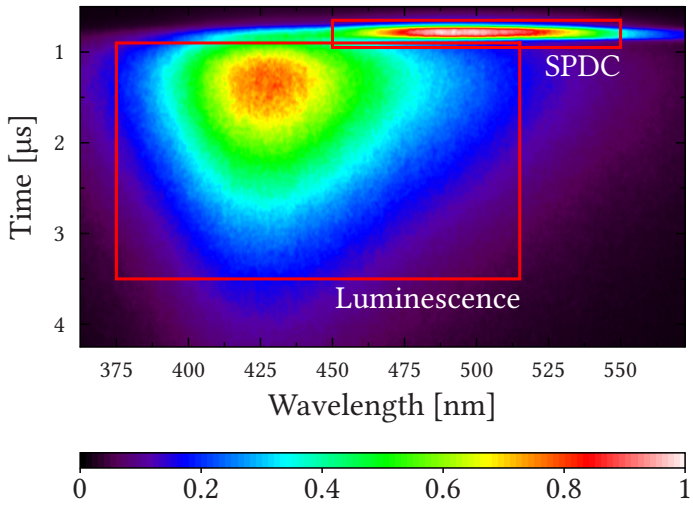

Figure 6.2: Typical readout image from streak camera in one particular time window (10 µs). Red rectangles represent regions of interest, where signal belonging to SPDC and luminescence, respectively can be identified.

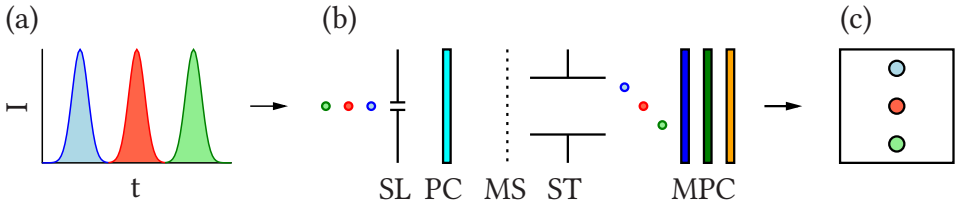

Figure 6.3: Schematic illustration of operation of the streak camera without monochromator. (a) Input pulse time profile. (b) Schematic sketch of the streak camera. SL: time slit, PC: photocathode, MS: accelerating mesh electrode, ST: streak tube, and MPC: micro-channel plate, phosphor screen, and CCD chip. (c) Final image on CCD chip, corresponding to input (a).

ode, which is responsible for the spectral sensitivity and quantum efficiency of the camera. The width of this slit determines the width of the instrument function, therefore the resolution of the streak camera in the time domain.

Emitted photo-electrons are accelerated through the streak tube with pair of large electrodes capable of generating variable electric field in direction perpendicular to the propagation of the photo-electrons. This electric field, if applied, deflects the electrons from linear direction, where the deflection depends on applied voltage. Since the voltage rumps up quickly after arrival of the optical pulse, the photo-electrons corresponding to the beginning of the optical pulse are deflected less than the ones corresponding to the pulse tail. The photo-electrons afterwards hit the phosphor screen, where they cause an optical flash,

which is detected by standard CCD chip. The stream of photo-electrons can be, as in our case, amplified by micro-channel plate (MCP) resulting in single-photon sensitivity.

6.3 Results

Using experimental apparatus described above, the spectral and temporal properties of light generated in the nonlinear crystal were obtained for various settings of pump polarization, power, and wavelength. Some measurements were performed also with different crystals. If not mentioned otherwise, the pump wavelength was set to 267 nm as a common wavelength in UV region (the fourth harmonic of Nd:YAG and the third harmonic of Ti:Sapphire laser) at a maximal power (about 100 mW) and used nonlinear crystal was $8\times8\times5$ mm^3 BBO crystal (Eksma) with cut angle 48°, with front surface oriented perpendicularly with respect to incident beam (emission angle about 4°).

6.3.1 Combined Measurements

This section will summarize spectral and time properties of both generated fields, the SPDC and the luminescence, while the later measurements will focus only on the luminescence.

Time-Integrated Spectral Profiles

At the beginning, the spectral profiles of both parametric and non-parametric processes were analysed with no time resolution using a simple grating spectrometer. The scope of this analysis was to identify spectral profiles belonging to each parametric and non-parametric processes, and thus find an optimal spectral setting for the streak camera for further measurements. The resulted spectral profiles are depicted in the figure 6.4. First, the pump polarization satisfying the phase-matching condition was used. In this configuration, a spectral profile with two features was observed with grating spectrometer. After that, the polarization was rotated using half-wave plate (HWP) so the phase-matching condition was no longer fulfilled. In this case, the peak corresponding to SPDC disappeared and only luminescence remained. Finally, the polarization was rotated back and linear polarizer (LP) was inserted in front of the fiber coupler (FC) to prevent linearly polarized SPDC signal from entering. Also in this case SPDC was filtered out, however the luminescence was reduced to only about a half, since its polarization is mixed. From this results it can be stated, that a significant spectral overlap exists between these two processes at this particular pump wavelength (267 nm).

Time-Resolved Measurements

Using streak camera, one can obtain time resolved spectral profiles as shown in the figure 6.2. The camera itself can operate in several time windows ranging from ms to ns, from which two (10 ns and 10 µs) were found the most suitable. In order to separate the SPDC and luminescence on the output image for processing, two region of interest (ROIs) were defined, as

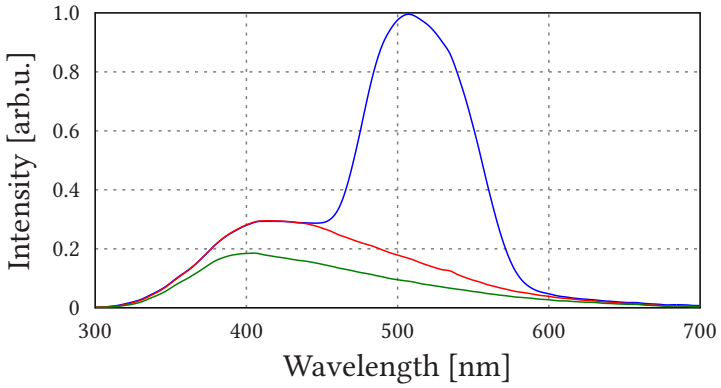

Figure 6.4: Combined time-integrated spectra measured with QE65Pro spectrometer under different experimental conditions: Both SPDC and luminescence signals (blue line), SPDC turned off by rotating the half-wave plate (red line), and SPDC is blocked from entering the coupler by linear polarizer (green line).

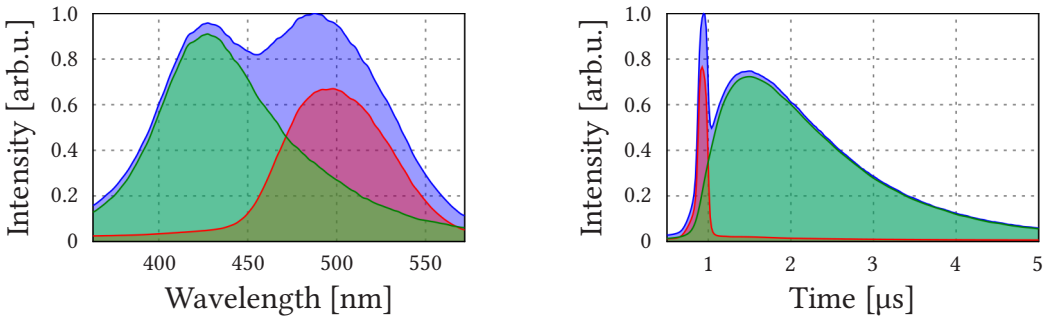

(a) Spectral profiles

(b) Temporal profiles

Figure 6.5: Spectral (a) and temporal (b) profiles of combined signal captured with streak camera in operate mode (as the one depicted in the figure 6.2). Data are obtained after appropriate integration over full image (blue curve), region of interest corresponding to SPDC signal (red line) and luminescence (green line).

schematically shown in the figure 6.2. Figure 6.5 displays spectral and temporal properties of separated as well as combined processes according to appropriate ROI.

6.3.2 Spectral Properties

During previous analysis, a spectral overlap between SPDC and luminescence at one particular wavelength was shown. To complete the analysis, the spectral profile of luminescence as it depends on pump wavelength and power was also investigated (see figure 6.6). Based on these results it can be stated, that spectral profiles of luminescence does not depend on nei-

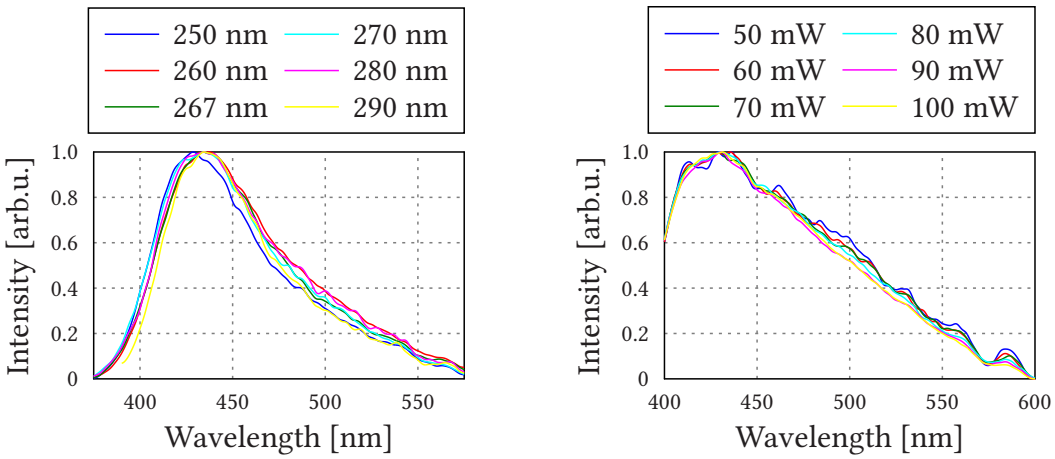

(a) (b)

Figure 6.6: Renormalized luminescence spectra as a function of pump wavelength (at maximal power of 100 mW) (a) and power (with pump wavelength 267 nm) (b).

ther the pump wavelength, nor the pomp power. Presented profiles have asymmetrical shape with maxima at about 430 nm. Since the SPDC (degenerate frequency) is emitted always at double wavelength with respect to the pump, it can be concluded, that in experimentally accessible spectral range from 240 nm to 290 nm, the luminescence will be always superimposed to the SPDC with maximal overlap at pump wavelength at approximately 215 nm.

From the perspective of luminescence and SPDC separation and thus noise reduction, there are two possibles strategies. The first one is to shift pump wavelength towards longer wavelengths until the spectral overlap is negligible. The second one is to use long pass edge or interference filter to cut off as much luminescence as possible. As the first option might not be optimal, if even accessible, from an experimental point of view (source and optical elements availability, detector quantum efficiency, etc.), the second one is usually widely used even though the luminescence can not be filtered completely and despite the fact, that each filter also introduce additional losses to the system due to its non-unitary transmittance.

It can be therefore concluded, that no spectral filtering in this region can be used to eliminate the luminescence as a noise for SPDC based single photon sources, as it can only reduce its intensity to some extent, while introducing a signal losses at the same time.

6.3.3 Temporal Properties

While the photons in parametric processes are emitted almost instantaneously as the pump pulse is propagating through the crystal, the non-parametric processes are typically delayed with long exponential decay. This difference is caused by the fact that in parametric process, the transition is described by electron transitions through the virtual energy levels, whereas

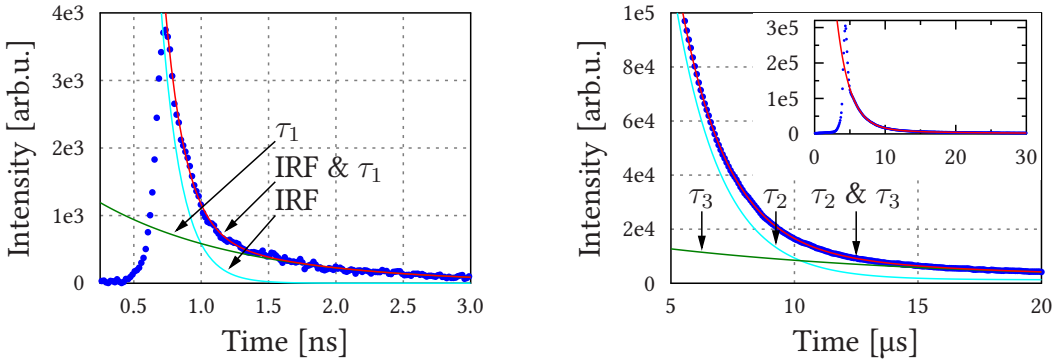

(a) Short decay

(b) Long decay

Figure 6.7: Exponential fit of data measured in short (a) and long (b) time window showing decay processes characterized by their time constants τ_1, τ_2, and τ_3 together with the instantaneous SPDC emission having the time duration of instrument response function (IRF).

in non-parametric processes the luminescence is product of electronic relaxation from excited real energy levels.

This effect of different decay times was already evident from time resolved measurements depicted in the figure 6.5, where sharp peak corresponding to the SPDC with width of instrument response function together with long time emission with characteristic exponential decay time can be identified. The typical exponential decay time is characterized by its time constant τ, a time period, in which the intensity falls to 1/e of its initial value. This constant can be obtained from experimental data by fitting the exponential function $I(t) = I_0 e^{-\tau t}$ on the data. In the case of multi-exponential decay, the fitting function gets form

$$I(t) = \sum I_0^{(i)} e^{-\tau_i t}. \tag{6.1}$$

Using two different time windows, three different processes with three different decay times were identified (see figure 6.7). The first decay process was observed having short decay time $\tau_1 = 0.73\,\text{ns}$, while others two have decay times in order of µs, $\tau_2 = 1.85\,\mu\text{s}$ and $\tau_3 = 9.95\,\mu\text{s}$, all obtained with relative error about 7 %.

As well as for the spectral profiles, also a time properties were analysed for different pump wavelengths and powers. From obtained results no dependence of time decay constants on pump wavelength or pump power was observed. As an example, the figures 6.8 and 6.9, show decay processes for decay time τ_2 as a function of pump wavelength and power, respectively.

Also here as well as in the case of spectral properties, an optimal strategy for noise reduction based on timing can be discussed. The signal is usually detected in a time interval called detection window. Using detection window short enough one may be able to sufficiently reduce the non-parametric processes. However, the detection windows are rarely shorter than units of ns, and therefore the fastest decay process with decay time τ_1 would not be

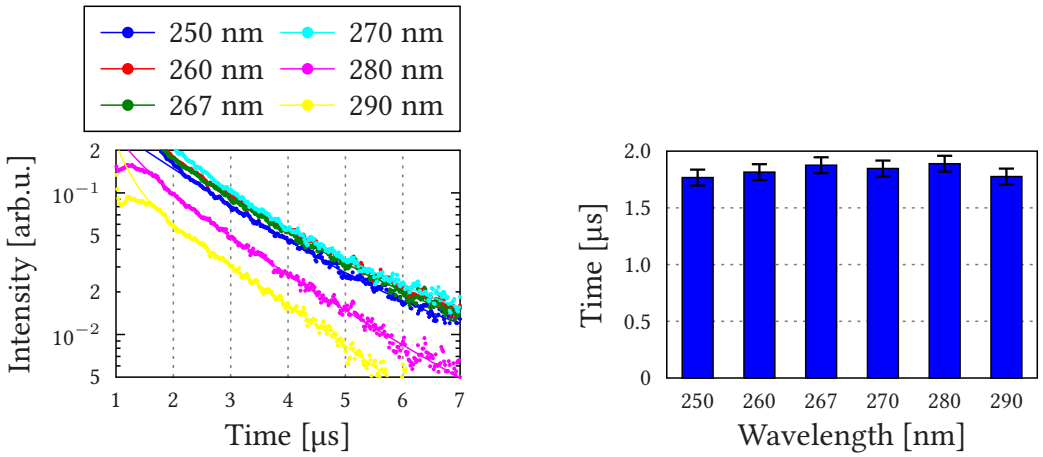

(a) (b)

Figure 6.8: Decay processes as a function of pump wavelength. Both exponential fits (a) and derived time constants (b) are presented. In figure (a) the dots represent acquired data, while the lines represent analytic exponential fit.

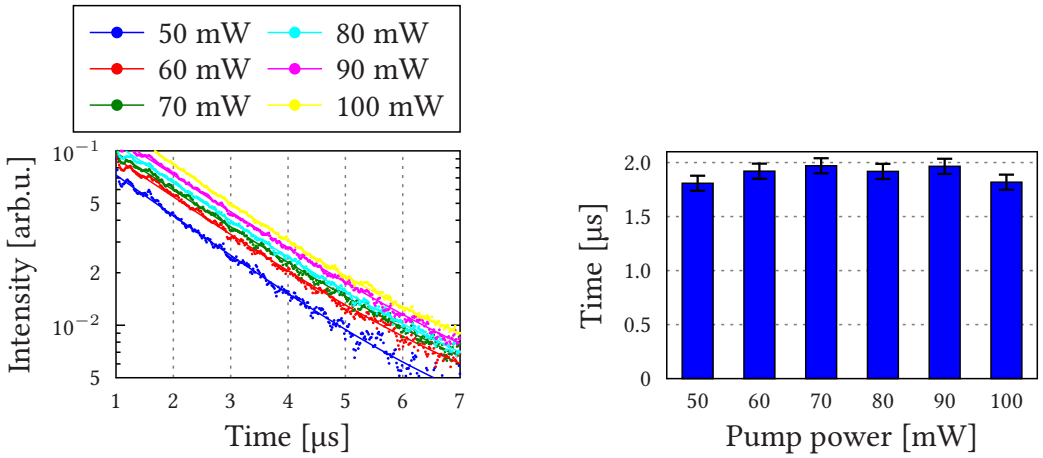

(a) (b)

Figure 6.9: Decay processes as a function of pump power. Both exponential fits (a) and derived time constants (b) are presented. In the figure (a) the dots represent acquired data, while the lines represent analytic exponential fit.

Eksma 48°	Eksma 50°	Caston 37°	Caston 48°
8×8×5 mm^3	8×8×5 mm^3	10×8×8 mm^3	8×8×6 mm^3
$\tau_2 = 1.71\,\mu s$	$\tau_2 = 1.88\,\mu s$	$\tau_2 = 1.06\,\mu s$	$\tau_2 = 1.09\,\mu s$

Table 6.1: Table of crystals used for purposes of presented study specified by their manufacturer, cut angle and dimensions (w×h×l) together with resulting decay time τ_2.

significantly affected. Other drawback of such gating is necessity to reduce repetition rate of the laser (not detection, but the laser itself) to allow the luminescence to extinguish before new detection window is opened. This would, if considering the longest decay process characterized with decay time τ_3, allows for the repetition rate of the experiment to be maximally about 100 kHz. Finally, this strategy is suitable for pulse laser sources only.

6.3.4 Different Crystals

So far the results obtained by measuring only one crystal were presented. It can be however suspected, that they may vary in some extent if different crystal would be used. To cover this issue, some of performed measurements were therefore repeated with different crystals of two manufacturers, Eksma and Caston. The results for all used crystals are listed in the table 6.1. As can be seen Eksma crystals possess a little bit longer decay times τ_2, which can be seen as a advantage from the perspective of time gating. Concerning the spectral properties, the results showed no significant differences.

6.3.5 Intensity Properties

Based on previous analysis it was stated, that neither spatial filtering nor time gating can be utilized in order to sufficiently reduce the luminescence induced noise from the SPDC signal, and thus a non-negligible amount of luminescence remains superimposed to the signal. In this section, the influence of such noise will be quantified using simple model of heralded single photon source based on SPDC[5,23,116,117].

Assuming an ideal heralded single photon source, the signal photon can be found in pure Fock state $|1\rangle\langle 1|$ every time, the heralding (idler) photon is detected. However, due to the presence of luminescence induced noise, the signal photon will be generated in a mixed state characterized by a density matrix $\hat{\rho}$

$$\hat{\rho} = \frac{1}{N}\left(p_0|0\rangle\langle 0| + p_1|1\rangle\langle 1| + p_2|2\rangle\langle 2|\right), \tag{6.2}$$

where $N = p_0 + p_1 + p_2$ represents the normalization factor. The first vacuum term $|0\rangle\langle 0|$ describes the situation, when a luminescence photon in idler mode is detected without being accompanied by any photon in signal mode, and thus causes a false heralding. The probability of this scenario can be expressed as $p_0 = p_l(1 - p_s)$, where p_l and p_s denotes probabilities of

Experimental condition		C_s	C_l	SNR	F
(i)	no filtering	2.225	1.343	1.657	0.624
(ii)	spectral filtering	2.176	0.489	4.450	0.820
(iii)	spectral & time filtering	2.077	0.024	86.572	0.989

Table 6.2: Measured values of SPDC and luminescence counts (in units of 10^{10}) under various spectral filtering and time gating. Resulting calculation of SNR and fidelity F is also presented.

generation luminescence and SPDC photons, respectively. The desired second term appears with success probability $p_1 = p_s(1-p_l)$. The last term $|2\rangle\langle 2|$ characterizes a situation, where both SPDC and luminescence photons being generated in signal mode simultaneously with probability $p_2 = p_s p_l$.

Let it be noted, that due to low conversion efficiency of SPDC the probability of more than one photon pair to be generated in one detection window was neglected. Also, since the luminescence photon rate is of the same order or lower than the generation rate of SPDC, the probability of simultaneous generation of two luminescence photons in a single detection window could thus be also neglected.

The quality of generated quantum state is usually expressed using the fidelity quantity F, which for our case takes a form

$$F = \frac{p_1}{p_0 + p_1 + p_2} = \frac{p_s(1-p_l)}{p_s(1-p_l) + p_l}. \tag{6.3}$$

As it was already demonstrated, the SPDC and luminescence intensity can be obtained separately via integrating over appropriate regions of interest. Doing so an SPDC-to-luminescence count ratio or signal-to-noise ratio SNR can be determined as

$$SNR = \frac{C_s}{C_l} = \frac{p_s}{p_l}, \tag{6.4}$$

where C_s and C_l denotes SPDC and luminescence counts, respectively. Using equation 6.4, the fidelity can be now expressed in term of SNR as

$$F = \frac{SNR - P_s}{SNR + 1 - P_s} \approx \frac{SNR}{SNR + 1}, \tag{6.5}$$

where the last approximation holds for low generation probabilities.

To calculate value of fidelity, three different scenarios were chosen: (i) no spectral filtering or time gating, (ii) spectral filtering only by a long-pass edge filter with cut-off edge at 460 nm, and (iii) both spectral filtering and time gating, where both spectral filtering and time gating were chosen to provide the best possible SNR. In all cases, an experimentally obtained SNR were used and values of fidelity were calculated according to formula (6.5). The results are summarized in the table 6.2. As can be seen, without any filtering the fidelity, and therefore the quality of single photon source is significantly reduced. Only when both spectral and temporal filtering were adopted, the fidelity approaches its theoretical limit $F = 1$. With spectral filtering alone, about half of this improvement can be achieved.

6.4 Summary

In this chapter, an experimental study of luminescence induced noise of nonlinear BBO crystals in SPDC-based single photon sources was presented. It was shown, that non-negligible spectral overlap exists between luminescence and SPDC signal for pump wavelength from region from 240 nm to 290 nm resulting in impossibility to spectrally separate the SPDC from the luminescence. It was also shown, that polarization projection can not be utilized neither in order to purify the source.

After that, a temporal characteristics of luminescence has been measured. It was found, that there exist fast (ns) and slow (μs) decay processes, whereas only the slow ones could be removed by typical time gating. Different behaviour of different crystals from different manufacturers was also studied.

The last section of this research was denoted to simple quantitative characterization of single photon source quality through its fidelity with desired state. It was shown, that only both spectral filtering together with time gating can remove the luminescence induced noise to the extent, where the fidelity reaches unity.

Conclusion

In this thesis, the second-order nonlinear phenomena have been studied. It was shown, that modern photonic devices based on guiding structures have a great potential as a future replacement of commonly used bulk crystals. This statement is justified due to their higher conversion efficiencies and possibility of monolithic integration into more complex photonic circuits. Generation of correlated photon pairs in bulk sources by parametric down-conversion was demonstrated experimentally several times in this thesis. These pairs were used to synthesize more complex entangled states, which were afterwords used to demonstrate non-classicality of these states. Another application of generated pairs was to study the connection between different intensity regimes, which can be eventually beneficial for future development in field of quantum communications.

The nonlinear phenomena were introduced in chapter 1, where the nonlinear wave equation was derived. This equation was afterwards used to derive coupled differential equations for two second-order nonlinear processes, the process of second-harmonic generation and spontaneous parametric down-conversion. Influence of phase-mismatch factor in obtained equations was thoroughly discussed and several approaches for its compensation were addressed. Finally, a real experimental techniques involving bulk crystals and waveguides were studied.

In chapter 2, the experimental characterization of second-harmonic generation in periodically-poled KTP waveguide was presented. It was experimentally demonstrated, that three different types of nonlinear interactions can be generated simultaneously utilizing different orders of periodic nonlinearity modulation. It was also shown, that due to broad spectrum of pulsed pump, the second-harmonic field is generated with rich spectral and spatial structure. However, the possibility to select only one particular interaction was also demonstrated. Further to that, the imperfection during the fabrication was considered. Analysed waveguide was in the end found to be a versatile source of second-order nonlinear precesses.

In the next chapter 3, a special type of quantum correlations, so-called quantum entanglement, was introduced. In the first theoretical part, Bell's like inequalities were discussed together with quantum tomography as an experimental tools to characterize particular state and distinguish, whether the state is classical or quantum. The second part was afterwords devoted to experimental generation and characterization of full set of maximally entangled Bell's states using Kwiat's source. Density matrices of generated states were then determined using polarization tomography and their quantumness was verified by violation of Bell's like CHSH inequality.

In chapter 4, generation of non-classical states in AlGaAs based Bragg reflection waveguide was studied. It was shown, that these structures posses many advantages with respect not only to common bulk crystals, but also to periodically-poled materials. The main advantages are extremely high nonlinearity leading to high conversion efficiency and therefore bright sources, and their great potential for further integration, which benefits from mature AlGaAs growth technologies. Even though the material is isotropic, a modal phase-matching between two different guided modes was demonstrated. After that, the quantumness of generated field was again verified by CHSH inequality violation.

Chapter 5 showed connection between different intensity regimes of parametric down-conversion generated in ordinary bulk BBO crystal. Here, the spatial correlations properties were studied in fields generated under two different conditions. First, the crystal was pumped by laser beam with such intensity, that generated fields consisted of individual photon pairs. In this case, the spatial correlations are demonstrated by existence of so-called correlation areas. Next, the pump power was increased to generate macroscopic fields, where the same phenomenon is manifested by creating typical speckle pattern. Using detector with very large dynamic range, the very same experimental setup was used in both cases. Since the cross-correlation functions in both regimes were found almost identical, it was proven, that they both originate from the same non-linear phenomenon. Also the dependencies of intensity autocorrelation and cross-correlation functions on pump power and beam diameter in high-gain regime were investigated. It was found, that these dependencies follow the behaviour expected from the theoretical model developed for single-photon level, which links both regimes even further.

In the next chapter 6, the experimental study of non-parametric process of luminescence induced noise of nonlinear BBO crystals was presented. Non-negligible spectral overlap with signal generated by parametric down-conversion was demonstrated at wavelengths typical for our experiments. After that, the temporal characteristics of the luminescence were measured, giving their typical time constants. Based on these measurements, an optimal strategy for filtering off the luminescence was discussed. It was shown, that due to fast decay, neither time gating, if available, is sufficient to remove this source of noise. Because of that, the influence of such noise on a simple single photon source based on parametric down-conversion was quantified. It was shown how different filtering strategies affect final fidelity with respect to the ideal single photon state.

Outlook

Regarding the future work, we will continue in experiments involving parametric down-conversion. The special attention will be given to spatial and spectral correlations of generated fields. We are especially interested in high intensity regime with typical speckle pattern. Currently, we are working on experiments exploring so-called x-waves as a product of spectral decomposition of generated fields by a dispersive element. We are also trying to reproduce some standard quantum-optical experiments with intense fields such as exploring quantum correlations of tripartite systems, for instance.

Conclusion in Czech

V této práci byly studovány nelineární jevy druhého řádu. Jak bylo ukázáno, moderní fotonické struktury mají velký potenciál nahradit běžně používané objemové krystaly. Toto tvrzení je podloženo jejich vyššími konverzními účinnostmi a možnostmi jejich integrace do složitějších optických obvodů. Byla zde několikrát experimentálně demonstrována generace korelovaných fotonových párů. Tyto páry byly následně použity pro syntézu složitějších entanglovaných stavů, jejichž neklasičnost byla rovněž experimentálně potvrzena. Generace korelovaných optických polí v procesu sestupné konverze v klasickém objemovém krystalu byla studována z pohledu souvislosti různých intenzitních režimů.

Základní úvod do nelineární optiky, zejména do nelineárních jevů druhého řádu, byl obsahem kapitoly 1. Z nelineární vlnové rovnice byly odvozeny vázané diferenciální rovnice popisující vývoj interagujících polí pro procesy generace druhé harmonické a parametrické sestupné frekvenční konverze. Na těchto příkladech byl demonstrován vliv fázového faktoru, na účinnosti těchto procesů. Dále byla ukázána některá řešení, jak tento fázový člen minimalizovat a tím docílit fázového sladění. Následně byly prezentovány vlastní experimenty pro generaci nelineárních jevů s využitím jak objemových krystalů, tak vlnovodných struktur.

Kapitola 2 obsahovala experimentální charakterizaci periodicky pólovaného vlnovodu promocí procesu generace druhé harmonické frekvence. Bylo experimentálně ukázáno, že takováto struktura může díky vyšším harmonickým frekvencím periodického pólovaní generovat všechny tři kombinace interagujících polarizací. Dále bylo ukázáno, že díky širokému spektru pulzního čerpacího pole bylo možné generovat celou škálu jednotlivých procesů lišících se jak spektrálními, tak módovými profily interagujících polí. Nicméně bylo demonstrováno, že vhodnou filtrací je možné tyto procesy izolovat. Na závěr byl rovněž diskutován vliv nedokonalostí výrobního procesu na vlastnosti generovaných polí. Celkově bylo ukázáno, že periodicky pólované vlnovody jsou vhodným zdrojem nelineárních procesů nejen díky jejich vysoké konverzní účinnosti, ale i značné univerzálnosti.

Kapitola 3 se věnovala entanglementu jako specifickému typu kvantových korelací. První část byla věnována teoretickému rozboru. Dále byly zavedeny Bellovy nerovnosti, které lze použít jako kritérium neklasičnosti, tj. rozlišení, nalézá-li se zkoumaný systém v klasickém či kvantovém stavu. Mimo to byla prezentována metoda kvantové tomografie založená na metodě maximální věrohodnosti jakožto experimentální nástroj pro kompletní analýzu studovaného stavu. Druhá část byla věnována vlastnímu experimentu věnujícímu se generaci kompletní sady Bellových stavů jakožto maximálně entanglovaných dvojfotonových stavů světla. Pro jejich generaci by využit Kwiatův zdroj. Pomocí polarizační kvantové tomografie byly získány matice hustoty generovaných stavů, jejichž neklasičnost byla experimentálně demonstrována porušením Bellových nerovností.

Generace neklasických stavů světla byla obsahem i následující kapitoly 4. Zde byl však použit tzv. Braggův vlnovod. Nejdříve byl studován prostorový profil vedeného módu a diskutovány hlavní výhody takovýchto struktur z nichž nejdůležitější je vysoká konverzní účinnost a značný potenciál pro integraci do monolitických optických čipů, zejména díky pokročilým výrobním technologiím. Dále byl prezentován způsob fázového sladění v takovýchto izotropních polovodičových materiálech založený na interakci různých vedených módů. Nakonec byla demonstrována jejich schopnost generovat neklasické stavy světla, což bylo ověřeno opět pomocí porušení Bellových nerovností.

Kapitola 5 popisuje spojitost mezi různými intenzitními režimy sestupné parametrické konverze generované v klasických objemových BBO krystalech. Konkrétně byly studovány prostorové korelace generovaných polí v režimu nízkého a vysokého zisku, tj. pro slabé a silné čerpání. V prvním režimu slabého čerpání byla generovaná pole tvořena jednotlivými fotony, zatímco v druhém silným makroskopickým polem s typickou strukturou koherenční zrnitosti. Díky detektoru s vysokým dynamický rozsahem bylo možné v obou režimech použít totéž experimentální uspořádání. Fakt, že vzájemné korelační funkce jsou v obou režimech prakticky totožné lze brát jako potvrzení toho, že chování v obou režimech je řízeno stejným nelineárním procesem. Dále bylo zkoumáno chování korelačních funkcí v závislosti na parametrech čerpacího svazku. Vzhledem k tomu, že i tyto závislosti kopírovaly předpovědi učiněné pro režim nízkého zisku, lze i to chápat jako další potvrzení souvislosti mezi jednotlivými režimy.

Následující kapitola 6 byla věnována neparametrické luminiscenci, jakožto zdroji neodstranitelného šumu doprovázejícího sestupnou parametrickou konverzi. Na námi typicky používaných vlnových délkách byl ukázán nezanedbatelný spektrální překryv obou procesů. Studiem časových charakteristik luminiscence bylo následně ukázáno, že ani pomocí detekce v časově omezených oknech není možné tento šum zcela odstranit. Na základě získaných výsledků pak byla diskutována optimální strategie pro maximální odstínění tohoto parazitního jevu. Vzhledem k tomu, že luminiscenci lze odstínit jen částečně, byl vytvořen jednoduchý model pro kvantitativní analýzu vlivu takového šumu na přesnost generace jednofotonových stavů.

List of Author's Publications

The First Author

- R. Machulka, J. Svozilík, J. Soubusta, J. Peřina, Jr., and O. Haderka: *"Spatial and spectral properties of fields generated by pulsed second-harmonic generation in a periodically poled potassiumtitanyl-phosphate waveguide"*. Physical Review A **87**, 013836 (2013).
- R. Machulka, J. Svozilík, J. Soubusta, J. Peřina, Jr., and O. Haderka: *"Spatial and spectral properties of second harmonic generation in a periodically poled KTP waveguide"* in *"Wave and Quantum Aspects of Contemporary Optics"*. Proceedings of SPIE **8697**, 86972 (2013).
- R. Machulka, O. Haderka, J. Peřina, Jr., M. Lamperti, A. Allevi, and M. Bondani: *"Spatial properties of twin-beam correlations at low- to high-intensity transition"*. Optics Express **22**, 11, 13374–13379 (2014).
- R. Machulka, K. Lemr, O. Haderka, M. Lamperti, A. Allevi, and M. Bondani: *"Luminescence-induced noise in single photon sources based on BBO crystals"*. Journal of Physics B: Atomic Molecular and Optical Physics **47**, 21, 215501 (2014).

Co-Author

- F. Sciarrino, G. Vallone, G. Milani, A. Avela, J. Galinis, **R. Machulka**, A.M. Perego, K.Y. Spasibko, A. Allevi, and M. Bondani: *"High degree of entanglement and nonlocality of a two photon state generated at* 532 nm*"*. European Physics Journal: Special Topics **199**, 1, 111–125 (2011).
- A. Valles, M. Hendrych, J. Svozilík, **R. Machulka**, P. Abolghasem, D. Kang, B.J. Bijlani, A.S. Helmy, and J.P. Torres: *"Generation of polarization-entangled photon pairs in Bragg reflection waveguide"*. Optics Express **21**, 9, 10841–10849 (2013).
- A. Allevi, M. Lamperti, M. Bondani, J. Peřina, Jr., V. Michálek, O. Haderka, and **R. Machulka**: *"Characterizing the nonclassicality of mesoscopic optical twin-beam states"*. Physical Review A **88**, 6, 063807 (2013).
- M. Lamperti, A. Allevi, M. Bondani, **R. Machulka**, V. Michálek, O. Haderka, and J. Peřina, Jr: *"Optimal sub-Poissonian light generation from twin beams by photon-number resolving detectors"*. Journal of the Optical Society of America B: Optical Physics **31**, 1, 20–25 (2014).

- M. Lamperti, A. Allevi, M. Bondani, **R. Machulka**, V. Michálek, O. Haderka, and J. Peřina, Jr.: *"Generation of sub-Poissonian non-Gaussian states from multimode twin beams by photon-number-resolving detectors"*. International Journal of Quantum Information **12**, 1461017 (2014).
- A. Allevi, M. Lamperti, O. Jedrkiewicz, J. Galinis, **R. Machulka**, O. Haderka, J. Peřina, Jr., and M. Bondani: *"Spatio-spectral characterization of twin-beam states of light for quantum state engineering"*. International Journal of Quantum Information **12**, 7, 1560027 (2015).

References

1. R. W. Boyd: "*Nonlinear optics*" (Elsevier Science, 2008).
2. R. W. Boyd: "*Topical review: Order-of-magnitude estimates of the nonlinear optical susceptibility*". Journal of Modern Optics **46,** 367–378 (1999).
3. P. A. Franken, A. E. Hill, C. W. Peters, and G. Weinreich: "*Generation of optical harmonics*". Physical Review Letters **7,** 118–119 (1961).
4. D. A. Kleinman: "*Nonlinear dielectric polarization in optical media*". Physical Review **126,** 1977–1979 (1962).
5. D. C. Burnham, and D. L. Weinberg: "*Observation of simultaneity in parametric production of optical photon pairs*". Physical Review Letters **25,** 84–87 (1970).
6. P. Malý: "*Optika*" (Karolinum, 2008).
7. A. Yariv, and P. Yeh: "*Optical waves in crystals: Propagation and control of laser radiation*" (Wiley, 2002).
8. J. A. Armstrong, N. Bloembergen, J. Ducuing, and P. S. Pershan: "*Interactions between light waves in a nonlinear dielectric*". Physical Review **127,** 1918–1939 (1962).
9. T. H. Maiman: "*Stimulated optical radiation in ruby*". Nature **187,** 493–494 (1960).
10. K. Moutzouris, S. V. Rao, M. Ebrahimzadeh, A. D. Rossi, M. Calligaro, V. Ortiz, and V. Berger: "*Second-harmonic generation through optimized modal phase matching in semiconductor waveguides*". Applied Physics Letters **83,** 620–622 (2003).
11. R. L. Sutherland: "*Handbook of nonlinear optics*" (Taylor & Francis, 2003).
12. K. Chikuma, and S. Umegaki: "*Characteristics of optical second harmonic generation due to Čerenkov radiation type phasematching*". Journal of Optical Society of America B **7,** 768–775 (1990).
13. M. J. Li, M. de Micheli, Q. He, and D. B. Ostrowsky: "*Čerenkov configuration second harmonic generation in proton-exchanged lithium niobate guides*". IEEE Journal of Quantum Electronics **26,** 1384–1393 (1990).
14. O. Sugihara, S. Kunioka, Y. Nonaka, R. Aizawa, Y. Koike, T. Kinoshita, and K. Sasaki: "*Second-harmonic generation by Cerenkov-type phase matching in a poled polymer waveguide*". Journal of Applied Physics **70,** 7249–7252 (1991).
15. V. Vaičaitis: "*Cherenkov-type phase matching in bulk KDP crystal*". Optics Communications **209,** 485–490 (2002).

16. G. D. Boyd, and D. A. Kleinman: "*Parametric interaction of focused gaussian light beams*". Journal of Applied Physics **39,** 3597–3639 (1968).

17. C. Yeh, and F. Shimabukuro: "*The essence of dielectric waveguides*" (Springer, 2008).

18. R. Machulka, J. Svozilík, J. Soubusta, J. Jan Peřina, and O. Haderka: "*Spatial and spectral properties of fields generated by pulsed second-harmonic generation in a periodically poled potassium-titanyl-phosphate waveguide*". Physical Review A **87,** 013836–9 (2013).

19. M. M. Fejer, G. A. Magel, D. H. Jundt, and R. L. Byer: "*Quasi-phase-matched second harmonic generation: tuning and tolerances*". IEEE Journal of Quantum Electronics **28,** 2631–2654 (1992).

20. M. M. Fejer, G. A. Magel, and E. J. Lim: "*Quasi-phase-matched interactions in lithium niobate*". in *Proceedings SPIE: Nonlinear optical properties of materials* (eds H. R. Schlossberg, and R. V. Wick) **1148** (1989), 213–224.

21. M. Yamada, N. Nada, M. Saitoh, and K. Watanabe: "*First-order quasi-phase matched $LiNbO_3$ waveguide periodically poled by applying an external field for efficient blue second-harmonic generation*". Applied Physics Letters **62,** 435–436 (1993).

22. N. E. Yu, S. Kurimura, and K. Kitamura: "*Higher-order quasi-phase matched second harmonic generation in periodically poled MgO-doped stoichiometric $LiTaO_3$*". Journal of Korean Physical Society **47,** 636–639 (2005).

23. J. Chen, A. J. Pearlman, A. Ling, J. Fan, and A. L. Migdall: "*A versatile waveguide source of photon pairs for chip-scale quantum information processing*". Optics Express **17,** 6727–6740 (2009).

24. M. G. Roelofs, A. Suna, W. Bindloss, and J. D. Bierlein: "*Characterization of optical waveguides in $KTiOPO_4$ by second harmonic spectroscopy*". Journal of Applied Physics **76,** 4999–5006 (1994).

25. C. M. Kaleva, M. Munro, T. D. Roberts, T. Chang, and P. Battle: "*Type II sum frequency generation in KTP waveguides: a technique for pre and post screening*". in *Proceedings SPIE: Nonlinear frequency generation and conversion: Materials,devices,and applications VII* (ed P. E. Powers) **6875** (2008), 68751–8.

26. A. Christ, K. Laiho, A. Eckstein, T. Lauckner, P. J. Mosley, and C. Silberhorn: "*Spatial modes in waveguided parametric down-conversion*". Physical Review A **80,** 033829–7 (2009).

27. M. Karpinski, C. Radzewicz, and K. Banaszek: "*Experimental characterization of three-wave mixing in a multimode nonlinear $KTiOPO_4$ waveguide*". Applied Physics Letters **94** (2009).

28. P. J. Mosley, A. Christ, A. Eckstein, and C. Silberhorn: "*Direct measurement of the spatial-spectral structure of waveguided parametric down-conversion*". Physical Review Letters **103,** 233901–4 (2009).

29. K. Banaszek, A. B. U'Ren, and I. A. Walmsley: "*Generation of correlated photons in controlled spatial modes by downconversion in nonlinear waveguides*". Optics Letters **26,** 1367–1369 (2001).

30. L. Mandel, and E. Wolf: "*Optical coherence and quantum optics*" (Cambridge University Press, 1995).

31. A. W. Snyder, and J. Love: "*Optical waveguide theory*" (Springer, 1983).

32. J. D. Bierlein, A. Ferretti, L. H. Brixner, and W. Y. Hsu: "*Fabrication and characterization of optical waveguides in $KTiOPO_4$*". Applied Physics Letters **50,** 1216–1218 (1987).

33. T. Y. Fan, C. E. Huang, B. Q. Hu, R. C. Eckardt, Y. X. Fan, R. L. Byer, and R. S. Feigelson: "*Second harmonic generation and accurate index of refraction measurements in flux-grown $KTiOPO_4$*". Applied Optics **26,** 2390–2394 (1987).

34. K. Kawano, and T. Kitoh: "*Introduction to optical waveguide analysis: Solving Maxwell's equation and the Schrödinger equation*" (Wiley, 2004).

35. I. Rubinstein, and L. Rubinstein: "*Partial differential equations in classical mathematical physics*" (Cambridge University Press, 1998).

36. J. Jin: "*The finite element method in electromagnetics*" (John Wiley & Sons Canada,Limited, 2003).

37. A. B. Fallahkhair, K. S. Li, and T. E. Murphy: "*Vector finite difference modesolver for anisotropic dielectric waveguides*". Journal of Lightwave Technology **26,** 1423–1431 (2008).

38. N.-E. Yu, J.-H. Ro, H.-K. Kim, M. Cha, I. Hatanaka, K. Nakamura, and H. Ito: "*High order quasi-phase-matched second harmonic generations in periodically poled lithium niobate*". Journal of Korean Physical Society **35,** 1384–1386 (1999).

39. M. F. Saleh, B. E. A. Saleh, and M. C. Teich: "*Modal,spectral,and polarization entanglement in guided-wave parametric down-conversion*". Physical Review A **79,** 053842–10 (2009).

40. F. Sciarrino, G. Vallone, G. Milani, A. Avella, J. Galinis, R. Machulka, A. M. Perego, K. Y. Spasibko, A. Allevi, M. Bondani, and P. Mataloni: "*High degree of entanglement and nonlocality of a two-photon state generated at 532 nm*". The European Physical Journal **199.** *Special Topics,* 111–125 (2011).

41. M. A. Nielsen, and I. L. Chuang: "*Quantum information and quantum computation*" (Cambridge University Press, 2011).

42. H. J. Briegel, and R. Raussendorf: "*Persistent entanglement in arrays of interacting particles*". Physical Review Letters **86,** 910–913 (2001).

43. J. I. Cirac, A. K. Ekert, S. F. Huelga, and C. Macchiavello: "*Distributed quantum computation over noisy channels*". Physical Review A **59,** 4249–4254 (1999).

44. D. Bouwmeester, A. K. Ekert, and A. Zeilinger: "*The physics of quantum information: quantum cryptography,quantum teleportation,quantum computation*" (Springer Publishing Company, 2010).

45. V. Giovannetti, S. Lloyd, and L. Maccone: "*Advances in quantum metrology*". Nature Photonics **5,** 222–229 (2011).

46. T. B. Pittman, Y. H. Shih, D. V. Strekalov, and A. V. Sergienko: "*Optical imaging by means of two-photon quantum entanglement*". Physical Review A **52,** 3429–3432 (1995).

47. M. I. Kolobov: "*Quantum Imaging*" (Springer New York, 2007).

48. E. Nagali, F. Sciarrino, F. D. Martini, L. Marrucci, B. Piccirillo, E. Karimi, and E. Santamato: "*Quantum information transfer from spin to orbital angular momentum of photons*". Physical Review Letters **103,** 013601–4 (2009).

49. A. Migdall: "*Polarization directions of noncollinear phase-matched optical parametric downconversion output*". Journal of the Optical Society of America B **14,** 1093–1098 (1997).

50. A. Einstein, B. Podolsky, and N. Rosen: "*Can quantum-mechanical description of physical reality be considered complete?*" Physical Review **47,** 777–780 (1935).

51. J. S. Bell: "*On the Einstein-Podolsky-Rosen paradox*". Physics **1,** 195–200 (1964).

52. J. F. Clauser, M. A. Horne, A. Shimony, and R. A. Holt: "*Proposed experiment to test local hidden-variable theories*". Physical Review Letters **23,** 880–884 (1969).

53. M. Genovese: "*Research on hidden variable theories: A review of recent progresses*". Physics Reports **413,** 319–396 (2005).

54. M. Dušek: "*Koncepční otázky kvantové teorie*" (Univerzita Palackého, 2002).

55. W. H. Zurek: "*Decoherence and the transition from quantum to classical*". Physics Today **44,** 36–44 (1991).

56. D. F. V. James, P. G. Kwiat, W. J. Munro, and A. G. White: "*Measurement of qubits*". Physical Review A **64,** 052312–15 (2001).

57. N. K. Langford, T. J. Weinhold, R. Prevedel, K. J. Resch, A. Gilchrist, J. L. O'Brien, G. J. Pryde, and A. G. White: "*Demonstration of a simple entangling optical gate and its use in Bell-state analysis*". Physical Review Letters **95,** 210504–4 (2005).

58. J. Řeháček, Z. Hradil, and M. Ježek: "*Iterative algorithm for reconstruction of entangled states*". Physical Review A **63,** 040303–4 (2001).

59. Y. Nambu, K. Usami, Y. Tsuda, K. Matsumoto, and K. Nakamura: "*Generation of polarization-entangled photon pairs in a cascade of two type-I crystals pumped by femtosecond pulses*". Physical Review A **66,** 033816–10 (2002).

60. P. G. Kwiat, K. Mattle, H. Weinfurter, A. Zeilinger, A. V. Sergienko, and Y. Shih: "*New high-intensity source of polarization-entangled photon pairs*". Physical Review Letters **75,** 4337–4341 (1995).

61. V. G. Dmitriev, G. G. Gurzadyan, and D. N. Nikogosyan: "*Handbook of nonlinear optical crystals*" (Springer,Berlin, 1991).

62. P. G. Kwiat, E. Waks, A. G. White, I. Appelbaum, and P. H. Eberhard: "*Ultrabright source of polarization-entangled photons*". Physical Review A **60,** 773–776 (1999).

63. C. H. Monken, P. H. R. Souto, and S. Pádua: "*Transfer of angular spectrum and image formation in spontaneous parametric down-conversion*". Physical Review A **57,** 3123–3126 (1998).

64. T.-C. Wei, K. Nemoto, P. M. Goldbart, P. G. Kwiat, W. J. Munro, and F. Verstraete: "*Maximal entanglement versus entropy for mixed quantum states*". Physical Review A **67,** 022110–12 (2003).

65. A. Vallés, M. Hendrych, J. Svozilík, R. Machulka, P. Abolghasem, D. Kang, B. J. Bijlani, A. S. Helmy, and J. P. Torres: "*Generation of polarization-entangled photon pairs in a Bragg reflection waveguide*". Optics Express **21,** 10841–10849 (2013).

66. I. Shoji, T. Kondo, A. Kitamoto, M. Shirane, and R. Ito: "*Absolute scale of second-order nonlinear-optical coefficients*". Journal of the Optical Society of America B **14,** 2268–2294 (1997).

67. B. J. Bijlani, and A. S. Helmy: "*Bragg reflection waveguide diode lasers*". Optics Letters **34,** 3734–3736 (2009).

68. J. S. Aitchison, M. W. Street, N. D. Whitbread, D. C. Hutchings, J. H. Marsh, G. T. Kennedy, and W. Sibbett: "*Modulation of the second-order nonlinear tensor components in multiple-quantum-well structures*". IEEE Journal of Selected Topics in Quantum Electronics **4,** 695–700 (1998).

69. A. Fiore, V. Berger, E. Rosencher, P. Bravetti, and J. Nagle: "*Phase matching using an isotropic nonlinear optical material*". Nature **391,** 463–466 (1998).

70. C. B. Ebert, L. A. Eyres, M. M. Fejer, and J. James S. Harris: "*MBE growth of antiphase GaAs films using GaAs/Ge/GaAs heteroepitaxy*". Journal of Crystal Growth **201-202,** 187–193 (1999).

71. A. S. Helmy, D. C. Hutchings, T. C. Kleckner, J. H. Marsh, A. C. Bryce, J. M. Arnold, C. R. Stanley, J. S. Aitchison, C. T. A. Brown, K. Moutzouris, *et al.:* "*Quasi phase matching in GaAs–AlAs superlattice waveguides through bandgap tuning by use of quantum-well intermixing*". Optics Letters **25,** 1370–1372 (2000).

72. R. Haidar, N. Forget, and E. Rosencher: "*Optical parametric oscillation in microcavities based on isotropic semiconductors: a theoretical study*". IEEE Journal of Quantum Electronics **39,** 569–576 (2003).

73. D. Faccio, F. Bragheri, and M. Cherchi: "*Optical Bloch-mode-induced quasi phase matching of quadratic interactions in one-dimensional photonic crystals*". Journal of the Optical Society of America B **21,** 296–301 (2004).

74. A. S. Helmy, B. Bijlani, and P. Abolghasem: "*Phase matching in monolithic Bragg reflection waveguides*". Optics Letters **32,** 2399–2401 (2007).

75. P. Abolghasem, J. Han, B. J. Bijlani, A. Arjmand, and A. S. Helmy: "*Continuous-wave second harmonic generation in Bragg reflection waveguides*". Optics Express **17,** 9460–9467 (2009).

76. J.-B. Han, P. Abolghasem, D. Kang, B. J. Bijlani, and A. S. Helmy: "*Difference-frequency generation in AlGaAs Bragg reflection waveguides*". Optics Letters **35,** 2334–2336 (2010).

77. R. Horn, P. Abolghasem, B. J. Bijlani, D. Kang, A. S. Helmy, and G. Weihs: "*Monolithic source of photon pairs*". Physical Review Letters **108,** 153605–5 (2012).

78. B. R. West, and A. S. Helmy: "*Properties of the quarter-wave Bragg reflection waveguide: theory*". Journal of the Optical Society of America B **23,** 1207–1220 (2006).

79. P. Abolghasem, J.-B. Han, D. Kang, B. J. Bijlani, and A. S. Helmy: "*Monolithic photonics using second-order optical nonlinearities in multilayer-core Bragg reflection waveguides*". IEEE Journal of Selected Topics in Quantum Electronics **18,** 812–825 (2012).

80. P. Yeh, and A. Yariv: "*Bragg reflection waveguides*". Optics Communications **19,** 427–430 (1976).

81. A. S. Helmy: "*Phase matching using Bragg reflection waveguides for monolithic nonlinear optics applications*". Optics Express **14,** 1243–1252 (2006).

82. P. Abolghasem, J. Han, B. J. Bijlani, A. Arjmand, and A. S. Helmy: "*Highly efficient second-harmonic generation in monolithic matching layer enhanced AlGaAs Bragg reflection waveguides*". IEEE Photonics Technology Letters **21,** 1462–1464 (2009).

83. N. Gisin: "*Bell's inequality holds for all non-product states*". Physics Letters A **154,** 201–202 (1991).

84. S. V. Zhukovsky, L. G. Helt, D. Kang, P. Abolghasem, A. S. Helmy, and J. E. Sipe: "*Generation of maximally-polarization-entangled photons on a chip*". Physical Review A **85,** 013838–6 (2012).

85. R. Machulka, O. Haderka, J. Jan Peřina, M. Lamperti, A. Allevi, and M. Bondani: "*Spatial properties of twin-beam correlations at low-to high-intensity transition*". Optics Express **22,** 13374–13379 (2014).

86. M. Hamar, J. Peřina, O. Haderka, and V. Michálek: "*Transverse coherence of photon pairs generated in spontaneous parametric down-conversion*". Physical Review A **81,** 043827–10 (2010).

87. O. Haderka, J. Jan Peřina, M. Hamar, and J. Peřina: "*Direct measurement and reconstruction of nonclassical features of twin beams generated in spontaneous parametric down-conversion*". Physical Review A **71,** 033815–5 (2005).

88. O. Haderka, J. Jan Peřina, and M. Hamar: "*Simple direct measurement of nonclassical joint signal-idler photon-number statistics and the correlation area of twin photon beams*". Journal of Optics B: Quantum and Semiclassical Optics **7,** 572–576 (2005).

89. C. K. Hong, Z. Y. Ou, and L. Mandel: "*Measurement of subpicosecond time intervals between two photons by interference*". Physical Review Letters **59,** 2044–2046 (1987).

90. G. Brassard, N. Lütkenhaus, T. Mor, and B. C. Sanders: "*Limitations on practical quantum cryptography*". Physical Review Letters **85,** 1330–1333 (2000).

91. A. A. Malygin, A. N. Penin, and A. V. Sergienko: "*Spatiotemporal grouping of photons in spontaneous parametric scattering of light*". Doklady Akademii Nauk SSSR **281,** 308–313 (1985).

92. G. Molina-Terriza, S. Minardi, Y. Deyanova, C. I. Osorio, M. Hendrych, and J. P. Torres: "*Control of the shape of the spatial mode function of photons generated in noncollinear spontaneous parametric down-conversion*". Physical Review A **72,** 065802–4 (2005).

93. B. Jost, A. Sergienko, A. Abouraddy, B. Saleh, and M. Teich: "*Spatial correlations of spontaneously down-converted photon pairs detected with a single-photon-sensitive CCD camera*". Optics Express **3,** 81–88 (1998).

94. O. Jedrkiewicz, Y. K. Jiang, E. Brambilla, A. Gatti, M. Bache, L. A. Lugiato, and P. D. Trapani: "*Detection of sub-shot-noise spatial correlation in high-gain parametric down conversion*". Physical Review Letters **93,** 243601–4 (2004).

95. M. Bondani, A. Allevi, and A. Andreoni: "*Ghost imaging by intense multimode twin beam*". The European Physical Journal **203.** *Special Topics,* 151–161 (2012).

96. E. Brambilla, A. Gatti, M. Bache, and L. A. Lugiato: "*Simultaneous near-field and far-field spatial quantum correlations in the high-gain regime of parametric down-conversion*". Physical Review A **69,** 023802–19 (2004).

97. A. Joobeur, B. E. A. Saleh, and M. C. Teich: "*Spatiotemporal coherence properties of entangled light beams generated by parametric down-conversion*". Physical Review A **50,** 3349–3361 (1994).

98. A. Joobeur, B. E. A. Saleh, T. S. Larchuk, and M. C. Teich: "*Coherence properties of entangled light beams generated by parametric down-conversion: Theory and experiment*". Physical Review A **53,** 4360–4371 (1996).

99. T. P. Grayson, and G. A. Barbosa: "*Spatial properties of spontaneous parametric down-conversion and their effect on induced coherence without induced emission*". Physical Review A **49,** 2948–2961 (1994).

100. O. Steuernagel, and H. Rabitz: "*Spontaneous parametric down-conversion for an arbitrary monochromatic pump beam*". Optics Communications **154,** 285–289 (1998).

101. G. Brida, A. Meda, M. Genovese, E. Predazzi, and I. Ruo-Berchera: "*Systematic study of the PDC speckle structure for quantum imaging applications*". Journal of Modern Optics **56,** 201–208 (2009).

102. A. Mosset, F. Devaux, G. Fanjoux, and E. Lantz: "*Direct experimental characterization of the Bose-Einstein distribution of spatial fluctuations of spontaneous parametric down-conversion*". The European Physical Journal D: Atomic, Molecular, Optical and Plasma Physics **28,** 447–451 (2004).

103. T. Wang, Y. Qiu, H. Cai, and J. Deng: "*A fast onboard star-extraction algorithm optimized for the SVOM visible telescope*". Science in China: Series G: Physics, Mechanics & Astronomy **53,** 51–55 (2009).

104. J. Jan Peřina, O. Haderka, V. Michálek, and M. Hamar: "*Absolute detector calibration using twin beams*". Optics Letters **37,** 2475–2477 (2012).

105. X. Y. Zou, L. J. Wang, and L. Mandel: "*Induced coherence and indistinguishability in optical interference*". Physical Review Letters **67,** 318–321 (1991).

106. R. Machulka, K. Lemr, O. Haderka, M. Lamperti, A. Allevi, and M. Bondani: "*Luminescence-induced noise in single photon sources based on BBO crystals*". Journal of Physics B: Atomic, Molecular and Optical Physics **47,** 215501–7 (2014).

107. F. Sciarrino, C. Vitelli, F. D. Martini, R. Glasser, H. Cable, and J. P. Dowling: "*Experimental sub-Rayleigh resolution by an unseeded high-gain optical parametric amplifier for quantum lithography*". Physical Review A **77,** 012324–5 (2008).

108. C. T. Chen, B. C. Wu, A. D. Jiang, and G. M. You: "*A new-type ultraviolet SHG crystal β-BaB_2O_4*". Scientia Sinica Series B: Chemical Biological Agricultutural Medical & Earth sciencies **28,** 235–243 (1985).

109. G. C. Bhar, S. Das, and U. Chatterjee: "*Evaluation of beta barium borate crystal for nonlinear devices*". Applied Optics **28,** 202–204 (1989).

110. M. D. Eisaman, J. Fan, A. Migdall, and S. V. Polyakov: "*Invited Review Article: Single-photon sources and detectors*". Review of Scientific Instruments **82** (2011).

111. A. Acín, N. Brunner, N. Gisin, S. Massar, S. Pironio, and V. Scarani: "*Device-independent security of quantum cryptography against collective attacks*". Physical Review Letters **98,** 230501–4 (2007).

112. C. Branciard, E. G. Cavalcanti, S. P. Walborn, V. Scarani, and H. M. Wiseman: "*One-sided device-independent quantum key distribution: Security,feasibility,and the connection with steering*". Physical Review A **85,** 010301–5 (2012).

113. Sangeeta, and S. C. Sabharwal: "*Thermally stimulated luminescence from alkaline earth borates*". Journal of Luminescence **104,** 267–271 (2003).

114. Sangeeta, and S. C. Sabharwal: "*Kinetics of thermally stimulated luminescence from alkaline earth borates*". Journal of Luminescence **109,** 69–74 (2004).

115. C. V. Reddy, C. R. Krishna, T. R. Rao, D. V. Sathish, P. Rao, and R. V. S. S. N. Ravikumar: "*Synthesis and optical properties of Co^{2+} and Ni^{2+} ions doped β-BaB_2O_4 nanopowders*". Journal of Luminescence **132,** 2325–2329 (2012).

116. P. Walther, M. Aspelmeyer, and A. Zeilinger: "*Heralded generation of multiphoton entanglement*". Physical Review A **75,** 012313–5 (2007).

117. M. Hunault, H. Takesue, O. Tadanaga, Y. Nishida, and M. Asobe: "*Generation of time-bin entangled photon pairs by cascaded second-order nonlinearity in a single periodically poled $LiNbO_3$ waveguide*". Optics Letters **35,** 1239–1241 (2010).